2013

Synthesis, Characterization, and Functionalization of Magnetic Iron Nanoparticles for Enhanced Biological Applications

Christopher Warren
Virginia Commonwealth University

Synthesis, Characterization, and Functionalization of Magnetic Iron Nanoparticles for Enhanced Biological Applications

A Dissertation submitted in partial fulfillment of the requirements for the degree of Doctor of Philosophy at Virginia Commonwealth University.

By

Christopher Ryan Warren
B.S., Virginia Commonwealth University, 1990

Director: Dr. Everett E. Carpenter
Assistant Professor of Chemistry

Virginia Commonwealth University
Richmond, Virginia
December 2013

Acknowledgments

In completion of this dissertation, there are many people to thank. First, I would like to thank for family for their support and patience throughout the years of study it took to finally complete this work. My wife Gail, daughters Abbey and Peyton, and sons Henry and Harrison spent too many weekends to mention without me as I worked on this dissertation in the lab, as well as the endless hours spent in my office writing. I would like to thank my committee for their input and for taking the time to challenge me and make me think about my work from their perspectives. I would like to thank my lab mates, especially Mike Shultz, who helped with the MRI data. I am also grateful for the Virginia Division of Consolidated Laboratory Services, especially Shane Wyatt and Dr. Tim Croley for helping me with the *E. coli* and MALDI analysis. Lastly, I would like to express gratitude to the Virginia Commonwealth University Department of Chemistry for giving me the opportunity to further my education.

Table of Contents

List of Figures

Chapter 1

Chapter 3

Chapter 4

Chapter 6

List of Tables

Chapter 2

Chapter 3

Chapter 4

Chapter 5

Abstract

SYNTHESIS, CHARACTERIZATION, AND FUNCTIONALIZATION OF MAGNETIC IRON NANOPARTICLES FOR ENHANCED BIOLOGICAL APPLICATIONS

By C. Ryan Warren Ph.D.

A Dissertation submitted in partial fulfillment of the requirements for the degree of Doctor of Philosophy at Virginia Commonwealth University.

Virginia Commonwealth University, 2013

Director: Dr. Everett E. Carpenter

Associate Professor of Chemistry

The transition metal ferrites of composition MFe_2O_4 where M is Fe, Co, or Ni are well established materials for various biological applications due to their interesting magnetic properties. Their elemental and stochiometric composition can be easily manipulated which allows further tuning of their ferrimagnetic properties. By changing the identity of M and by changing the crystallite size of the ferrites, nanocrystals with diverse magnetic properties can be systematically produced. Furthermore, ferrites are more stable in diverse chemical environments, as compared to metallic nanoparticles, which make ferrites particularly useful for a broad range

of biomedical applications, especially in the field of magnetic resonance imaging and cell labeling. In this work, spinel ferrites of composition $CoFe_2O_4$, $NiFe_2O_4$, and $Ni_{.5}Co_{.5}Fe_2O_4$ were synthesized by a polyol method utilizing ethylene glycol as the solvent, reducing agent, and surfactant. The nanoparticles produced were surface coated with 3-aminopropyltriethoxy silane to increase solubility as well as to serve as an anchor for further conjugation with targeting substrates such as peptides and antibodies.

The first part of this dissertation was focused on using the polyol method to produce nanoparticles of various metallic compositions. In each case, the polyol method provided an easy one-pot method to produce metallic as well as metal oxide nanocrystals. Utilizing the polyol method, ferrites of $CoFe_2O_4$, $NiFe_2O_4$, and $Ni_{.5}Co_{.5}Fe_2O_4$ were produced with size ranges between 20 nm and 50 nm depending on the reaction time in the polyol. The second part of this dissertation was concerned with the functionalization of the nanoparticles to serve as an anchor for further conjugation with targeting substrates in the immunoaffinity separation of food borne pathogens. These nanoparticles were functionalized using an anti-*E. coli* O157:H7 antibody, mixed with a food matrix, and then subsequently removed from the food matrix by an external magnet in order to be analyzed by Matrix Assisted Laser Desorption Ionization/Time of Flight (MALDI/TOF) Mass Spectrometry as a rapid identification method of bacterial pathogens. Furthermore, magnetic resonance imaging (MRI) was carried out on the polyol produced ferrites in order to measure the transverse relaxation time (T_2) of the nanoparticles in order to investigate

the size dependence and crystallite composition of the particles ability to affect the transverse relaxivity rarte (r_2). Further understanding of how ferrite composition and crystallite size affect their magnetic properties and resulting MRI contrast abilities will provide insight into the best materials for the next generation of contrast agents. Lastly, the ability of nanoparticles to serve as a stationary phase material for reversed phase ultrahigh pressure liquid chromatography will be discussed as a novel separation technique.

Chapter 1: Introduction

1.1 Introduction

Nanotechnology is the application of nanometer technologies in a wide range of areas. It is a very broad, interdisciplinary research field that involves various areas of science such as physics, engineering, biology and medicine. The necessity for synthesis of nanomaterials with well-controlled size and morphology has emerged in recent years as novel advanced applications have developed, especially in biological and biomedical fields. These applications require nanoparticles with more complex design, such as multifunctional nanoparticles that can attach to several components, each with its own functionality. In this chapter, a brief discussion of the unique properties of nanoparticles as well as an overview of the various synthesis and stabilization methods of nanoparticles will be discussed. Concluding the chapter will be an introduction to the biological applications of nanoparticles.

1.2 Overview

In the past 20 years, the synthesis of nanoparticles has been actively developed for fundamental scientific interest as well as for many technological applications. Some biomedical applications include magnetic separations, targeted drug delivery, contrast agents in magnetic resonance imaging, hyperthermia treatments, and biosensing applications. Industrial applications include magnetic seals in motors, magnetic inks, and catalysts.[1-4] These and many other

applications are the result of interesting physical properties that are affected by the size of particles at the nanoscale. A major characteristic of nanoscale material that is not present in the bulk material is the presence of unique or improved electronic, optical, and magnetic properties.[5-7] It is these unique magnetic properties at the nanoscale that is a focus of the work in this dissertation. An introduction into these unique properties as well as basic magnetic theory is given in the following sections.

1.3 Electronic Properties

The electronic properties of nanoparticles have been an actively researched topic in the past ten years. It has been predicted that metal semiconducting nanoparticles can display very different quantum effects from the bulk properties of the metal.[8-11] For example, if we take a cubic crystal of sodium metal that is 1.5 mm on an edge, it would contain approximately 10^{20} sodium atoms. The difference in energy between the bonding orbitals, also called the valence band, and the antibonding orbitals, also called the conduction band, decreases as the number of sodium atoms increases. The orbitals combine into an almost continuous band of energy levels. This is the basis for the molecular orbital band theory model for metals as shown in Figure 1.1.[12] As the number of atoms decreases as the crystal gets smaller, the energy difference between the conduction band and the valence band, or band gap, increases. When the size of the crystal is smaller than a critical length, called the exciton Bohr radius (a_b*), electron crowding leads to the

splitting of the original energy levels into smaller ones with smaller gaps between each successive level.[13-14] The band gap can be observed to shift through the entire visible region, from blue emission for the smaller particles to red emission for the larger particles as shown in Figure 1.2.[15-16]

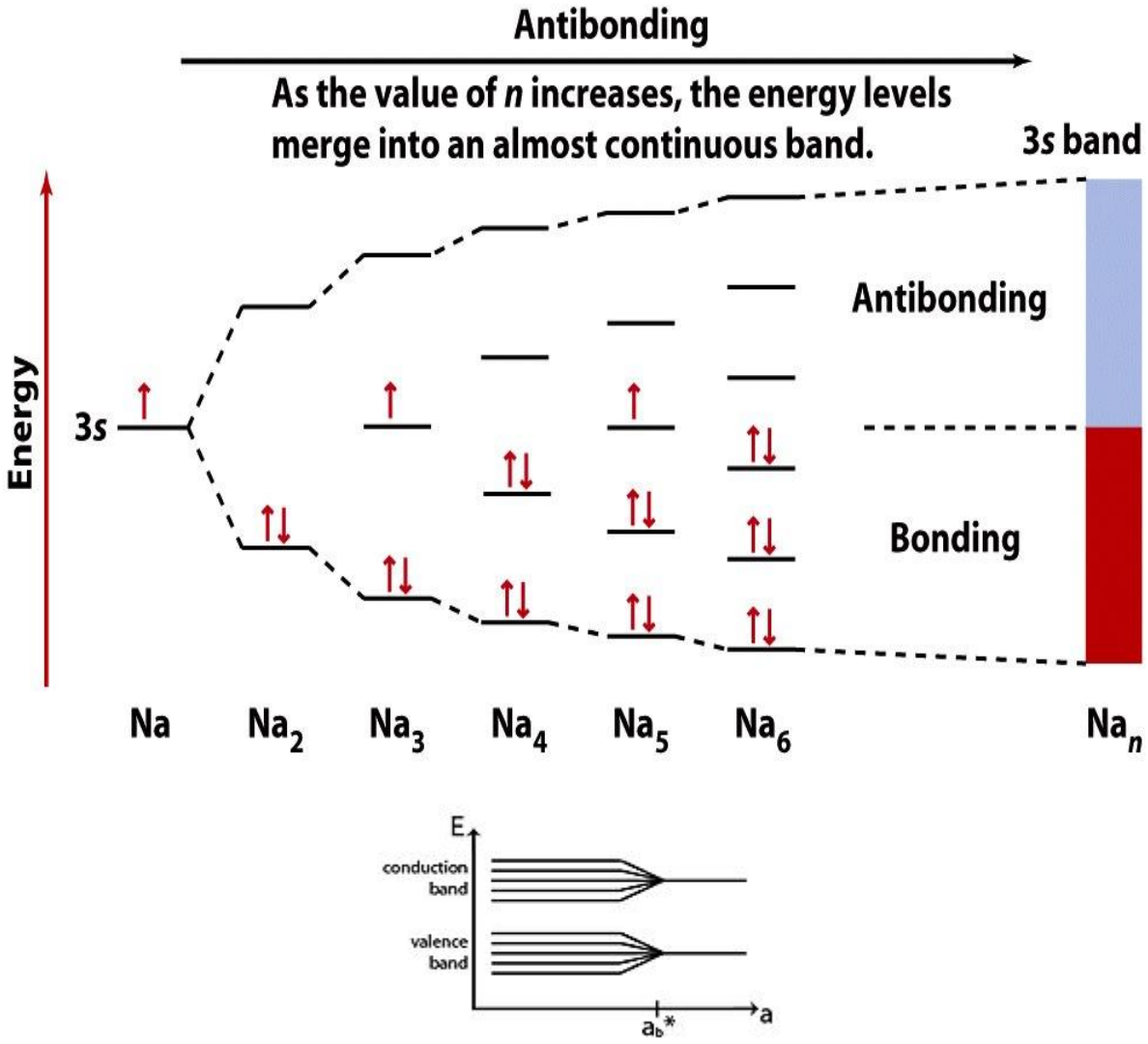

Figure 1.1. Molecular orbital energy levels for Na_n molecules showing the difference in energy between successive molecular orbitals decreases as the number of Na atoms increases (top).[12] The splitting of energy levels with smaller gaps at a crystal size smaller than the exciton Bohr radius (bottom).[13]

5

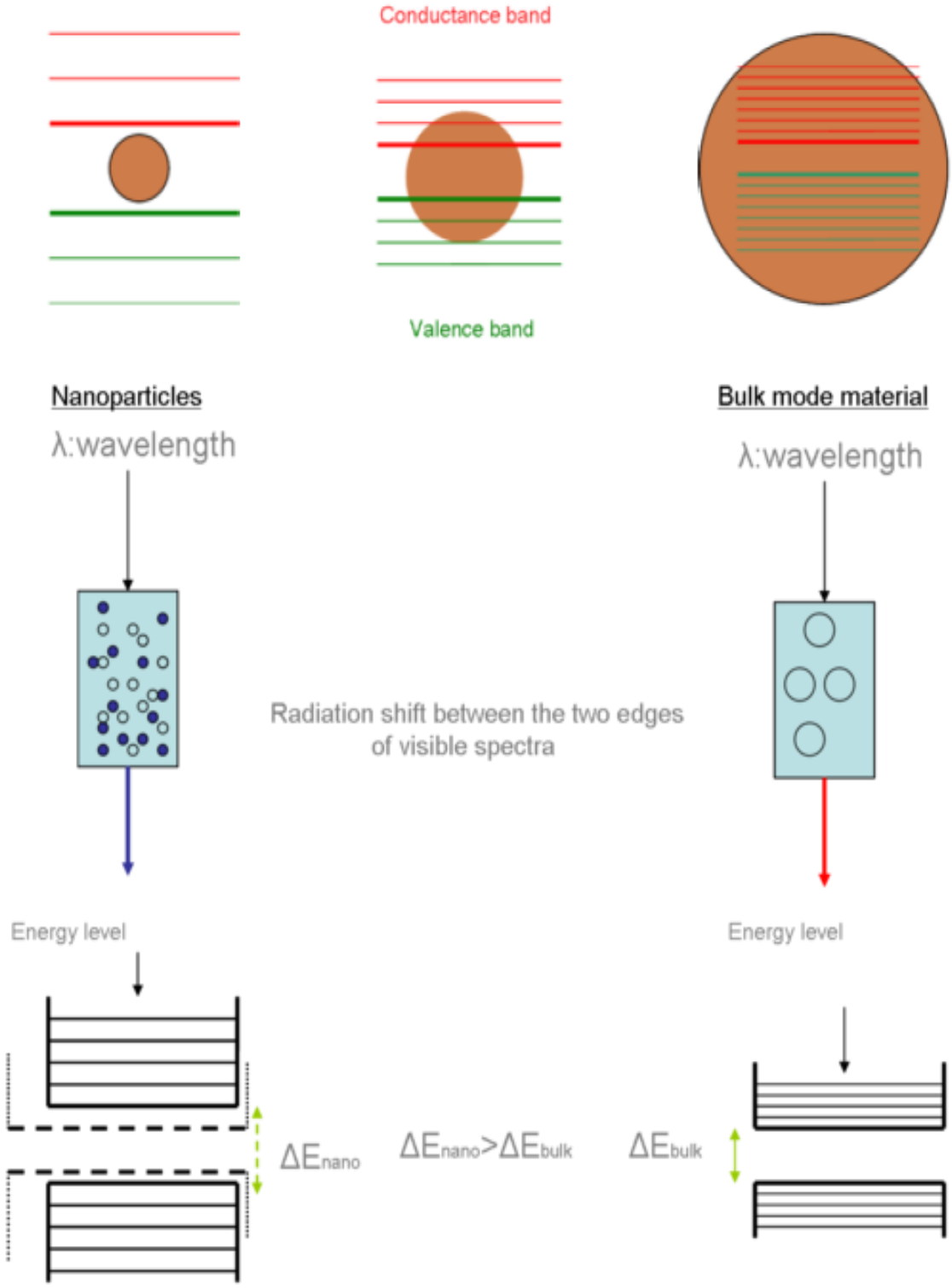

Figure 1.2. Illustation of the increase in band gap as the size of the particle decreases in diameter (top).[14] The radiation shift of particles relating particle size to band gap energies (bottom).[15-16]

1.4 Optical Properties

As described in the previous section, the optical properties of nanoparticles are different from their bulk counterparts. This difference is attributed to quantum effects, unique surface phenomena, and efficient charge transfer over nanoscale distances within nanomaterials. These phenomena result from localized surface plasmons.[17-23] Surface plasmon resonance can be described as the resonant, collective oscillation of valence electrons in a solid stimulated by incident light.[24] When conduction electrons oscillate coherently, they will distort an electron cloud from the nucleus producing a surface charge distribution as shown in Figure 1.3.[25] The

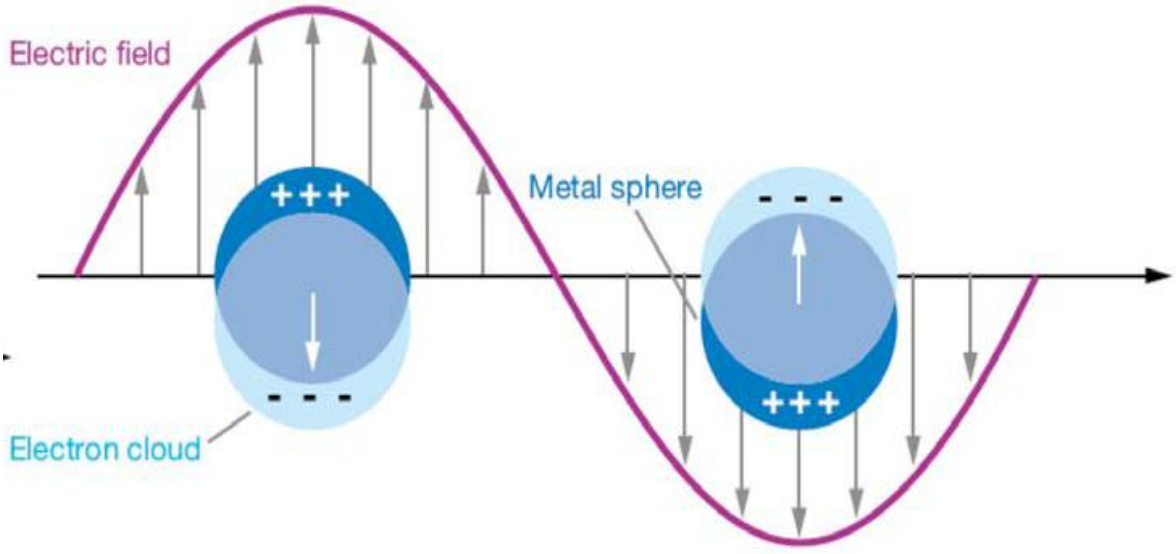

Figure 1.3. Surface plasmon resonance excitation of small particles by light irradiation.[25]

resonance condition is established when the frequency of light photons matches the natural frequency of surface electrons oscillating against the restoring force of positive nuclei. Surface plasmon excitation occurs when a photon is absorbed and transfers energy into the collective oscillations of conduction electrons that are coupled in phase with the incident light. Surface plasmon resonance in nanometer-sized structures is called localized surface plasmon resonance. In the case of nanoscale metal particles, the absorption wavelength associated with the s-p transitions depends on the shape and size of the particle. This is a unique property of nanoparticles that is due to the fact that the s-p (conduction) electrons are mostly free to move throughout the nanoparticle, and their energies are sensitive to their shape and size.[26-32] For gold and silver nanoparticles, these resonant frequencies occur within the visible spectrum, which is why you see the various colors of their colloidal solutions, as shown in Figure 1.4. The unique optical properties of nanoparticles have been known since the 4th century AD.[33] For example, silver nanoparticles were used to color glass in church windows yellow, while gold nanoparticles were used to make ruby-colored glass.

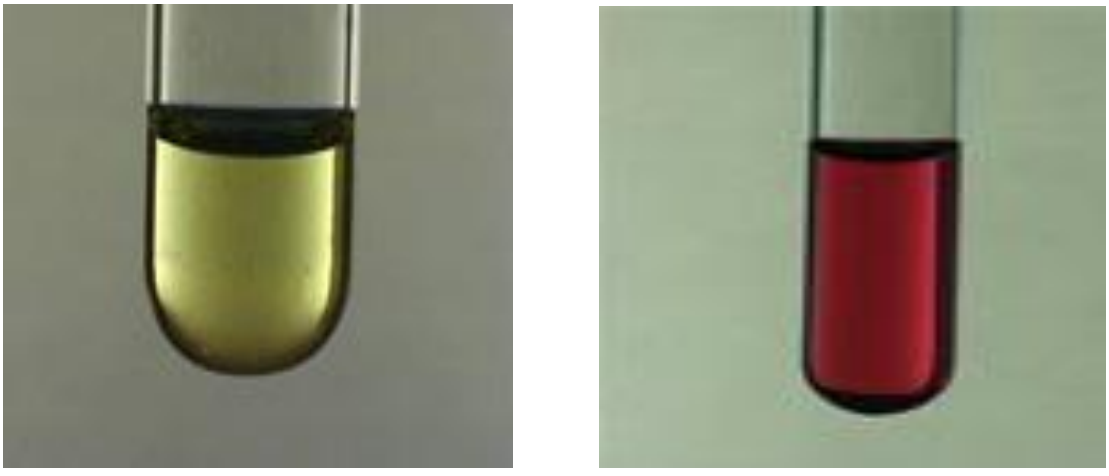

Figure 1.4 Colloidal silver nanoparticles (left) and gold nanoparticles (right).

When nanoparticles aggregate, the wavelengths of light absorbed changes as shown below in Figure 1.5.[33] Quantum confinement of the electrons provides a visualization of the electronic characteristics of materials depending on their size.

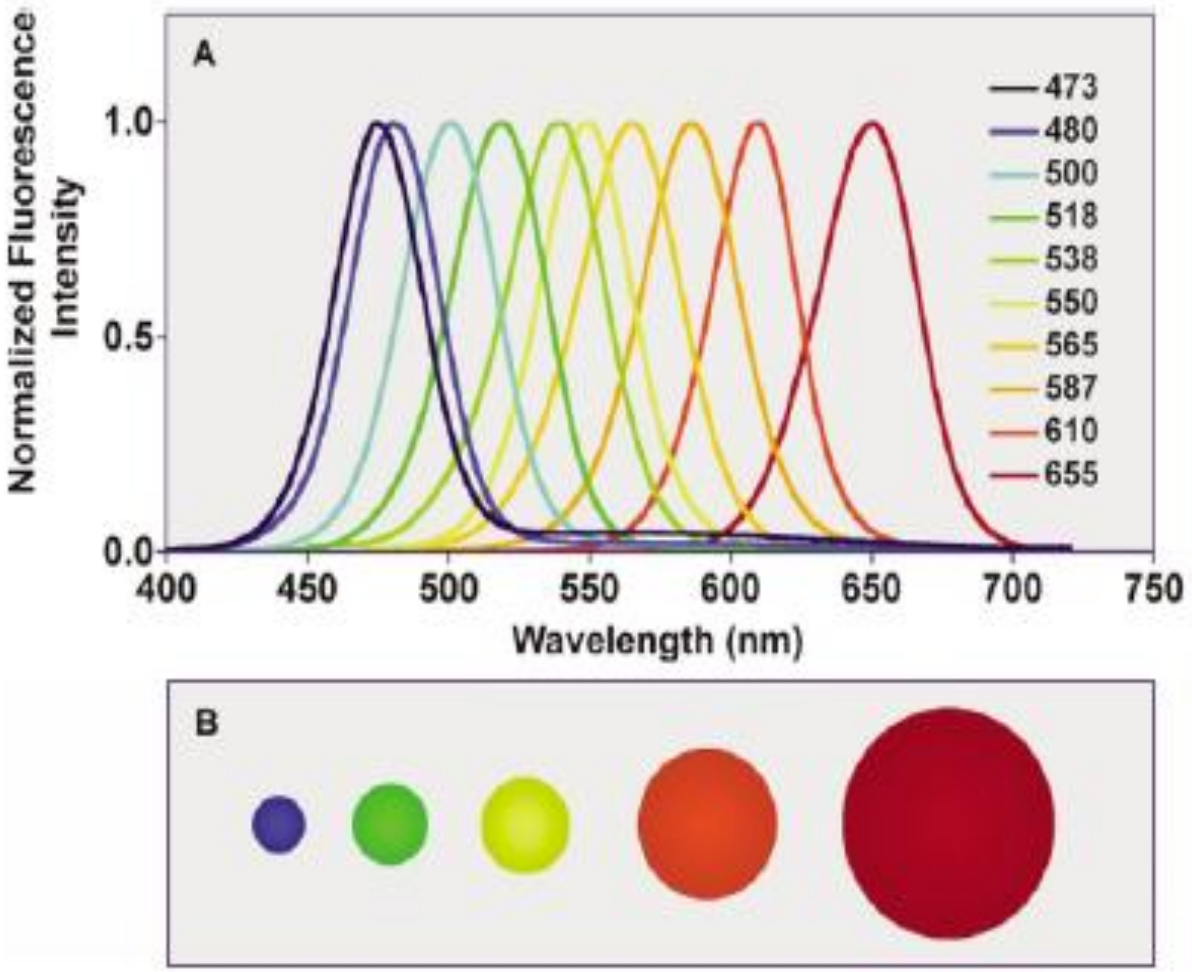

Figure 1.5. The change in fluorescence of nanoparticles as a function of particle diameter.[33]

When two particles stick together, the absorption produced is very similar to that of a single particle having a diameter equal to the sum of the diameters of the two particles. The ability to take advantage of this property of nanomaterials has brought about a lot of interest in the area of biomedical imaging and sensing. The optical properties can be selectively tailored by controlling the dimensions of the nanomaterials in terms of shape, size, and surface properties. For example, the various colors associated with colloidal silver nanoparticles at different stages of particle aggregation are shown in Figure 1.6. On the far left of Figure 1.6, the silver particles have an average diameter of 10 – 14 nm. As the particles begin to aggregate, their average size begins to increase. The orange solution contains particles in the 35 – 50 nm range. The violet solution contains particles in the 60 – 80 nm range, and the silver colored solution on the far right has particles in the 100 nm range. These distinctive colors are a result of the resonance of localized surface plasmons brought about by visible light.

Figure 1.6. Colloidal silver nanoparticles in various stages of aggregation.

1.5 Magnetic Properties

Magnetism results from the spin of unpaired electrons in an atom. In an atom, the electron possesses spin that is equivalent to the strength of the magnetic moment of the electron. These electrons are arranged into orbitals of increasing energy, with each orbital containing a maximum of 2 electrons with opposing spins. Therefore, when an orbital is full there is no net magnetic moment. Diamagnetism is the result, which refers to a substance that contains all paired electron spins, and therefore has no net magnetic moment. The most common diamagnetic substances are water and wood. In other materials, the electron orbitals are not completely full, and there is a resultant magnetic moment due to the unpaired electrons. This type of magnetism is called paramagnetism.

Due to the magnetic field generated by unpaired electrons, paramagnetic atoms may act like miniature magnets in the presence of an external magnetic field. However, when the external magnetic field is removed, thermal fluctuations make the magnetic moment of the material move about randomly. If there is coupling between the neighboring magnetic moments of a paramagnetic material, spontaneous ordering of the moments will occur below a critical temperature. There are three types of coupling in which atomic spins in a material can interact. They are direct, indirect, and superexchange coupling. The basis of this coupling is the quantum mechanical coupling between electrons of adjacent atoms. In direct coupling, the distance

between electrons in the two atoms is relatively small, and as a result of the Pauli exclusion principle, the electrons will align themselves in an antiparallel arrangement. This type of spin arrangement produces the antiferromagnetism. Indirect coupling is an interaction that occurs at greater distances than direct coupling. This interaction is very common in metals and occurs when a magnetic atom induces a spin polarization in the conduction band electrons. Different metals will have different distances to which indirect coupling can act due to conductivity and spatial arrangement. In superexchange coupling, there is a coupling of spins of two next to nearest neighbor cations through a non-magnetic anion, usually oxygen, as shown in Figure 1.7. The distance, orientation and bond angles of the superexchange will determine whether the coupled electrons align themselves in a parallel or anti-parallel arrangement. For example, superexchange interactions are strongest when the Fe-O-Fe bond angles are 120°-180° resulting in a strong antiferromagnetic arrangement and they are weakest when the Fe-O-Fe angle is 90° resulting in weak antiferromagnetic interactions. This coupling mechanism is the primary method in which magnetization is produced in ferrites.

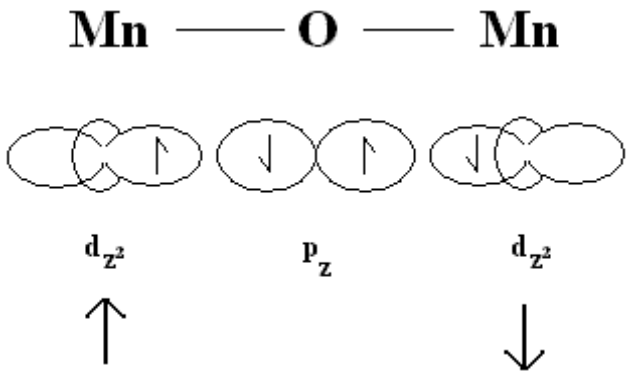

Figure 1.7. Superexchange coupling between two Mn atoms through an oxygen atom.

The ordered arrangements of magnetic moments tend to decrease with an increase in temperature. If the ordering involves alignment of all of the moments in the same direction, the substance is referred to as being ferromagnetic, and the critical temperature is called the Curie temperature T_C. This is the temperature transition point at which a substance will spontaneously change from ferromagnetic to paramagnetic. The driving force that causes this transition is thermal energy. When the thermal energy of the system becomes too great, the spins will break alignment from each other, and they will become more random relative to each other. Spontaneous magnetization will be lost, and paramagnetic behavior will result. If some of the moments are aligned opposite to the others, but the relative numbers or magnitudes of the moments give a resultant magnetic moment, the substance is referred to as being ferrimagnetic. Ferrimagnetism and ferromagnetism share essentially the same properties. If half of the moments are aligned opposed to the other half resulting in no net moment, the substance is antiferromagnetic and the critical temperature is called the N´eel temperature, T_N. Similar to the Curie temperature for ferromagnetic materials, the N´eel temperature is the temperature at which an antiferromagnetic material will display paramagnetic behavior. The Curie temperature and N´eel temperature are phenomenon of secondary transitions when the thermal energy of the system is equal to the exchange coupling energy. Another temperature that is measured in the study of magnetic nanoparticles is the blocking temperature $T_{B.}$ This is the temperature at which thermal energy is sufficient to break some magnetic alignment between spins. The blocking

temperature is at a lower temperature than the Curie and N´eel temperatures. Typical blocking temperatures are between 5 K and 300 K. The blocking temperature is the point at which spins that were aligned by an external magnetic field at room temperature and then frozen in place gain enough thermal energy to become more unaligned. The result is not a total loss of magnetization and coupling, but rather a loss of interaction between domains formed in nanomaterials. Figure 1.8 diagrams the various arrangements of magnetic moments in materials along with their corresponding critical temperature.

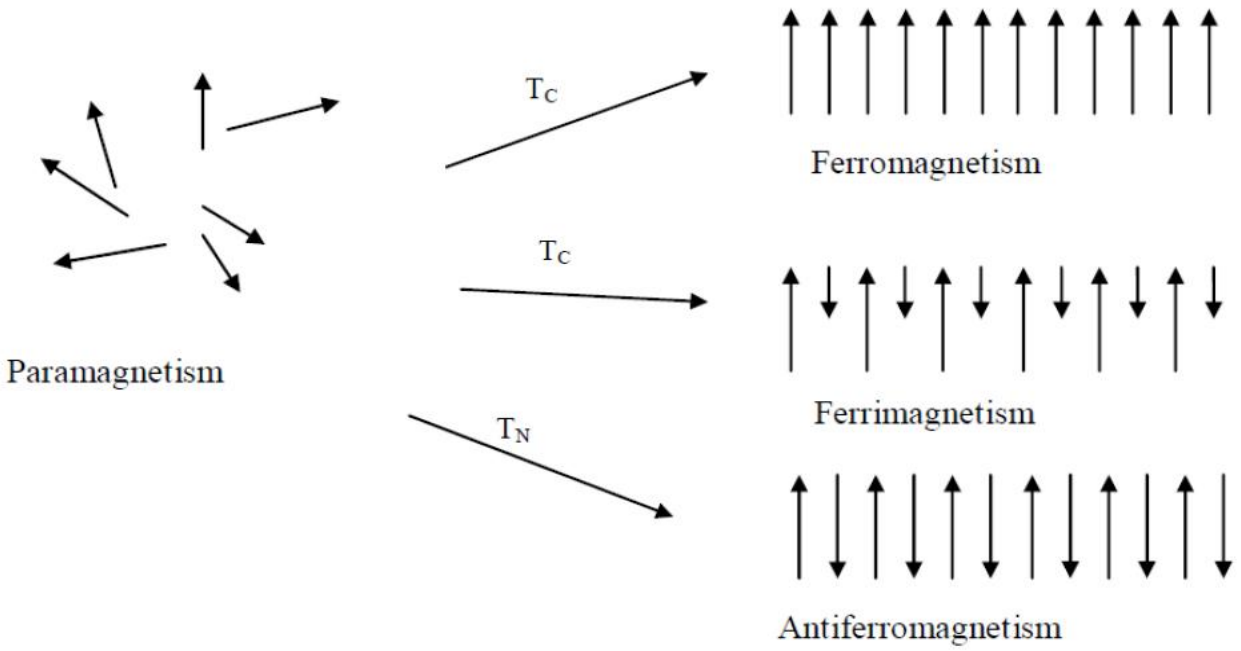

Figure 1.8. Alignment of atomic magnetic moments in various materials.

When a ferromagnetic material with magnetization M is put into a magnetic field H, a hysteresis curve is obtained as shown in Figure 1.9. This curve shows that the magnetization increases under an increasing magnetic field until it reaches a maximum value called saturation magnetization M_S. When the field decreases back to zero, there is a tendency for a material to maintain some alignment gained from being put in the saturating magnetic field. This is referred to as remnant magnetization M_R. The magnetic field strength required to obtain a zero moment is termed coercivity H_C. The presence of remnant magnetization and coercivity in a hysteresis curve is typical of a ferromagnetic material. Superparamagnetic materials that are smaller than 50 nm in diameter usually do not exhibit remnant magnetization, and therefore revert back to zero magnetic moment in the absence of an external magnetic field. Superparamagnetic materials return to paramagnetic behavior without remnant magnetization at temperatures below the Curie

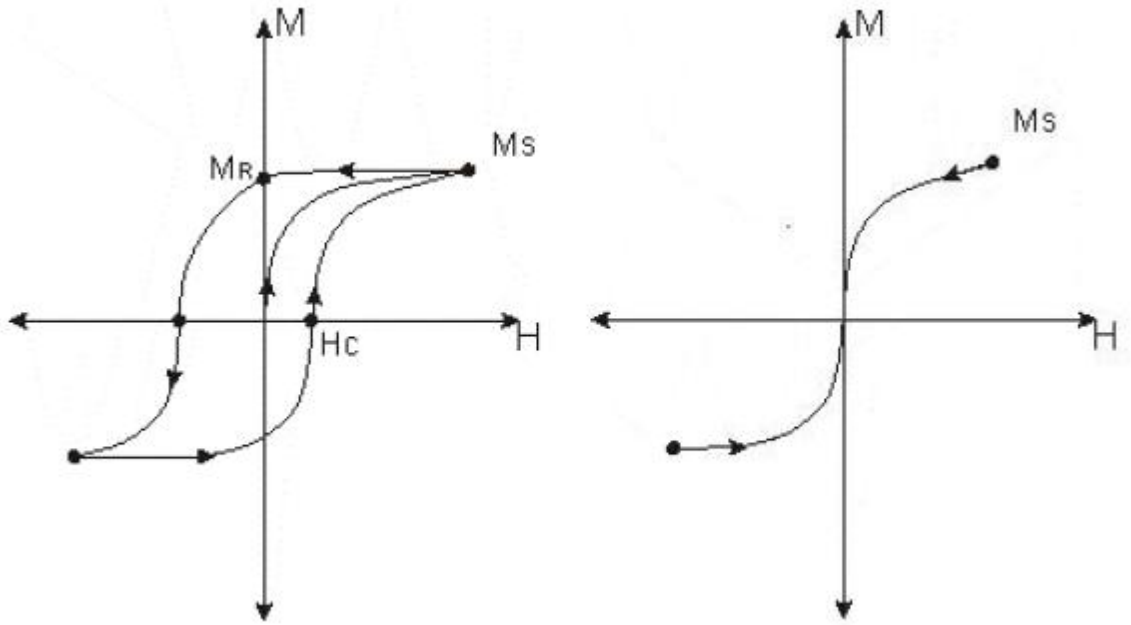

Figure 1.9. Hysteresis curve of ferromagnetic (left) and superparamagnetic (right) materials.

temperature as there is enough thermal energy in the surroundings to bring about paramagnetic behavior. This phenomenon occurs with particles that are less than 10 nm, and these particles are referred to as having a single domain.

In large crystals, not all of the crystals magnet moments will be preferentially aligned. Large particles, which have diameters greater than 50 nm, have a multi-domain structure with regions of net magnetization that are separated by domain walls as shown in Figure 1.10.[34] Coercivity levels off as the particles size reaches some bulk value (green region). As the particles decrease in size, but stay multidomain, the coercivity increases. This can be the result of shape anisotropy in the crystal structure. The critical diameter D_C is the point at which the indirect exchange coupling reaches throughout the entire particle, forming a single domain. A single domain particle that is uniformly magnetized will have all of its spins aligned in the same direction and will have a high coercivity and the highest remnant magnetization (blue region). As particle size decreases below the critical diameter, the size of the domain will not have enough spins to couple together and overcome the thermal energy in the surroundings, which will decrease the coercivity to zero (red region). The red region represents particles that are in the superparamagnetic range.

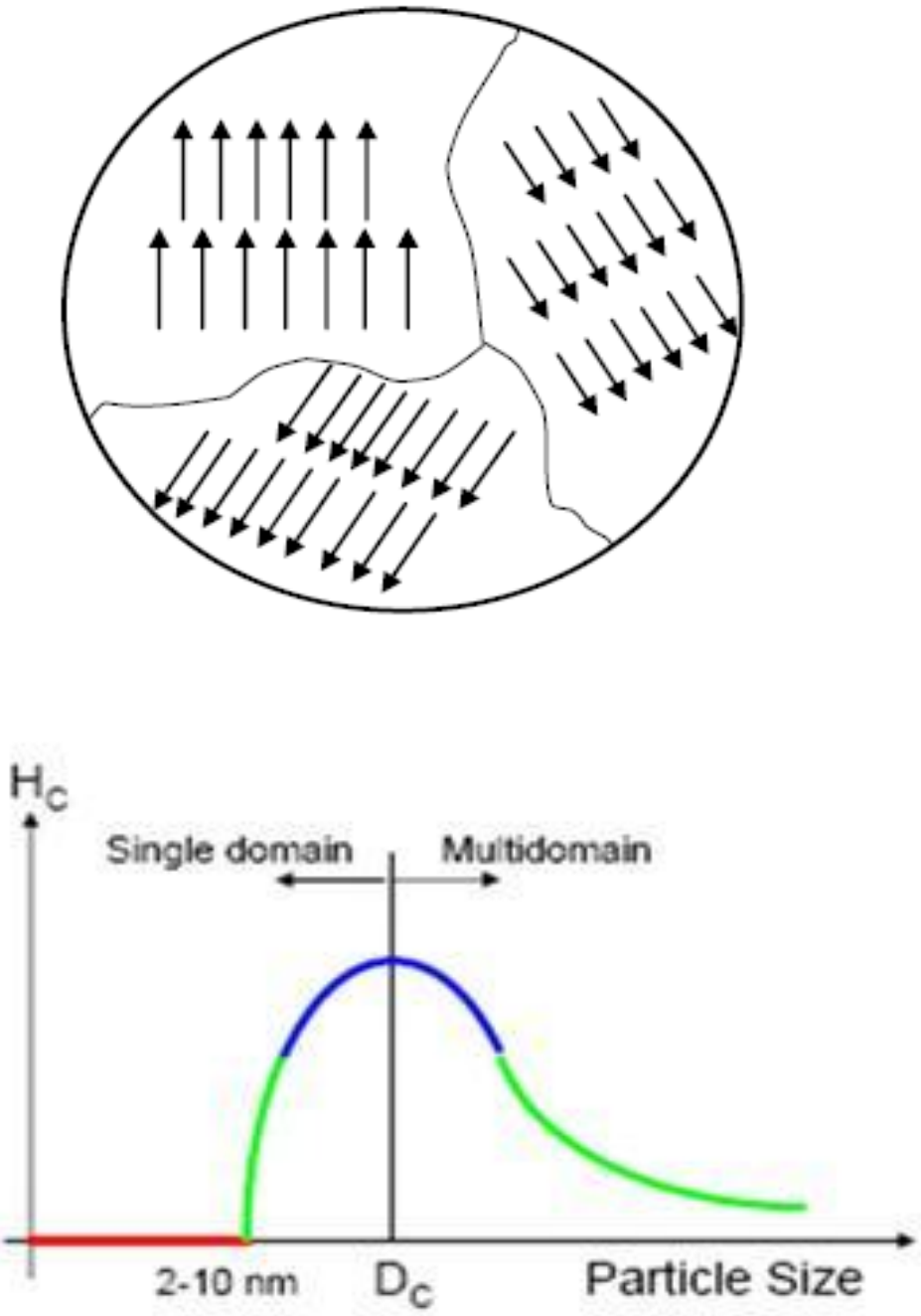

Figure1.10. Multi-domain structure of bulk material (top) and coercivity vs. particle diameter (bottom).[34]

1.6 Crystal Structures of Iron and Iron Oxide Compounds

Metallic iron crystallizes in either a body centered cubic structure or a face centered cubic crystal structure. The body centered cubic (bcc) structure of iron is the thermodynamically stable form of iron and is called α-iron. The body centered cubic structure is shown below in Figure 1.11. The unit cell is formed by placing one iron in each of the eight corners of the cube and one atom in the center. The corner atoms each count 1/8 and the center atom counts as one for a total of two iron atoms per unit cell.

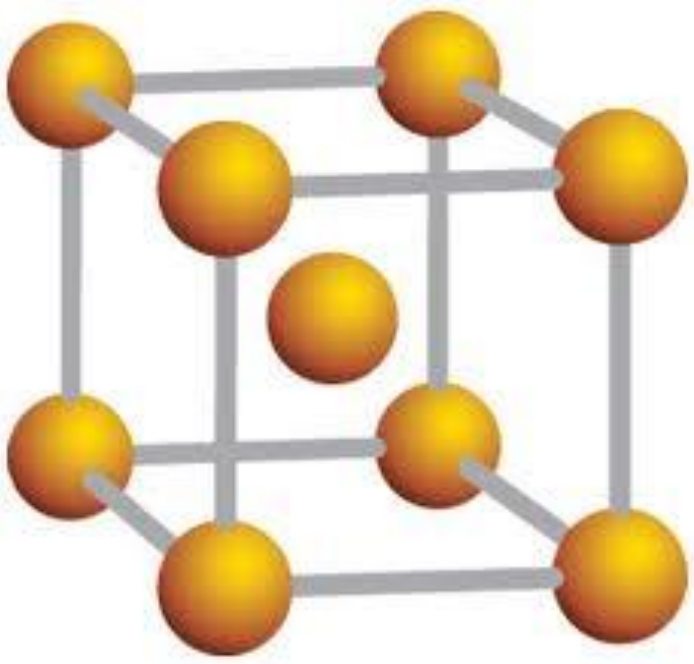

Figure 1.11 Body centered cubic structure.

The face centered cubic structure (fcc) is formed in a similar fashion as the body centered cubic structure. Instead of having an atom occupy the center of the unit cell, atoms are placed on the six faces of the cube. The corner atoms each count 1/8, as in the body centered cubic structure, with atoms on the faces counting for 1/2 for a total of four atoms per unit cell. The face centered cubic structure of iron is only stable at high temperatures and is called γ iron. The face centered cubic structure is shown below in Figure 1.12.

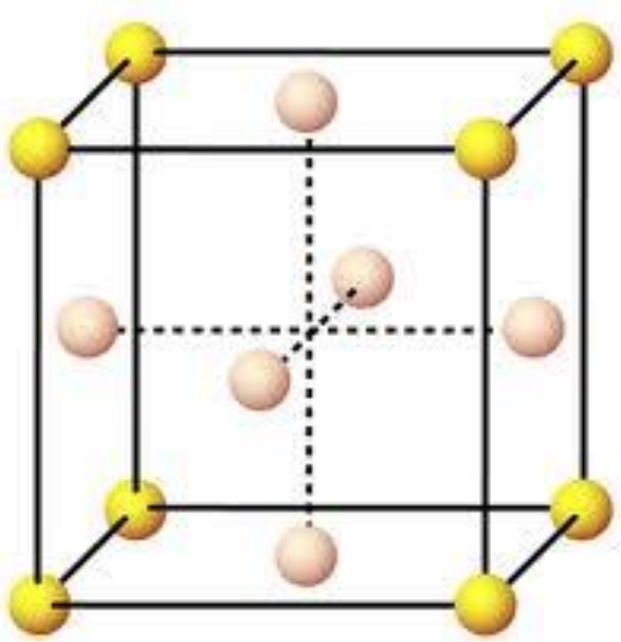

Figure 1.12. Face centered cubic structure.

The body centered cubic structure of iron is the more desired form due to its strong magnetic properties. Unfortunately, it is very difficult to obtain due to the ease by which iron is oxidized. After oxidation occurs, the magnetic properties are greatly diminished, and it is for this reason that a large amount of research is focused on surrounding the surface of the iron with a material to prevent its oxidation and subsequent loss of magnetic properties.

Magnetite, which is a focus of the work in this dissertation, has the peculiarity of containing both Fe^{2+} and Fe^{3+} ions, within a spinel crystal structure. The spinels are any of a class of minerals of general formulation $A^{2+}B_2^{3+}O_4^{2-}$ with the oxide anions arranged in a face center cubic (FCC) crystal structure and the metal cations occupying interstitial sites. These interstitial sites are of two types; metal cations coordinated with four oxygen atoms, and metal cations coordinated to six oxygen atoms. These sites are known as tetrahedral and octahedral, respectively, as shown in Figure 1.13. The spinel structure was named for the mineral $MgAl_2O_4$, in which the trivalent aluminum cations occupy the 16 octahedral sites and the 8 tetrahedral sites are occupied by the divalent magnesium cations. This arrangement of atoms where the octahedral sites are solely occupied by trivalent atoms and the tetrahedral sites are occupied by the divalent atoms is known as the normal spinel structure. An inverse spinel structure has all of the divalent cations occupying the octahedral sites. Ferrites are referred to as having the spinel structure since the actual distributions of cations is somewhere between the normal and inverse spinel structure.

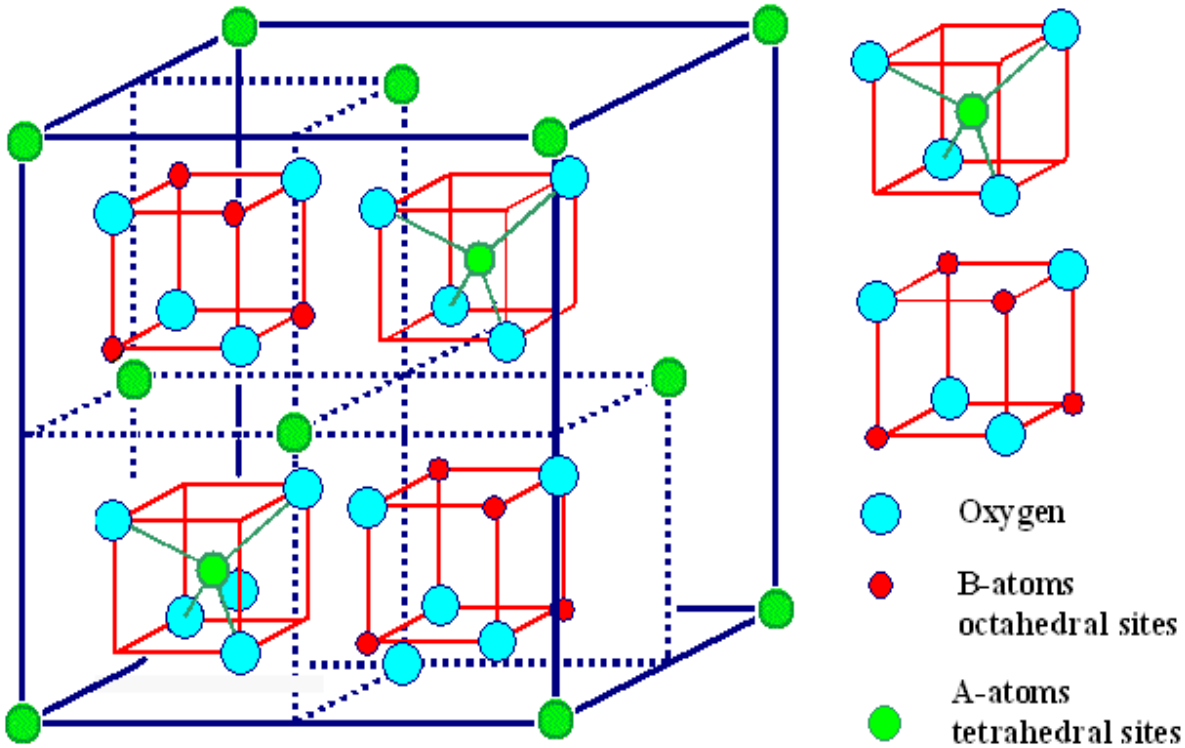

AB_2O_4 spinel The red cubes are also contained in the back half of the unit cell

Figure 1.13. Basic spinel structure illustrating the octahedral and tetrahedral sites relative to the position of oxygen.[35-36]

In the case of magnetite, the divalent Fe^{2+} occupies half of the octahedral sites, with the remaining octahedral and all of the tetrahedral sites being occupied with the trivalent Fe^{3+} cations as shown in Figure 1.14. Since there are the same numbers of octahedral and tetrahedral Fe^{3+} ions, they cancel each other out magnetically, and the resulting magnetic moment of magnetite arises only from the uncompensated octahedral occupied Fe^{2+} ions. This organization is sometimes represented as Fe^{3+} [Fe^{2+} Fe^{3+}] O_4.

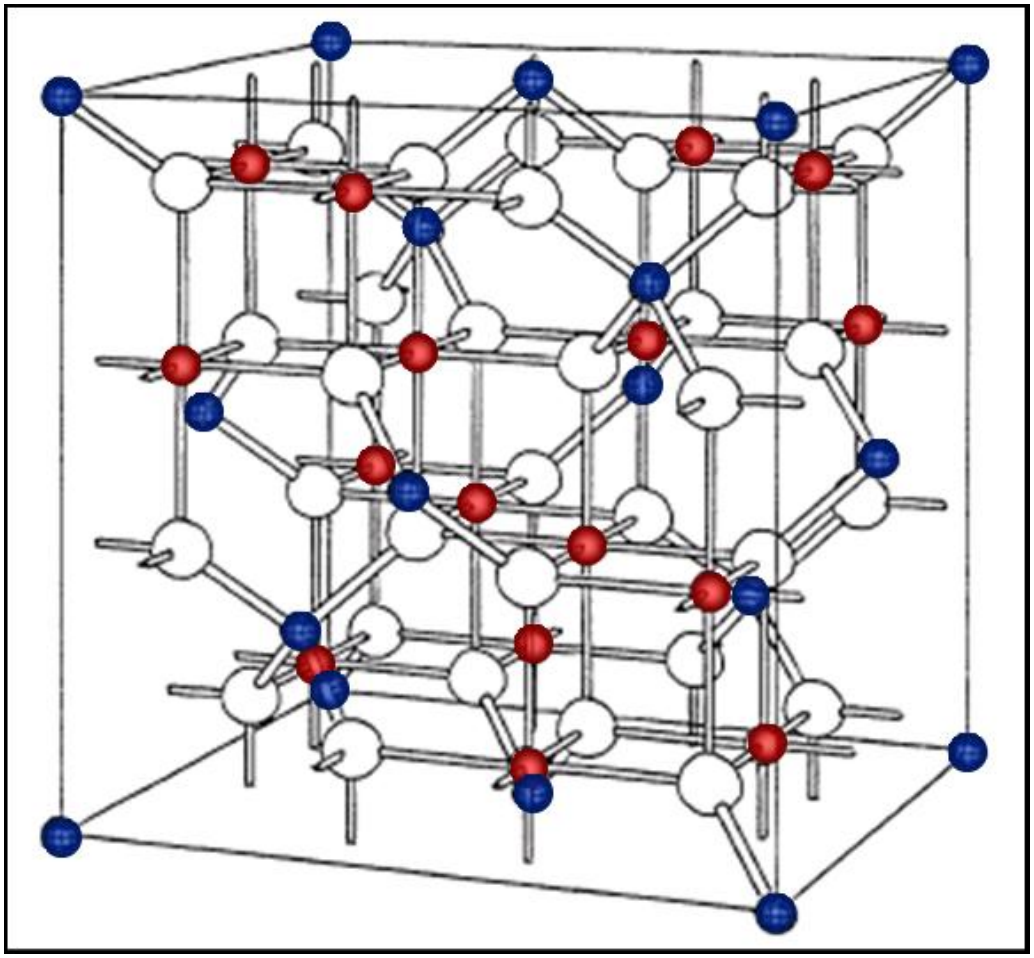

Figure1.14.Crystal structure of magnetite. Blue atoms are tetrahedrally coordinated Fe^{3+}; red atoms are octahedrally coordinated, 50/50 Fe^{2+}/Fe^{3+}; white atoms are oxygen.[35-36]

Magnetite is ferrimagnetic due to superexchange oxygen mediated coupling. In spinel oxides, the metal cations are separated by an oxide O^{2-} ion. The separation between the two metals is too large to involve direct coupling, therefore, it has been proposed that the spin configurations of the metal and the oxide ion become intermingled causing and extra reduction of ground state energy.[37] This lowering of the ground state energy does not occur if the metals have parallel spins. The main type of interaction is antiferromagnetic coupling and is greatest between the octahedral and tetrahedral sites when the Fe-O-Fe bond angle is 127°. Between these sites, there is a J_{eff} of -28 Hz. The lowering of the ground state energy between two tetrahedral sites results in a J_{eff} of -18 Hz and there is an increase in the energy between two octahedral sites with a J_{eff} of 3 Hz. Figure 1.15 shows a representation of the superexchange interactions between two metals through oxygen.[35-37] Therefore, as mentioned previously, all of the magnetic moments of the Fe^{3+} tetrahedral occupied ions are aligned in one direction, while all of the Fe^{3+} octahedral occupied ions are aligned in the opposite direction as a result of superexchange oxygen mediated coupling as shown in Figure 1.16. Thus the higher the magnetic moment of the divalent cation, the greater will be the overall magnetization that results. For example, a manganese ferrite containing Mn^{2+} with five unpaired electrons should have a larger magnetization than magnetite with four unpaired electrons. Likewise, magnetite should be more magnetic than a Co^{2+} ferrite with three unpaired electrons, and a Co^{2+} ferrite should be more magnetic than a Ni^{2+} ferrite with two unpaired electrons. Figure 1.17 shows the orbital diagrams and a schematic representation of these mixed metal ferrites.

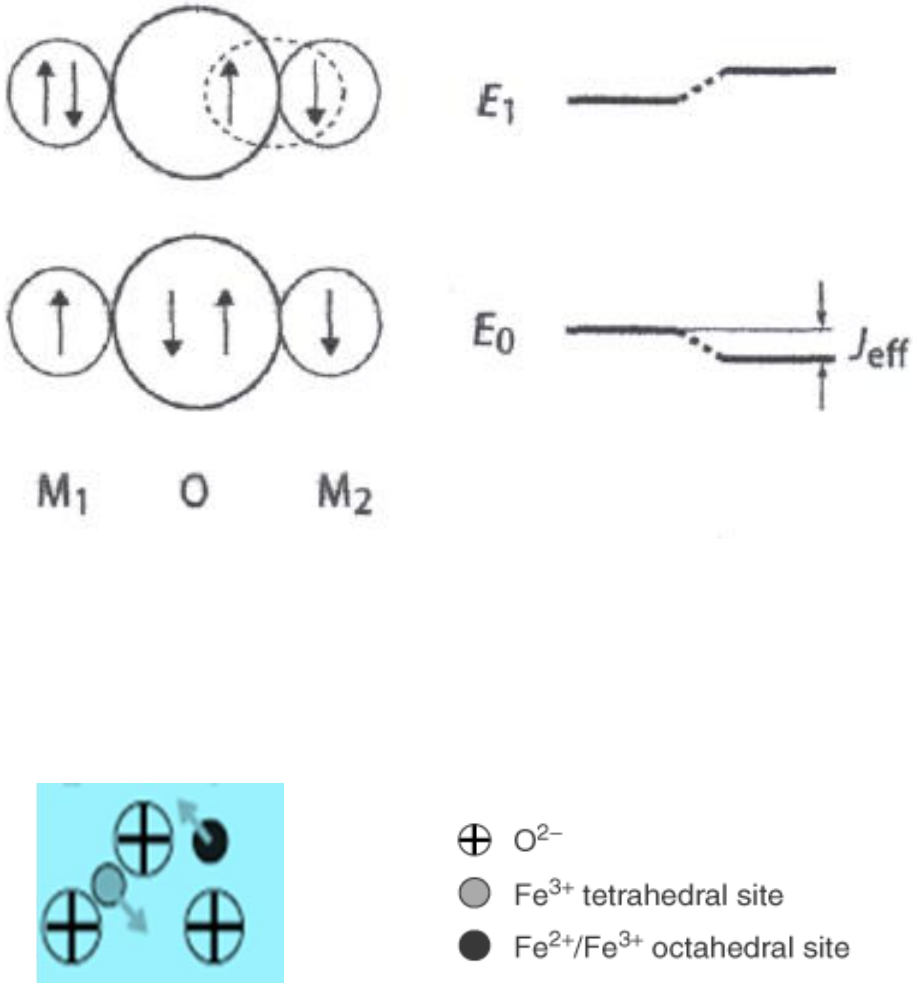

Figure 1.15. Ground state and excited state of two metal ions M_1 and M_2 showing the spin configuration interactions between an oxygen atom (top), and diagram of spin interactions in magnetite (bottom).[35-36]

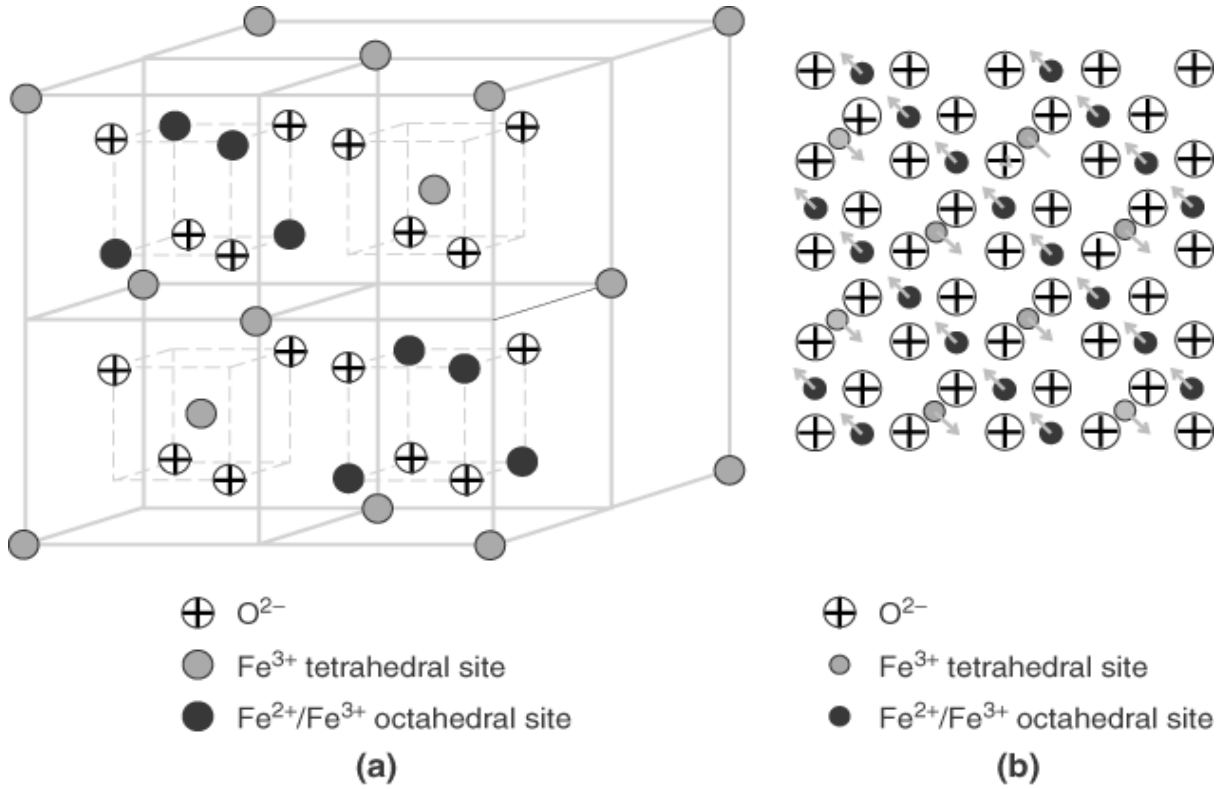

Figure 1.16. Inverse spinel structure of magnetite showing the magnetic spin interactions between the octahedral and tetrahedral sites within the lattice.[36]

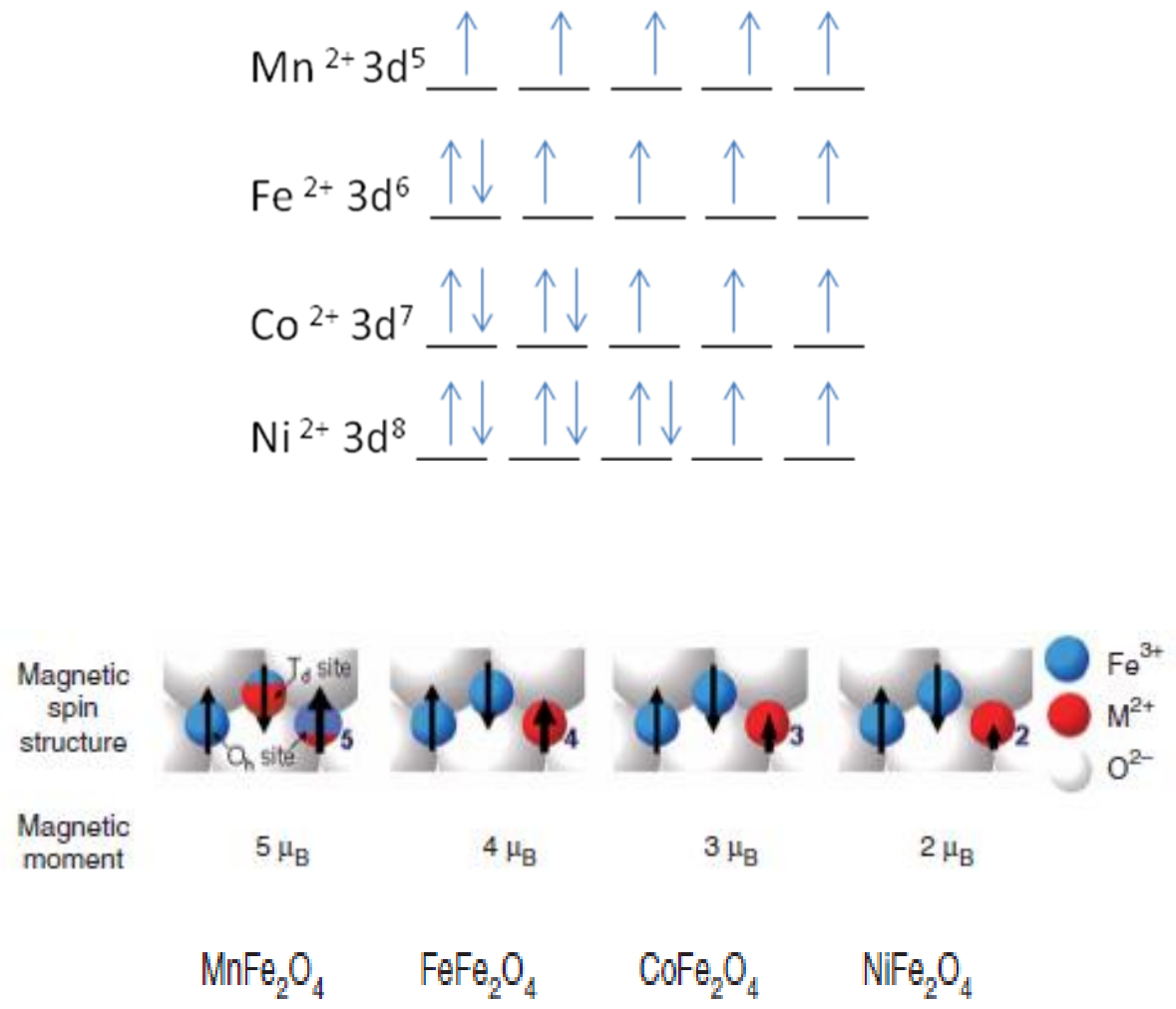

Figure 1.17. Orbital diagram of Mn^{2+}, Fe^{2+}, Co^{2+}, and Ni^{2+} showing the numbers of unpaired electrons (top), and their effect on the magnetic properties of mixed metal ferrites (bottom).

The resulting magnetic moment of magnetite is not directed randomly; it is aligned along a preferred direction called the anisotropy axes, or easy axes. The anisotropy axes are determined by the composition and crystallographic structure. The coupling energy between the field and the crystal magnetic moment is at a minimum when the magnetic moment is directed along this preferred direction. In the case of uniaxial anisotropy, there are only two anisotropy directions. The coupling energy therefore depends on the angle between the magnetic moment and the anisotropy axes. When the angle is 0° or 180°, the energy is at a minimum, and the alignment of the magnetic moments along these two directions is at a maximum as shown in Figure 1.18

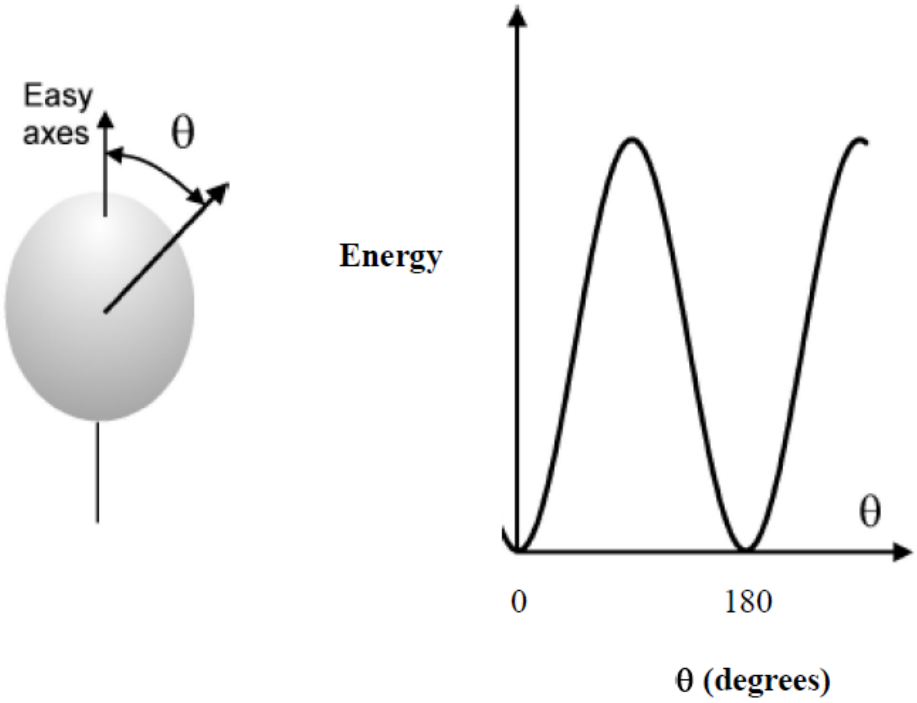

Figure 1.18 The change associated with the magnetic energy and the tilt angle between the anisotropy axes.[36]

In magnetite, there are eight anisotropy axes directed along the [111] cube diagonals. These are referred to as the easy directions. The axes directed along the [110] are the called the medium axes, while the axes along the [100] are referred to as the hard axes as shown in Figure 1.19.[36]

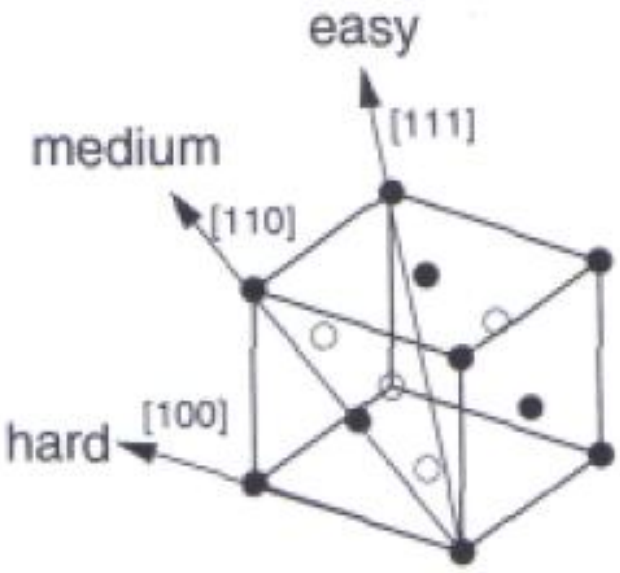

Figure 1.19 Illustration of the easy, medium, and hard anisotropy axes of magnetite.[36]

In small single domain crystals, a flip of the magnetic moment from one anisotropic direction to another anisotropic direction can be observed. If the thermal energy of the system is enough to overcome the anisotropy energy, the magnetization will change between the two different anisotropy directions within a specific time interval called the N´eel relaxation time.[35-36]

The N´eel relaxation is another important parameter of the magnetic behavior of magnetic particles. It is characterized by the time constant of the return to equilibrium of the crystals magnetization after an external magnetic force has been applied to the crystal as shown in Figure 1.20. In a very high anisotropy condition, the crystals magnetization will be locked into alignment with the easy axes, which favors the direction with the lower magnetic energy. The N´eel relaxation therefore describes the changes that come about from the change of the magnetic moments between the two different easy axes directions. The N´eel relaxation time increases exponentially as a function of the volume of the particle. In magnetite, the N´eel relaxation time is on the order of 10^{-9} seconds for a particle diameter of 20 nm. When the particle diameter increases to 30 nm, the N´eel relaxation time is on the order of 700 years.[36] This extreme relaxation time certainly explains magnetite's role in magnetic data recording.

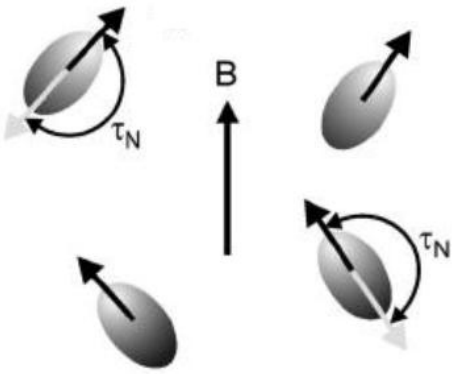

Figure 1.20 Illustration of N´eel relaxation after the application of a magnetic field B.[157]

In the case of magnetic crystals dispersed in aqueous fluids, the return of the magnetization to equilibrium is determined by two processes. The first one is N´eel relaxation, as described above, and the second one is the Brownian relaxation. The Brownian relaxation describes the rotation of the entire particle in the solvent as shown in Figure 1.21. The total relaxation rate (τ) of the magnetic fluid therefore has contributions from both the N´eel relaxation time ($\tau_{N)}$ and the Brownian relaxation rate (τ_B) shown in equation (1).

$$\frac{1}{\tau} = \frac{1}{\tau_N} + \frac{1}{\tau_B} \qquad (1)$$

For large particles, τ_B is shorter than τ_N. This is because the Brownian component of the magnetic relaxation is proportional to the particle volume whereas the N´eel relaxation time is an exponential function of the volume. Therefore, the Brownian relaxation rate is the main process that brings about equilibrium in large particles as illustrated in Figure 1.22.

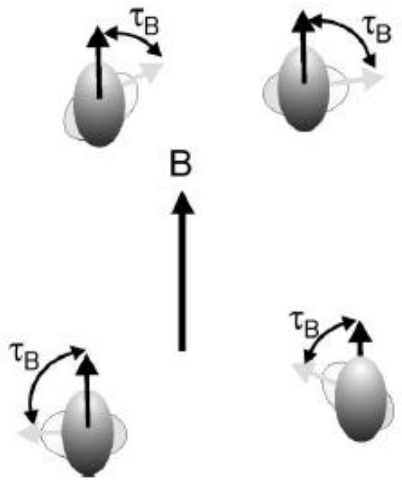

Figure 1.21 Illustration of Brownian relaxation after the application of a magnetic field B.[157]

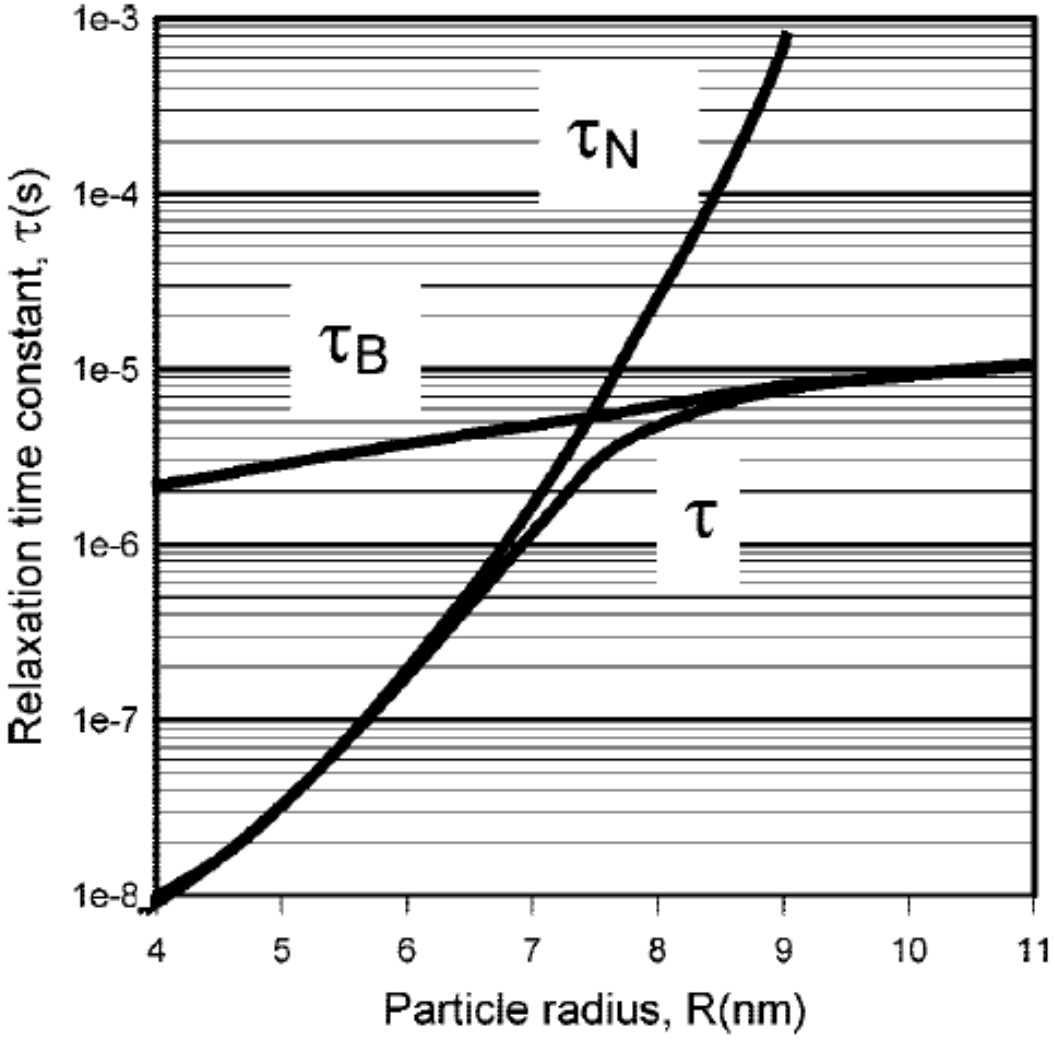

Figure 1.22 Graphical representation of the change of the N´eel and Brownian relaxation times as a function of particle radius.[157]

1.7 Synthesis Strategies:

There are a multitude of synthetic routes for the production of magnetic nanoparticles for biochemical applications.[38-48] The synthesis techniques can be divided into procedures that produce particles from solutions (precipitations, coprecipitations, microemulsions, and polyol), from aerosol/vapor phases (spray pyrolysis and laser pyrolysis), and those that produce nanoparticle composites consisting of magnetic particles surrounded by organic and inorganic matrixes. Magnetic nanoparticle syntheses, like most other synthetic processes, are developed with the goal of product uniformity, predictable reproducibility, and property control based on manipulating processing parameters. This includes control of particle size, size distribution, and the reduction of particle agglomeration.

1.7.1 Precipitation:

Uniform particles are usually prepared by homogeneous precipitation reactions in a process that involves the separation of the nucleation and growth of the particle nuclei. (Figure 1.23) In a homogeneous precipitation, a rapid nucleation occurs when the solute concentration obtains a critical supersaturation point. Then, the newly formed nuclei are permitted to grow in a uniform manner by diffusion of the solute from the solution to the surface until a final crystallite

size is formed. In order to achieve particles with a uniform size distribution, the process of nucleation and growth should be separated as described by the model put forth by LaMer and Dinegar (curve I of Figure 1.23).[49]

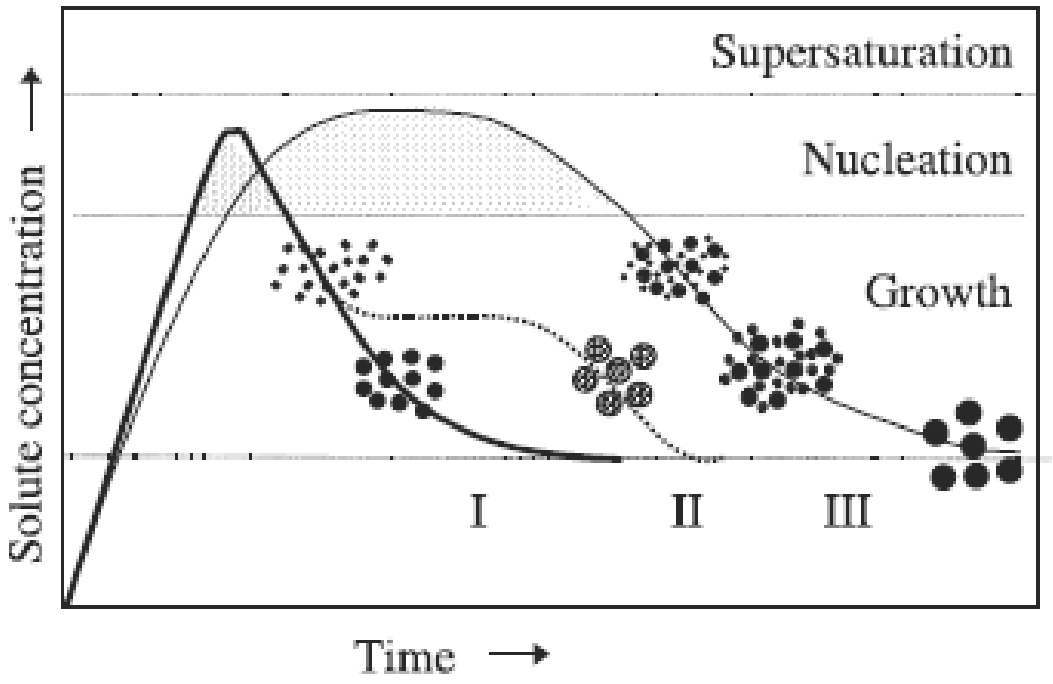

Figure 1.23. Mechanism of formation of uniform particles in solution: (I) single nucleation and uniform growth by diffusion. (II) nucleation, growth and aggregation of smaller subunits (III) Oswald ripening growth.[49]

According to this theory, the formation of nanoparticles should be arranged in such a way that all nucleation takes place in a very short period. Then, more solute can be slowly supplied so that it will grow the newly formed particle without the new material reaching supersaturation, which could promote further nucleation. An artificial separation between nucleation and growth processes may be achieved by seeding. In this process, particles are introduced into a solution containing solute particles below the critical supersaturation point.[49-50]

In Oswald ripening, (curve III of Figure 1.23) energetics favors the formation of larger particles at the expense of the smaller particles. This is a thermodynamically driven process based on the fact that molecules on the surface are less stable than the ones in the interior. For example, in a cubic crystal of atoms, the atoms that are bonded to six neighboring atoms in the interior are quite stable, whereas the atoms on the surface are only bonded to five or fewer atoms are less stable. As the system tries to lower its overall energy, atoms on the surface will tend to leave the larger particle and return back to the solution. When the solution becomes saturated with the small particles, the small particles will redeposit onto the larger particles. This shrinking and growing of particles will result in a larger mean diameter of particle sizes. As time goes to infinity, the entire population of particles becomes one large particle to minimize the total surface area. The ratio of atoms on the surface of the particles compared to the bulk is directly correlated with particle size as shown in Figure 1.24.[51]

.

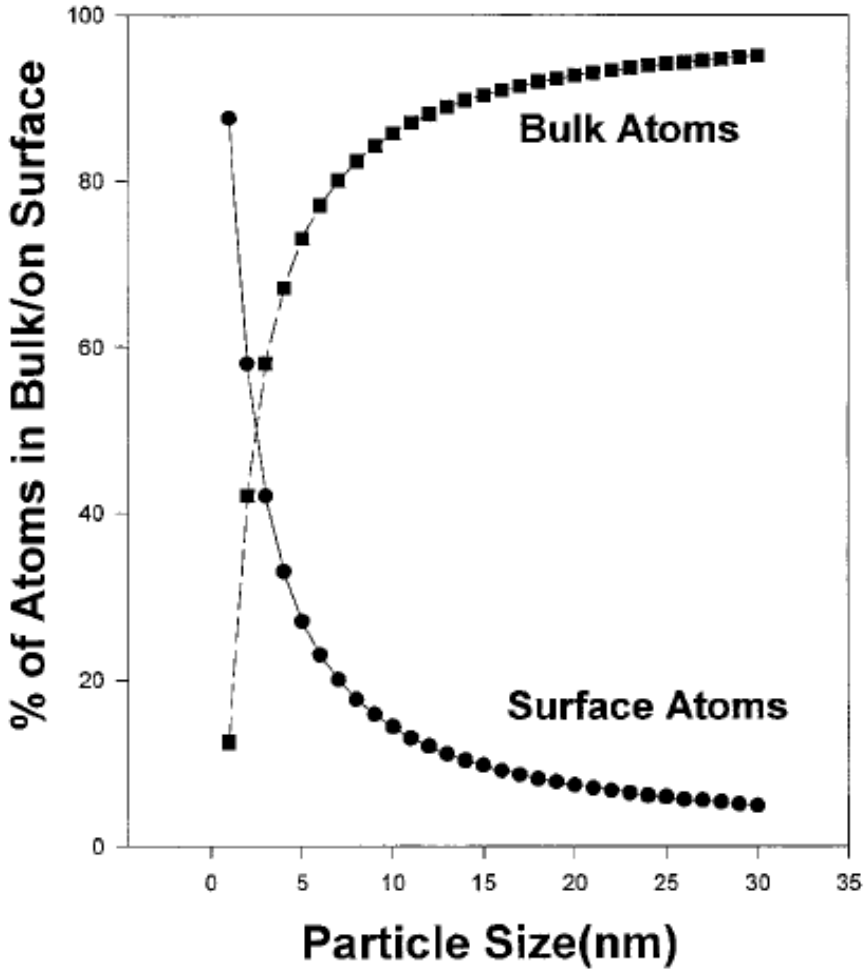

Figure 1.24. Calculated surface to bulk ratios for solid metal particles versus particle size.[51]

Therefore, larger particles with their lower surface to volume ratios, promotes a lower energy state of the solution. As the reaction progresses, the solution will lower its overall energy by the smaller particles diffusing into the larger particles. This results in an increase in the numbers of lower energy larger particles at the energy expense of the smaller particles. The end result is a solution with a more homogeneous particle size distribution. Unfortunately, as a result of the tendency of a system to lowers its overall energy, nanoparticles will often form agglomerates. Agglomeration of particles can occur during synthesis, drying, or post synthesis processing. In order to produce monodispersed particles without agglomeration, surfactants are often employed to control the dispersion during synthesis. Surfactants are commonly used during nanoparticle synthesis in order to decrease the inter-particle interaction by increasing the repulsive forces between particles. They are used to control particle size as well as shape.

1.7.2 Coprecipitation:

The coprecipitation technique is probably the simplest and most effective pathway to produce magnetic iron oxide nanoparticles. It has been know since 1852 that magnetite can be made by a coprecipitation method by the addition of a base to an aqueous mixture of ferrous and ferric salts.[52] Since that time, many investigators have produced iron oxides (either Fe_3O_4 or

γFe_2O_3) by reacting stoichiometric mixtures of ferrous and ferric salts in an aqueous alkaline medium.[53-61] The chemical reaction to produce Fe_3O_4 may be written as shown in equation (2).

$$Fe^{2+} + 2Fe^{3+} + 8OH^- \rightarrow Fe_3O_4 + 4H_2O \quad (2)$$

The thermodynamics of this reaction predict the complete precipitation of Fe_3O_4 should occur at a pH between 8 and 14, with a stoichiometric ratio of 2:1 (Fe^{3+}/Fe^{2+}) in a non-oxidizing environment. [53-56] Furthermore, it has been shown that by adjusting the pH and the ionic strength of the reaction solution, it is possible to control the average size of the particles from 2 nm to 15 nm. [57-61] There is a general trend in size reduction as the pH and the ionic strength of the reaction solution increases. The pH and the ionic strength affect the surface composition, as well as the surface charge of the particles. Together, these two parameters afford the production of small particles with a very narrow size distribution.

1.7.3 Microemulsions:

In microemulsions, micro droplets of aqueous phase are trapped within surfactant molecules that are dispersed in an organic phase. These systems are referred to as water- in- oil (W/O), or reverse micelle solutions. These surfactant micro droplets may spontaneously form nanoreactors of different sizes, micelles (1-10 nm) or water in oil emulsions (10-100 nm). Within these nanoreactors, aqueous iron salt solutions are encapsulated by surfactant molecules that separate them from the organic phase. The nanoreactor produces a confinement that limits the iron particle nucleation and growth. The first magnetic nanoparticles formed in micelles were produced by the oxidation of Fe^{2+} salts in ${}_{\gamma}Fe_2O_3$ and Fe_3O_4. [62-66] This reaction was carried out in an AOT/isooctane emulsion. The size of the nanoparticles produced can be controlled by the reaction temperature, the amount and type of surfactant, and the type of organic phase. Several types of surfactants have been used, such as cationic, anionic, or nonionic. Commonly utilized ionic surfactants are sodium bis(2-ethylhexyl)sulfosuccinate (AOT), cetyltrimethylammonium bromide (CTAB), or sodium dodecylsulfate (SDS). Nonionic surfactants include Triton X-100, Igepal CO-520, and Brij-97. [67-72] It has been discovered by several research groups that the functional groups associated with the ionic surfactants interact with the core of the nanoreactors, and this interaction limits the production of highly crystalline magnetite nanoparticles.[62-72]

1.7.4 Polyol:

In the polyol process, precursor compounds such as oxides, nitrates, and acetates are dissolved in a polyalcohol such as ethylene glycol, or diethylene glycol. The polyol utilized acts as the solvent, reducing agent, and surfactant. A typical procedure involves dissolving a precursor compound in the liquid polyol. The mixture is then rapidly stirred and heated, often to the boiling point of the polyol. During the reaction, the metal precursor becomes soluble in the polyol, forms an intermediate, and is reduced to form metal nuclei which can undergo growth to form metal particles. Nanoparticles such as Fe, Co, Ni, Ru, Rh, Pd, Ag, Sn, Re, W, Pt and Au have been synthesized using different precursors by this method.[73-81]

Although various methods of synthesis exist, the polyol process, which is a focus of this dissertation, offers several advantages. First, the surface of the nanoparticle prepared by the polyol method is coated with a hydrophilic shell; therefore, the nanoparticle can be easily dispersed into aqueous solvents. This is a basic characteristic required for most biological applications. Second, the high reaction temperatures employed in a polyol reaction favors particles with a higher crystallinity and therefore a higher magnetization. Lastly, the particle size distribution of the nanoparticles produced by this method is narrower than particles produced by other traditional methods.[82-89] While different polyols are chosen depending on the reduction

potential of the metals, for the work in this dissertation, the readily available and inexpensive propylene glycol, ethylene glycol and diethylene glycol were used to produce a series of ferrites of cobalt and nickel. (Figure 1.25)

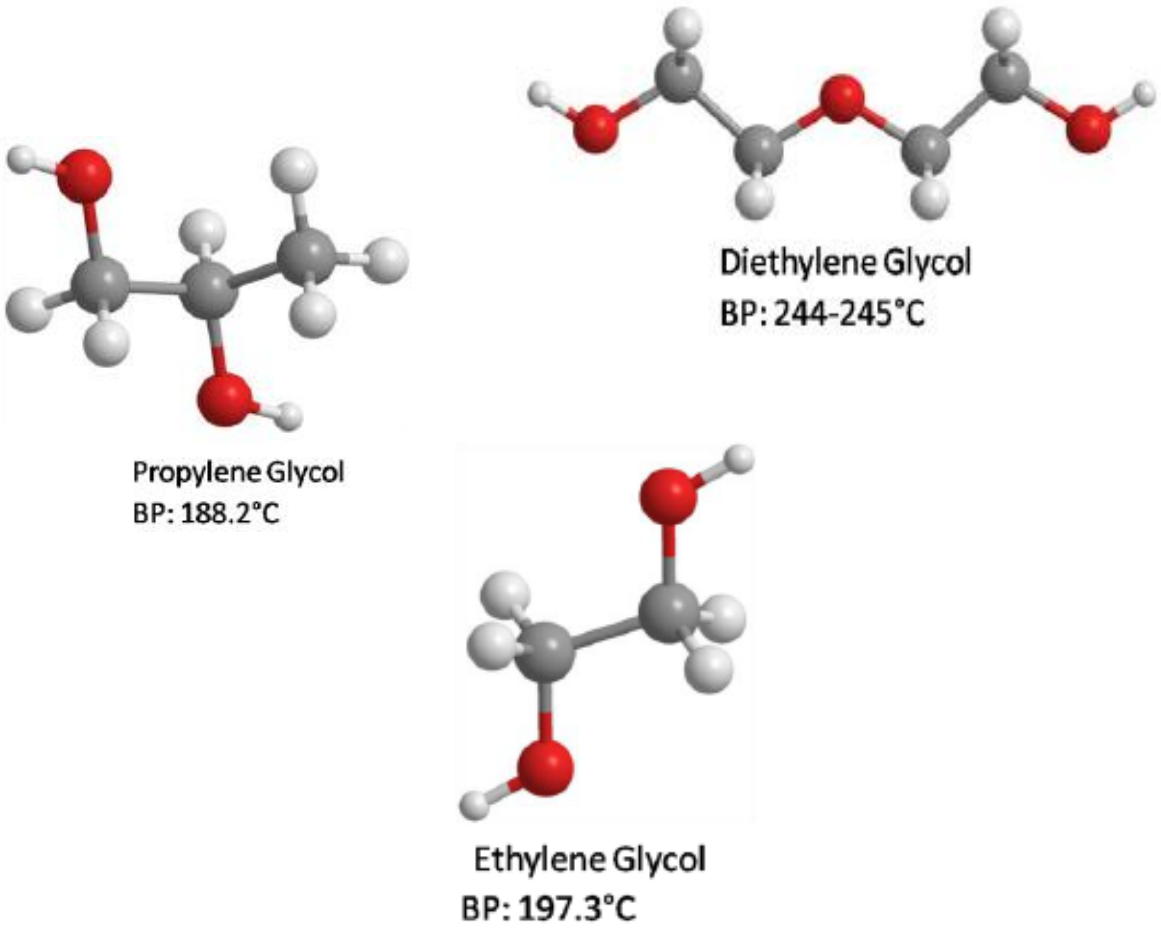

Figure 1.25. Various polyols utilized in the synthesis of mixed metal ferrites showing their respective boiling points.

1.8 Stabilization of Magnetic Particles:

The stabilization of the iron oxide nanoparticles is critical in order to obtain particles that are stable against aggregation in biological applications. The hydroxyl groups on the surface are the functional groups of the iron oxides. These surface hydroxyl groups may be coordinated to one, two, or three iron atoms in the nanoparticle as shown below in Figure 1.26.[36]

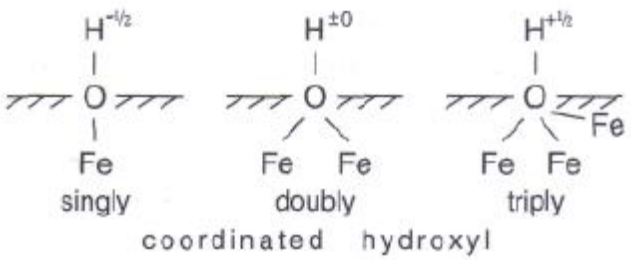

Figure 1.26. Hydroxyl groups coordinated to Fe via one, two, or three Fe atoms.[36]

These hydroxyl groups have two lone pairs of electrons along with a dissociable hydrogen atom that allows iron oxide particles to act like an acid or a base. Therefore, iron oxide particles are amphoteric, and as a result of this amphoteric behavior, knowledge of the surface charge is critical to the stabilization of iron oxide particles, and also their reactivity with other ligands.

The liquid layer that surrounds a nanoparticle with a charged surface consists of two parts; an inner region called the Stern layer, where the ions are strongly attached, and an outer diffuse region where they are loosely attached, as shown in Figure 1.27.[158] Within the diffuse layer, there is a boundary inside where the ions and particles form a stable arrangement. When the nanoparticle moves in the solution, ions within the boundary move it. The ions beyond the boundary stay behind in the bulk fluid. The potential at this boundary, or surface of hydrodynamic shear, is termed the zeta potential.[158] The magnitude of the zeta potential predicts the stability of the colloidal system. If all of the particles in a suspension have either a large negative or positive zeta potential they will repel each other and there will be very little tendency for the particles to coagulate. As a general rule, the line between a stable and unstable suspension is generally at either less than -30 mV or greater than +30 mV.

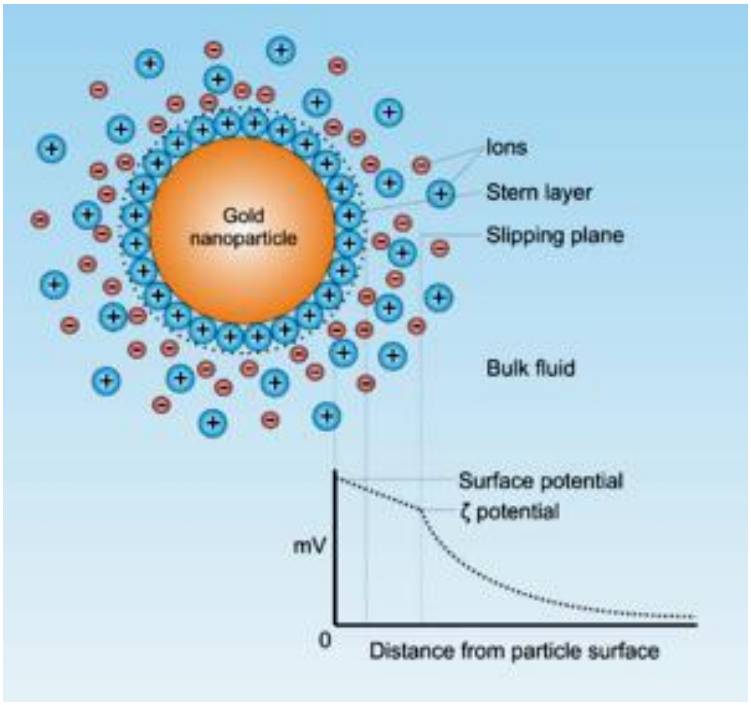

Figure 1.27 Illustration showing the Stern layer and zeta (ζ) potential of a gold nanoparticle.[158]

In aqueous solutions, the pH is one of the most important factors that affects the zeta potential. For each iron oxide, there is a pH at which the charge on the surface is zero. This is referred to as the point of zero charge or the isoelectric point.[36] At this point, the amount of adsorption of positively charged entities equals that of negatively charged entities. In general, iron oxides have a point of zero charge in the pH range 6-10.[36] When the pH is less than the point of zero charge, the predominate group on the surface will be $FeOH_2^+$. There will still be some FeO^- located on the surface, it is just that there will be a greater excess of $FeOH_2^+$. At the point of zero charge, the number of $FeOH_2^+$ will equal the number of FeO^-. As the pH increases, the number of FeO^- groups increase as shown in Figure 1.28.[36]

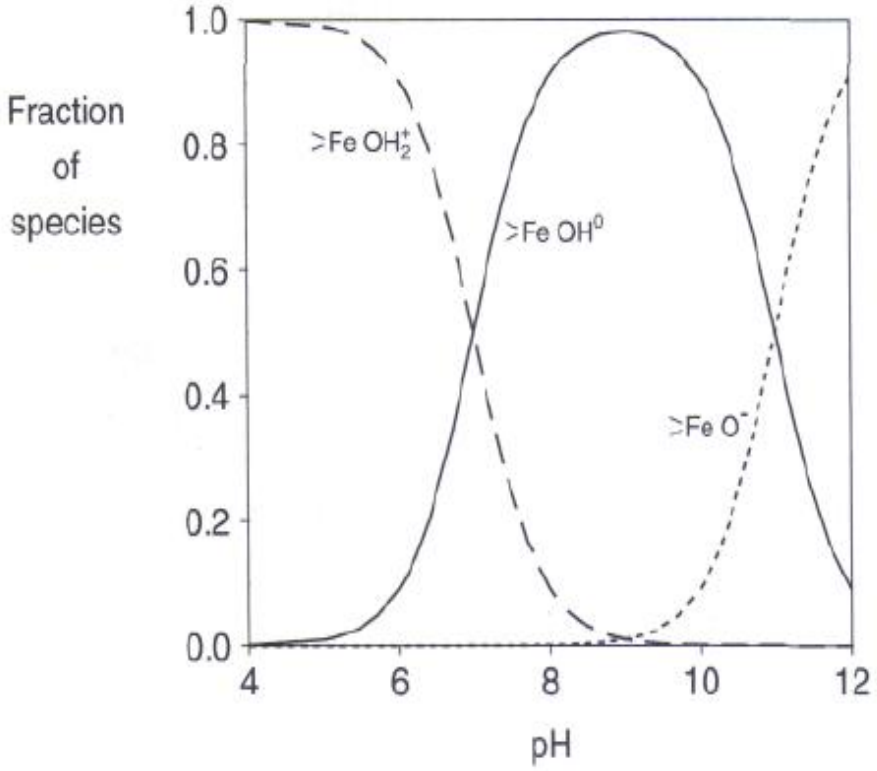

Figure 1.28. Schematic representation of the distribution of the positive, negative, and neutral surface hydroxyl groups on an iron oxide surface.[36]

The stability of the particles results from the equilibrium between two basic forces, attractive and repulsive.[90-91] Stabilization can be easily achieved by taking advantage of these forces by encapsulation of the particles in organic and inorganic matrixes. Controlling the strength of these forces is a major parameter in order to produce particles with good bio-stability. Inorganic and organic coatings have been prepared by precipitation and surface reactions. By careful selection of experimental conditions, this method can produce uniform coatings, and therefore lead to monodispersed magnetic composites. One of the most promising techniques for the production of magnetic composites is the layer by layer (LBL) method.[92] (Figure1.29) It consists of the continuous stepwise adsorption of charged polymers and oppositely charged polyelectrolytes onto the surface of the particles for a layer by layer buildup onto the particles. Using this method, particles have been coated with alternating layers of polyelectrolytes, nanoparticles, and proteins.[92]

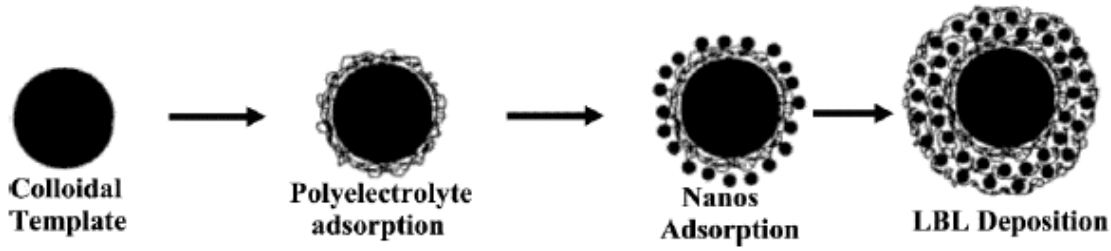

Figure 1.29. Schematic illustration of the layer by layer (LBL) electrostatic assembly method by the stepwise adsorption of charged polymers and oppositely charged polyelectrolytes onto the surface of particles.[92]

Organic polymers coated onto magnetic nanoparticles yields particles with important properties that uncoated particles lack. Polymer coatings reduce susceptibility to leaching, protect the particle surface from oxidation, and enhance the biocompatibility by reducing toxicity. Several approaches have been developed to coat iron oxide nanoparticles, including *in situ* coatings and post synthesis coatings. The most common coatings are dextran, carboxymethlated dextran, carboxydextran, starch, arabinogalactan, glycosaminoglycan, sulfonated styrene-divinylbenzene, polyethylene glycol, polyvinyl alcohol, poloxamers, and polyoxamines.[93-97]

Iron oxide particles have been coated with silica, gold, and gadolinium.[97-107] These inorganic coatings not only make the nanoparticles more stable in solution, they also provide a surface to bind various biological ligands to the surface of the particle. Surface silanol groups can easily react with various coupling agents to covalently attach specific ligands to the nanoparticles. Silica coatings have been extensively studied.[108-114] Silica prevents particle aggregation, improves chemical stability, and provides protection against toxicity. Three different methods have been developed to produce silica-coated nanospheres. The first method is based on the well-known Strober process, in which silica is formed in situ through the hydrolysis and condensation of a precursor, such as tetraethylorthosilicate (TEOS).[115-120] The second method is based on the deposition of silica from a silicic acid solution.[121] Several studies have shown that the silicic acid method appears to be more effective in covering a greater proportion of the magnetic surface than the TEOS method.[122] This technique is very easy to carry out, and the particle size can be

controlled from tens to hundreds of nanometers by changing the ratio of SiO_2/Fe_3O_4 or just simply repeating the coating procedure. The third method is an emulsion method, in which micelles are used to confine and control the silica coating.[123-125] Gold is another inorganic coating that not only promotes stability; it also imparts functionality for binding various ligands.[126-127]

The chemistry of iron nanoparticles is dominated by its robust reactivity with air. Finely divided iron has long been known to be pyrophoric. Controlling this extreme reactivity has been a subject of great interest for a number of years, and the stabilization of iron nanoparticles is critical to obtain magnetic colloidal liquids that are stable against aggregation in biological applications. As a result of this required stability, several research groups have alloyed iron nanoparticles with a less reactive metal. The most notable is the formation of iron-platinum nanoparticles. Coating the iron particles with a nonreactive shell to serve as an oxygen barrier is another method, and has led to iron particles coated with gold, gadolinium, and magnesium.[101-106] Gold is an ideal coating due its inertness towards oxidation, and it can be easily functionalized with a myriad of commercially available thiols. Iron nanoparticles coated with gold have been attempted a number of times, but result in weakly magnetic particles.[101-103] Magnesium coatings had little effect on magnetic saturation, but greatly altered coercivities.[105-106] Other inorganic coatings that are beginning to emerge are nickel and cobalt. The procedure for coating iron nanoparticles with nickel and cobalt has been attempted by several groups that use a coprecipitation technique.[128-129] The work presented in this dissertation has provided valuable

information about the synthesis and characteristics of alloyed iron nanoparticles of nickel and cobalt produced by the polyol process.

1.9 Biological Applications:

Magnetic iron oxide nanoparticles offer a wide array of possibilities in a multitude of biological applications. They have size ranges that are controllable ranging from a few nanometers up to hundreds of nanometers. These size ranges place magnetic iron nanoparticles at dimensions that are either smaller or comparable to those of a cell, a virus, or a protein. Since nanoparticles are of comparable size to a biomolecule of interest, they can interact with or bind to an entity, thereby providing a controlling means of labeling or tagging. Iron nanoparticles also have the added benefit of being superparamagnetic, which allows them to be easily manipulated by an external magnetic source.

1.9.1 MRI

Although a lot of materials research is focused on producing novel materials, a large amount of research is application driven. For example, researchers are seeking to improve magnetic resonance imaging contrast enhancement, and cell separations, both of which the second part of this work addresses. The synthesis of magnetic nanoparticles has made substantial progress, and the polyol process, as discussed previously, has the advantage of producing particles with higher crystallinity and higher magnetization than particles produced by coprecipitation. These magnetic nanoparticles are able to efficiently shorten T_2 and T_2* of water protons.[131] (Figure 1.30)

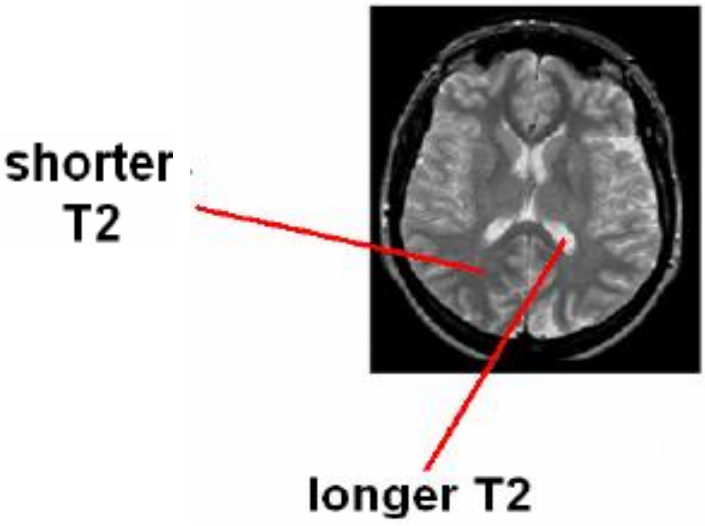

Figure 1.30. MRI image detailing the contrast between white and gray matter created by the natural differences in T_2 decay relaxation times of brain tissue.[131]

The contrast generation is related to the magnetic properties of the particles that induce a strong magnetic susceptibility effect on the water protons that diffuse around the particle. The T_2 relaxation of the particles is mainly controlled by their size, which ranges between 60 nm and 250 nm. Smaller particles (20 nm - 50 nm) are characterized by a lower relaxation.[130-133] The role played by the size of the particles introduces the first challenge to the synthesis process. The synthesis of ferrite particles of a defined size is often a difficult process to control mainly as a result of the colloidal nature of the ferrite. Therefore, the search for experimental conditions that produce a monodisperse population of particles is still a very active area of research. The work presented here will show how reaction time in the polyol can be an effective method of controlling particle size. Another challenge is the design of a particle with a high degree of crystallinity of the ferrite core. The crystallinity of the core is proportional to the magnetization of the particle, and therefore the efficiency of the particle as a MRI probe.

1.9.2 Cell Separations:

Cell separations, or more specifically immunomagnetic separations, allow analysts a rapid, inexpensive, and easy to use methodology in order to investigate microbial concentrations.

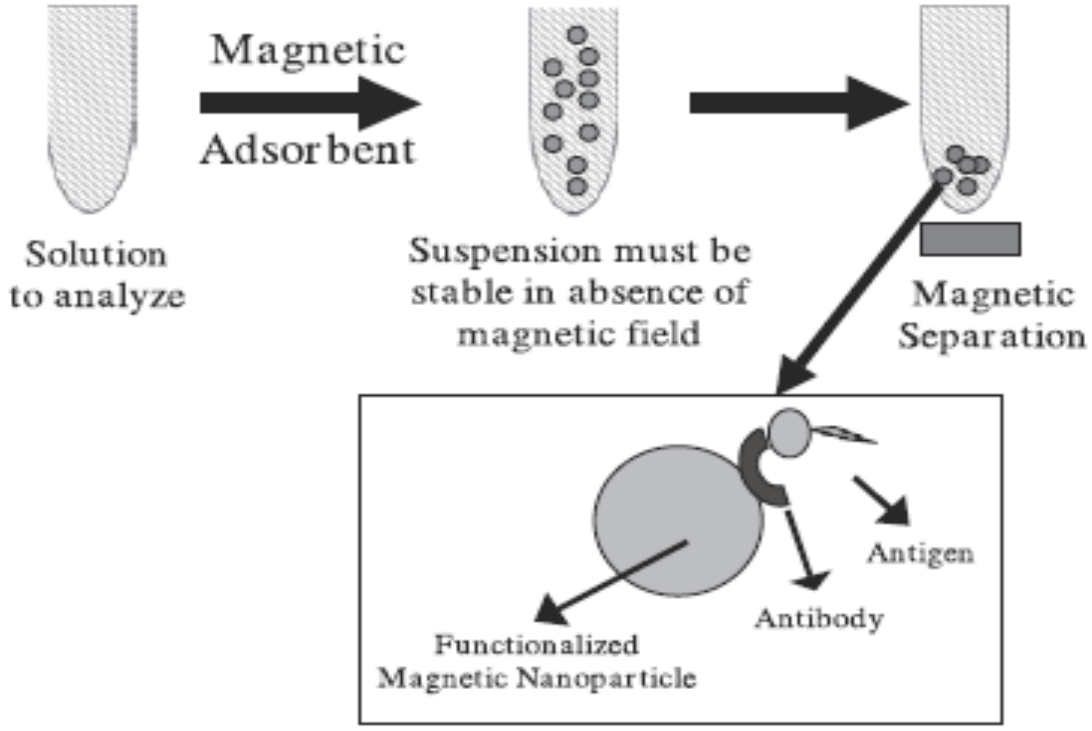

Figure 1.31. Schematic showing the various steps involved in immunomagnetic separations.[130]

Commercially prepared magnetic beads can be used to extract targeted bacteria from complex matrices such as food.[130] These beads consist of an iron core, a polystyrene outer coating and an antibody specific to the bacteria of interest bound to the polystyrene shell. To extract the target, the beads are mixed with the food. After thorough mixing, an external magnetic field is used to sequester the bead bound bacteria from the food matrix. With the bacteria bound to the bead and in the presence of the magnetic field, the interfering matrix is physically removed. Upon removal of the matrix, the magnetic field is disabled and the remaining material can be analyzed using traditional microbiological techniques.[130] (Figure 1.31) Commercial beads are effective at removing bacteria from food in high concentrations; however, only a small amount of iron is used in these beads. As a result, the lack of both magnetic moment and responsiveness to applied magnetic fields can cause cross-reactivity with the target and interfering bacteria which reduces the specificity of the extraction. A nanoparticle with a greater magnetic moment and reduced size would provide greater sensitivity based on engineering alone. The smaller size would allow better mixing in the matrix and the greater magnetic moment would allow for better and more uniform extraction.

To test this theory, iron oxide nanoparticles were synthesized in this work by a modified polyol technique, coated with a functionalized silane surface, and modified with monoclonal anti-*E. coli* O157:H7 antibodies. The resulting extracts were analyzed by MALDI/TOFMS to evaluate specificity, sensitivity and overall performance. In summary, a nanoparticle was designed and

implemented for the immunomagnetic isolation of pathogenic bacteria. This product provides a clean extract with added sensitivity over commercially available materials. Furthermore, the nanoparticle extraction followed by mass spectrometry could provide a valuable and rapid tool for the analytical determination of *E. coli*.

The next several chapters will address each area of research covered by this dissertation. Chapter 2 will discuss the polyol method of producing nanoparticles. Chapter 3 will cover the interesting properties of the mixed metal nanoferrites of nickel and cobalt, as well as a novel synthetic approach that avoids the use of organic capping agents. Also presented in Chapter 3 is a detailed post-synthesis metal analysis of the produced ferrites which is often omitted in the literature. Chapters 4 and 5 will examine the biological applications of these particles, first as a rapid cell separation methodology in Chapter 4 and then as a magnetic resonance imaging enhancement probe in Chapter 5. Chapter 4 describes a novel rapid approach to the identification of the pathogenic *E.coli* O157:H7 using nanoparticles. Also presented in Chapter 4 is a detailed analysis of the binding efficiency of the anti-*E. coli* O157:H7 antibodies to the particles, which is currently not found in the literature. Finally, Chapter 6 will offer some insights, implications and potential future work resulting from the novel work completed in this dissertation regarding the use of iron oxide nanoparticles as a packing matrix for ultra high pressure liquid chromatography.

Chapter 2: The Polyol Process

2.1 Introduction

The polyol process dates back to 1989 with a paper describing a new process for the preparation of micron and submicron powders of easily reducible metals by the French chemist Fernand Fievet.[134-135] In this process, precursor compounds such as oxides, nitrates, and acetates are dissolved in a polyalcohol such as ethylene glycol, propylene glycol, diethylene glycol, trimethylene glycol, and tetraethylene glycol, as shown in Figure 2.1. The polyol utilized acts as the solvent, reducing agent, and surfactant. One of the interesting characteristics of this process is that the reduction reaction takes place through the solution rather than in the solid state. This offers control of the reduction process by the separation of the nucleation and growth steps. A typical procedure involves dissolving a precursor compound in the liquid polyol, reduction of the dissolved metallic species by the polyol, and finally homogeneous nucleation and growth of the metal particles in the polyol.

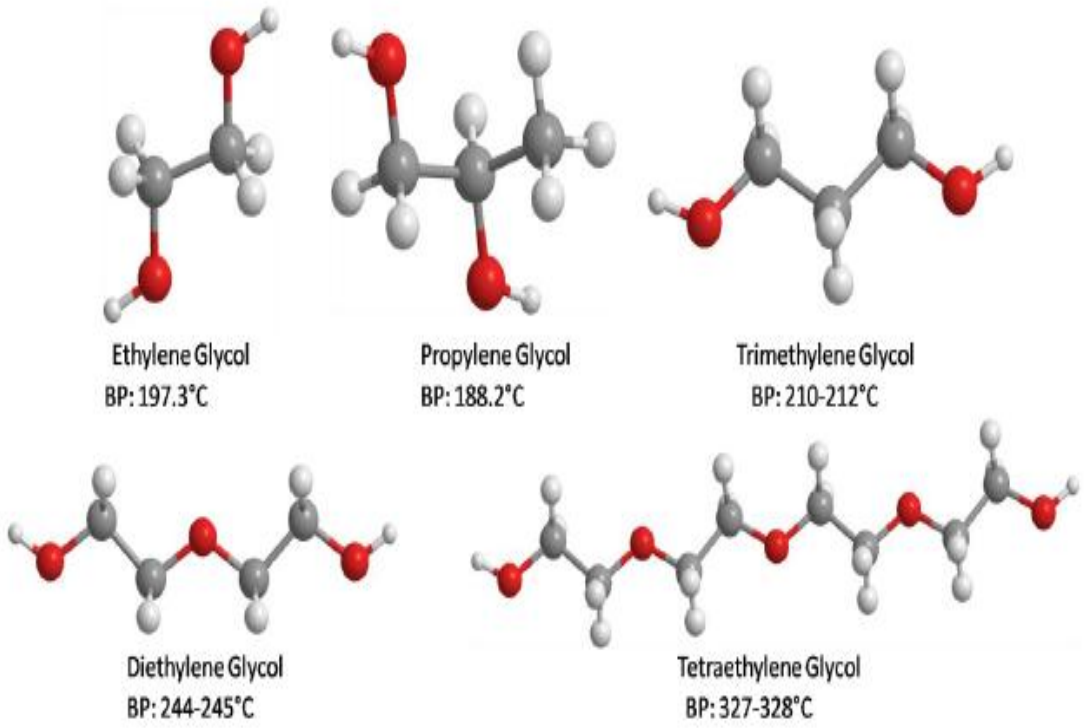

Figure 2.1 Polyols used for the reduction of metal salt precursors with their boiling points.

A multitude of metallic powders can be produced by the reduction of a suitable precursor in polyols. Previous studies have demonstrated that nanoparticles such as Fe, Cu, Co, Ni, Ru, Rh, Pd, Ag, Sn, Re, W, Pt and Au have been synthesized using different precursors by this method.[72-88] Therefore, I initially carried out a series of experiments on several different copper and silver precursors in three different polyols, propylene glycol (boiling point 188.2 ^{o}C), ethylene glycol (boiling point 197.3 ^{o}C), and diethylene glycol (boiling point 244.6 ^{o}C). Since silver has a more positive reduction potential (+0.80 V) than copper (+0.34 V), the reduction of silver was investigated first in ethylene glycol, followed by copper.

2.2 Synthesis of Silver Nanoparticles

All chemical used were reagent grade. Ethylene glycol and silver nitrate were purchased from Fisher Scientific. The synthesis of silver powders by the polyol process involves adding silver nitrate in a concentration range of 0.020 M to 0.20 M to ethylene glycol under rapid stirring. The temperature of the ethylene glycol solution can begin at room temperature, or it can be preheated to any temperature up to the boiling point of the ethylene glycol (197.3 ^{o}C). The reaction time and the percent yield of the silver are directly related to the initial temperature of the ethylene glycol. Under these conditions, the best range of temperatures was found to be between 160 ^{o}C and 180 ^{o}C. When the reaction temperature is less than 150 ^{o}C, the percent yield of silver metal was found to be less than 8%. At 170 ^{o}C, the percent yield increased to over 65%. By

increasing the reaction time from thirty minutes to two hours, the percent yield of silver metal was found to increase to above 80%. When the ethylene glycol is preheated to its boiling point (197.3 ^{o}C), the reduction of the silver was observed to occur instantaneously. While an increase in the temperature of the ethylene glycol decreases reaction time and increases the percent yield of silver metal produced, the particle size distribution of the reduced metal was found to be more polydisperse as a result of particle sintering. The effect that both temperature and time have on the silver yields illustrates that the silver production is controlled by the rate of silver reduction, which increases with temperature.

The reaction sequence of utilizing ethylene glycol to produce silver powders involves the reduction of the silver, nucleation of the metallic silver, and growth of the individual nuclei. Upon the addition of the silver nitrate to the pre-heated ethylene glycol, the silver is immediately reduced to metallic silver. As the reaction progresses, the concentration of metallic silver in ethylene glycol increases, reaches a saturation concentration, and finally nucleation occurs. Spontaneous nucleation takes place rapidly with many nuclei formed, which in turn reduces the metallic silver concentration in the ethylene glycol. The nuclei then grow in uniform manner by diffusion of the solute from the solution to the surface until a final crystallite size is obtained. It is during the nucleation and growth process that particle aggregation takes place.

2.2.1 Characterization

The silver particles were characterized by x-ray diffraction (XRD) in order to determine the phase, purity, crystallinity, and size of the produced particles. About 95% of all material can be described as crystalline. When X-rays interact with a crystalline substance, a diffraction pattern is obtained. By comparing the position of the peaks in the XRD pattern to the standards provided by the Joint Committee on Powder Diffraction Standards (JCPDS) and the International Center for Diffraction Data (ICDD), the phases present in samples are easily identified.[143] The XRD pattern can also be utilized to determine the size of the particles and the crystallinity of the sample.

X-rays are produced by a beam of fast moving electrons ejected from a cathode that bombard a metal target at the anode in an evacuated tube. (Figure 2.2) Copper and molybdenum are the most commonly used metal targets, as shown in Table 2.1. These fast moving electrons eject a core electron from the target, which subsequently emit high frequency radiation as electrons in the target move to fill the ejected electron hole. The resulting beam of high frequency radiation is then filtered to allow the passage of the $K_{\alpha 1}$ and $K_{\alpha 2}$ x-rays with wavelengths of 0.15405 nm and 0.1544 nm respectively. (Figure 2.3)[144-148]

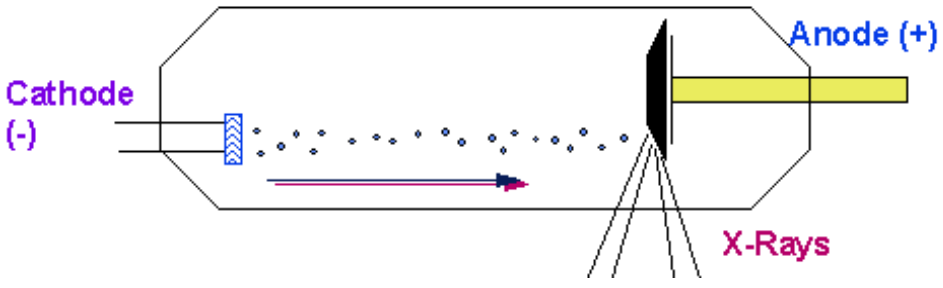

Figure 2.2 Schematic illustrating the production of x-rays by fast moving electrons.

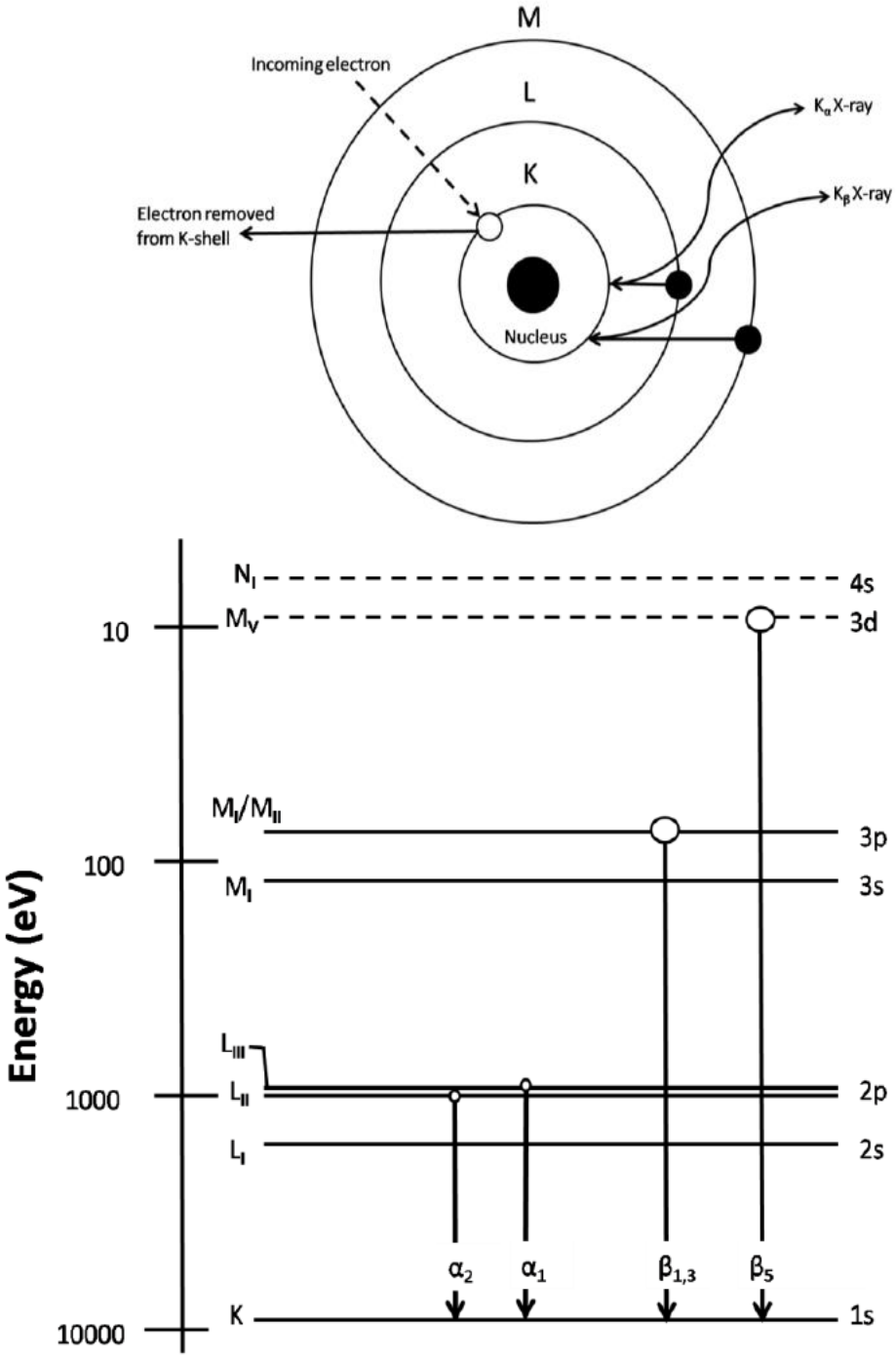

Figure 2.3 Schematic illustrating the removal of a core electron from a metal target and the subsequent emission of x-rays by the filling of the electron hole by electrons in the target (top). Each energy level in the target emits a characteristic x-ray by the relaxation process (bottom).[145]

Table 2.1 Wavelengths values of common metal target anodes measured in Å.[145]

Anode	$K_{\alpha 1}$	$K_{\alpha 2}$	K_{β}
Cu	1.5406	1.54439	1.3922
Mo	0.7093	0.71359	0.63229
Cr	2.2897	2.29361	2.08487
Co	1.78897	1.79285	1.62079
Fe	1.93604	1.93998	1.75661

When a beam of x-rays hits a material, a part of the beam will be scattered in all directions from the material (Figure 2.4) and constructively interfere in distinct directions based on the symmetry of the crystal structure (Figure 2.5). The angles where the peaks in the x-ray diffraction spectrum appear will obey Bragg's law.[146] Bragg's law states that diffraction will

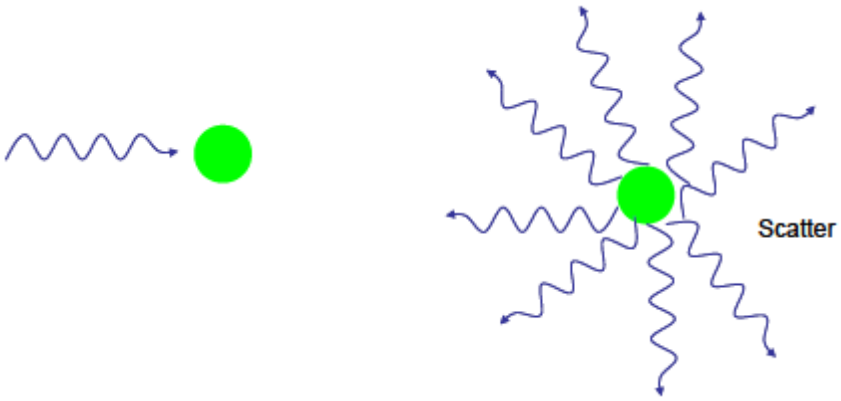

Figure 2.4 Illustration of the scattering of x-rays by a material.

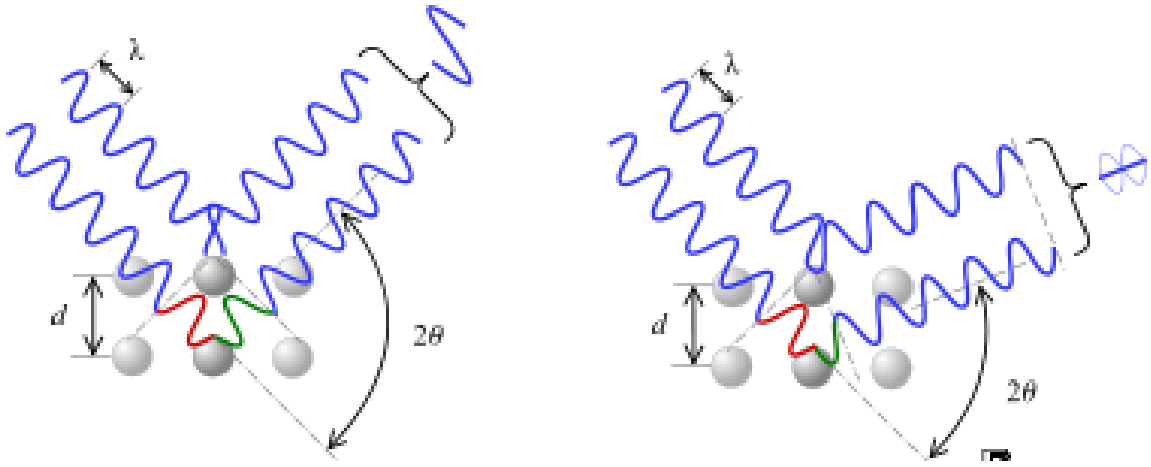

Figure 2.5 Illustration of the constructive interference of x-rays (left) and the non-constructive interference of x-rays (right).[146]

occur for specific values of θ and spacing between the crystal planes based on the equation $2d \sin \theta = \lambda$. In this equation, θ is the angle of the incident x-ray, λ is the wavelength of the x-ray, and d is the spacing between crystal planes in the sample, as shown in Figure 2.6. If Bragg conditions are not met, then the interference will not be constructive, and will produce a very low intensity diffracted beam.[147]

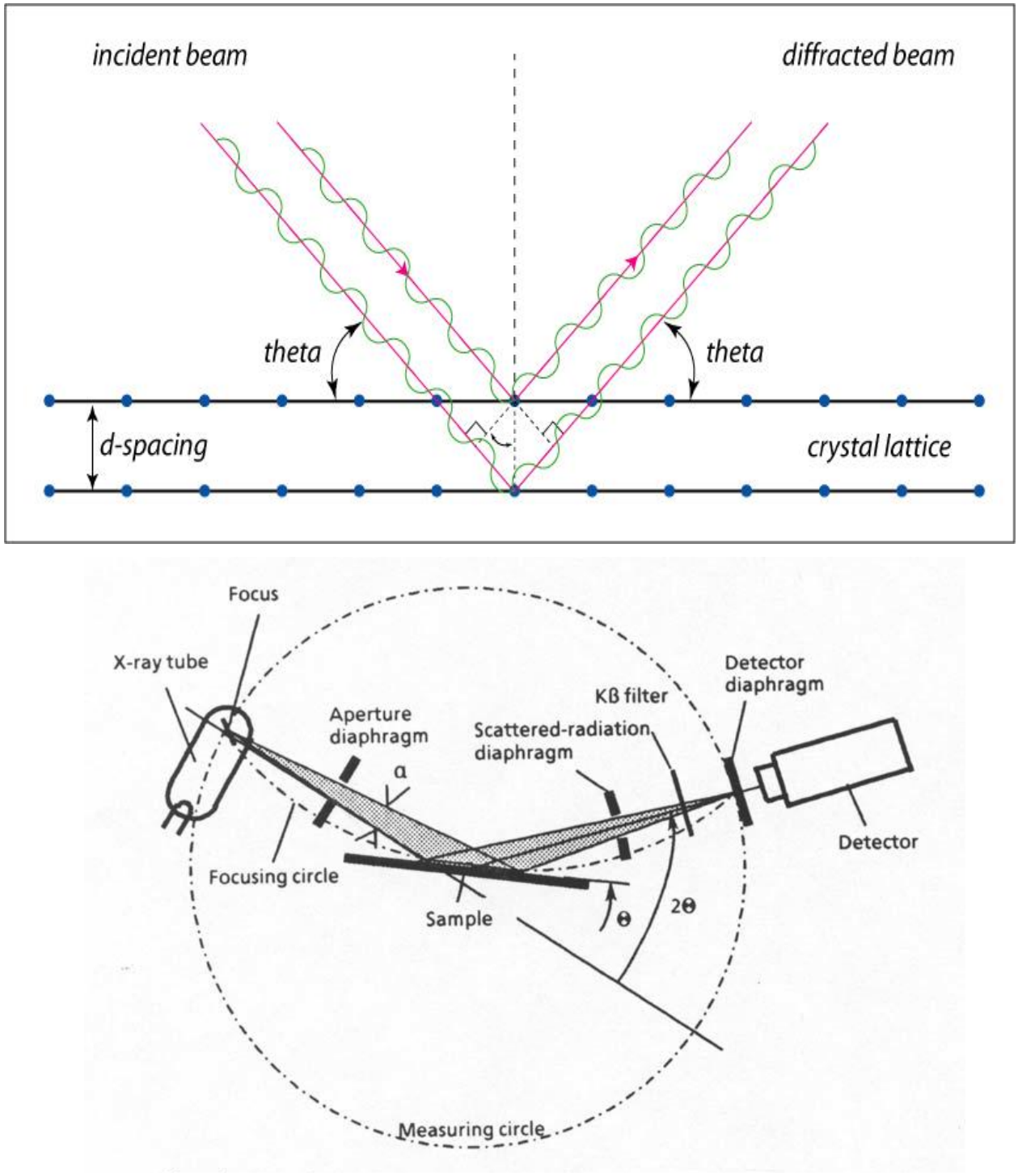

Figure 2.6 Diffraction of x-rays by the crystal lattice (top) and the schematic of a typical powder x-ray diffraction instrument (bottom).[146]

A nanoparticle sample can either be crystalline or amorphous with crystalline samples producing sharp peaks, and amorphous samples producing broad peaks on a XRD pattern. Broadening in the diffraction pattern can also be the result of the reduction of particle size or crystallite size. Peak width varies inversely with crystallite size, and therefore as the crystallite size decreases, the peaks get broader. The relationship between particle size and peak width is given below, which is referred to as the Scherrer Equation.[144]

$$B(2\theta) = \frac{K\lambda}{L\cos\theta}$$

In the Scherrer equation, B is the peak width, or more commonly known as the full width at half maximum (FWHM) of the diffraction peak, L is the crystallite size, K is the Scherrer constant, typically 0.94 for spherical particles with cubic symmetry, λ is the wavelength of irradiation, and θ is half the diffraction angle. To get the best calculations of crystallite size from the Scherrer equation, peaks between 30^{o} and 50^{o} are typically analyzed.[146]

All of the samples analyzed in this work were performed on a PANanlytical X'pert pro diffractometer at a scanning steep of 0.500^{o}, in a 2θ range from 20^{o} to 80^{o} with monochromatic CuKα radiation (λ=0.15418 nm). The data were analyzed by the Highscore plus program which contains a diffraction library based on standards provided by the Joint Committee on Powder Diffraction Standards (JCPDS) and the International Center for Diffraction Data (ICDD).[143] A typical XRD pattern of the silver nanoparticles produced by the polyol method is shown in Figure 2.7. The particles were found to have a face centered cubic structure (fcc) with four distinct peaks of 38.2^{o}, 44.4^{o}, 64.5^{o}, and 77.4^{o}. These peaks correspond to the (111), (200), (220), and (311) crystalline planes of cubic silver.

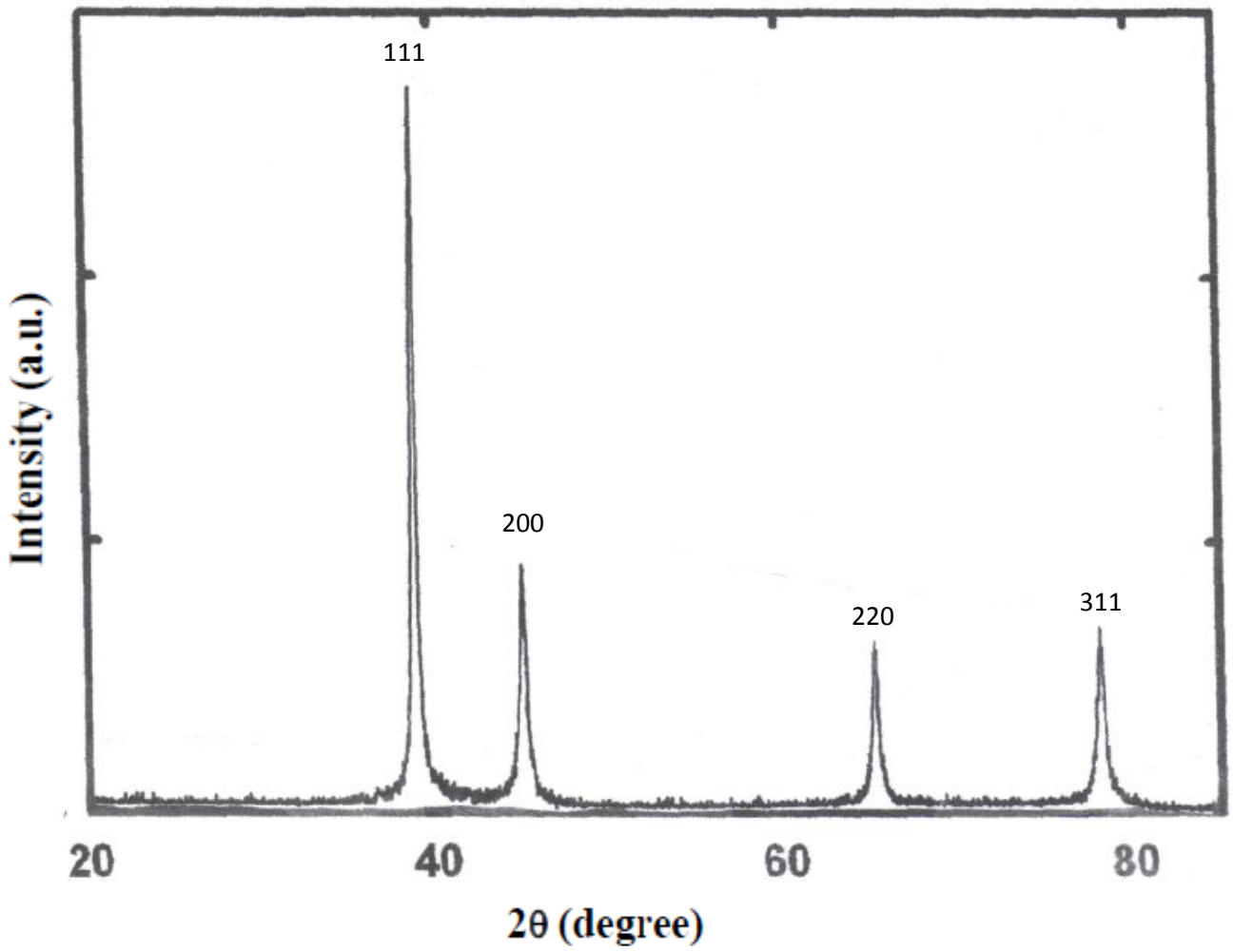

Figure 2.7 XRD pattern of silver nanoparticles produced by 0.050 M silver nitrate in ethylene glycol at 170^{o}C for 1 hour. The dried powder was analyzed on a PANanlytical X'pert pro diffractometer at a scanning steep of 0.500^{o}, in a 2θ range from 20^{o} to 80^{o} with monochromatic CuKα radiation (λ = 0.15418 nm).

Further characterization was also performed by using a JEOL JEM-1230 transmission electron microscope (TEM) at 150 kV with a Gatan Ultra Scan 4000 SP 4Kx4K CCD camera. A schematic of the JEOL JEM-1230 transmission electron microscope is shown in Figure 2.9. While light microscopy has a resolving power of about 200 nm, transmission electron microscopy can give a resolving power of 0.1 nm. Accelerated electrons behave in a vacuum just like light waves, but have wavelengths that are 100,000 times smaller than visible light. A TEM image is formed as the electrons interact with the sample in various ways. For example, absorption, diffraction, elastic scattering and inelastic scattering all contribute to the formation of the TEM image. Areas in a sample that scatter few electrons appear as bright areas in the image while areas that scatter more electrons or absorb electrons appear as dark areas as shown in Figure 2.8. Samples for TEM analysis were prepared by dispersing 7 μL of a methanol liquid suspension of particles onto a carbon film supported by carbon mesh (400 grid mesh) followed by the evaporation of the methanol. Figure 2.8 illustrates the TEM grid utilized as well as a TEM image of a typical silver powder sample produced in ethylene glycol at 170 ^{o}C. When looking at the TEM image, both light and dark regions are present. The lighter areas represent areas where the sample is less dense, and likewise, the darker regions are where the sample is more dense. From the image, it is obvious that the sample is polydisperse with a multitude of particle shapes. The multitude of particle shapes is most likely the result of particle aggregation during the nuclei growth step. Since the reaction is carried out at a relatively high temperature (170 ^{o}C), the particles are moving rapidly in the solvent and therefore the likelihood of their collision into one another is great.

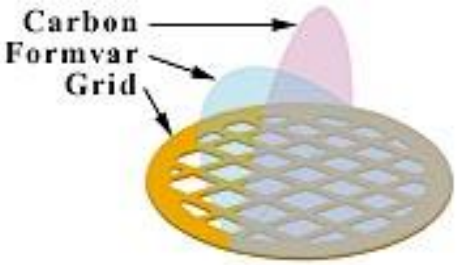

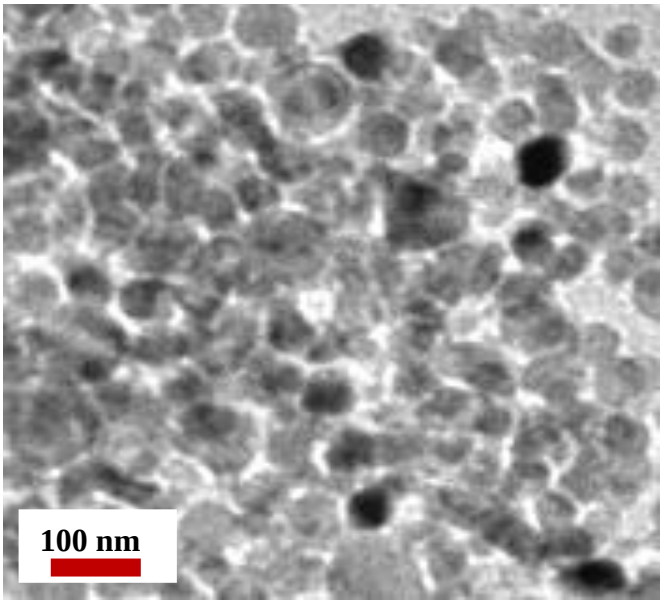

Figure 2.8 An illustration of the TEM grid utilized (top). Samples for TEM analysis were prepared by dispersing 7 μL of a methanol liquid suspension of particles onto a carbon film (400 grid mesh) followed by the evaporation of the methanol. The TEM image is of silver nanoparticles produced by 0.050 M silver nitrate in ethylene glycol at 170 ^{o}C for 1 hour (bottom).

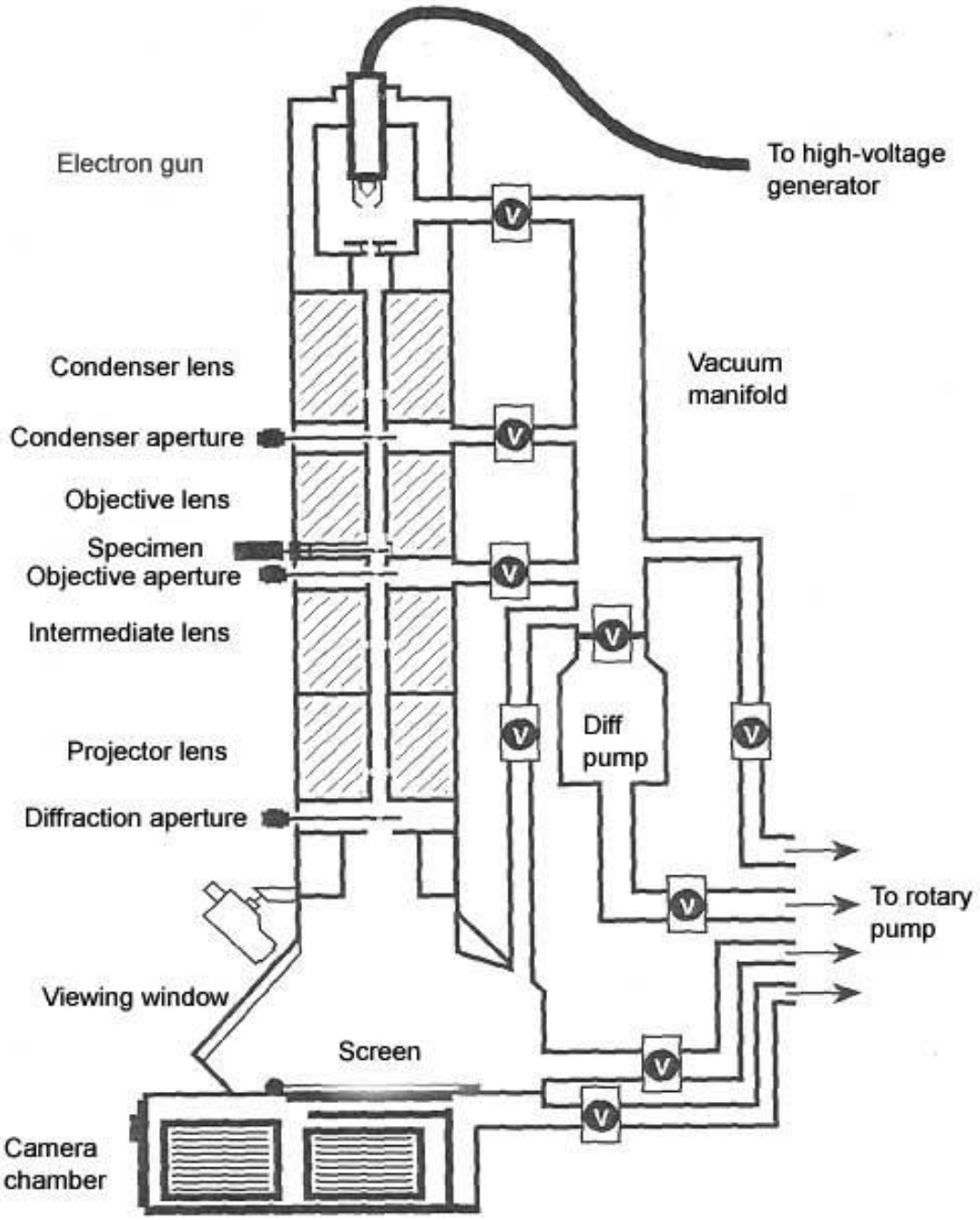

Figure 2.9 Schematic representation of the JEOL JEM-1230 transmission electron microscope.

2.3 Synthesis of Copper Nanoparticles

Micrometer sized copper particles can also be prepared by a similar polyol process as the protocol for the reduction of silver described above. There are a multitude of copper (II) compounds, such as oxides, hydroxides, acetates and sulfates, which are soluble in polyols and can be used to obtain metallic copper by reduction in solution. Two copper precursors were investigated, copper (II) oxide and copper (II) acetate tetrahydrate. The concentration range was between 0.20 M and 0.30 M in ethylene glycol. Since copper is not as easily reduced as silver, the reaction time and the temperature were increased from the 30 minutes for silver to two hours for copper, and the reaction temperature of the ethylene glycol was set at 195 ^{o}C, the boiling point of ethylene glycol. The solubility of copper (II) oxide in ethylene glycol was not adequate, even at 195 ^{o}C. Therefore, copper (II) acetate tetrahydrate was used to investigate the reduction process. The copper (II) acetate tetrahydrate was added to the polyol and then heated to reflux, or it was added at the boiling point and continued under reflux for a total reaction time of two hours. The reaction progress was monitored by observing the solution color. Initially the solution is blue-green. As the copper (II) ion is reduced to copper metal, the solution turns brown. When the copper (II) acetate is added to the polyol at room temperature, and then heated to reflux, there were no visible color changes until after thirty minutes of reaction time. When the copper (II) acetate was added to the boiling polyol, a color change was observed as quickly as ten minutes of reaction time.

2.3.1 Characterization

The copper particles were characterized by XRD in order to determine the phase, purity, crystallinity, and size of the produced particles. X-Ray diffraction was performed on a PANanlytical X'pert pro diffractometer at a scanning step of 0.500^{o}, in a 2θ range from 20^{o} to 80^{o} with monochromatic CuKα radiation (λ=0.51418 nm). A typical XRD pattern of the copper nanoparticles produced by the polyol method is shown in Figure 2.10. The particles were found to have a face centered cubic structure (fcc) with three distinct peaks of 43.7^{o}, 50.9^{o}, and 74.4^{o}. These peaks correspond to the (111), (200), and (220) crystalline planes of cubic copper. The polyol process was observed to be a very versatile and simple method to produce silver and copper particles. A TEM image of the dried copper particles is shown in Figure 2.11.

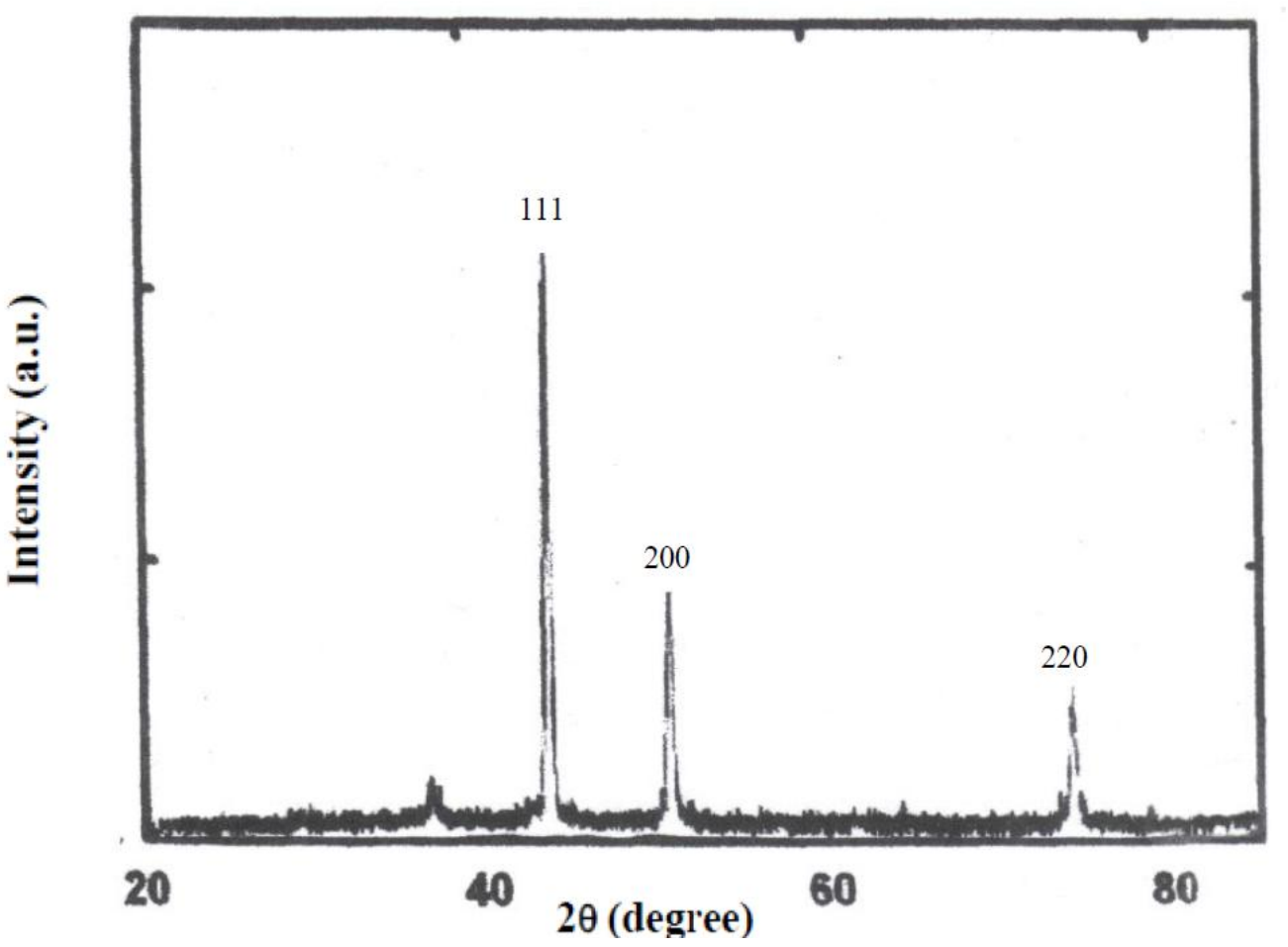

Figure 2.10 XRD pattern of copper nanoparticles produced by 0.250 M copper (II) acetate tetrahydrate in ethylene glycol at 195^{o}C for 2 hours. The dried powder was analyzed on a PANanlytical X'pert pro diffractometer at a scanning steep of 0.500^{o}, in a 2θ range from 20^{o} to 80^{o} with monochromated CuKα radiation (λ = 0.15418 nm).

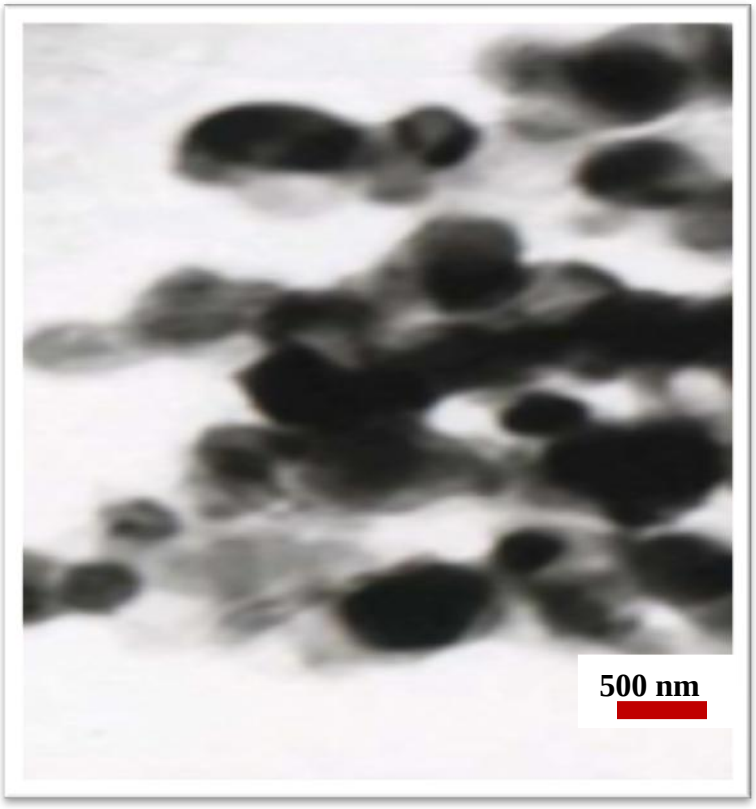

Figure 2.11 TEM image of the copper nanoparticles produced by 0.250 M copper (II) acetate tetrahydrate in ethylene glycol at 195^{o}C for 2 hours. TEM analysis was prepared by dispersing 7μL of a methanol liquid suspension of particles onto a carbon film supported by carbon mesh (400 grid mesh) followed by the evaporation of the methanol. A JEOL JEM-1230 transmission electron microscope (TEM) at 150 kV with a Gatan Ultra Scan 4000 SP 4Kx4K CCD camera was used to obtain the image.

2.4 Synthesis of Iron Nanoparticles

The reduction of iron (II) to iron metal by the polyol method requires more rigorous reaction conditions since iron (II) is more difficult to reduce than either silver or copper. The standard reduction potential of iron (II) is negative (-0.44 V) whereas the standard reduction potentials of silver and copper are both positive (0.80 V and 0.34 V respectively). It has also been reported previously in literature that the polyol process does not apply to iron.[72] Nevertheless, the polyol process for the reduction of iron (II) precursors was investigated and found to be a simple one pot process for the production of iron and iron oxide nanoparticles.

The disproportionation of iron (II) in aqueous media has been observed previously according to Equation (2).

$$4Fe(OH)_2 \rightarrow Fe + Fe_3O_4 + 4H_2O \qquad (2)$$

It has also been shown that the reaction is favored in basic solutions in the presence of weak complexing agents such as sugars or alcohols.[53-61] Alcohols are good alternatives for water as coordinating solvents with their relatively high dielectric constants and high donor numbers. Polyols are superior to regular alcohols since they are more polar, and they form a stronger coordination with metal ions. An initial experiment was designed to investigate these parameters on the production of iron and iron oxide nanoparticles by this modified polyol process.

Iron (II) chloride tetrahydrate was the iron (II) precursor, sodium hydroxide was the base, and ethylene glycol was the polyol initially studied. The procedure utilized for the iron reduction was essentially the same used for the silver and the copper described previously, except for the use of the sodium hydroxide. In a typical experiment, one gram of iron (II) chloride tetrahydrate was added to two grams of previously dissolved sodium hydroxide in a round bottom flask containing 25 mL of ethylene glycol. The solution was then heated under reflux for thirty minutes, one hour, ninety minutes, or two hours. Water was distilled off while the polyol was heated to reflux. After the reaction times described earlier, the black precipitated powder was separated from the basic polyol solution with the aid of a magnet and washed in ethanol and then water followed by a wash in acetone. The black powder was dried overnight at 80 ^{o}C. The dried black powder was found to have a mass of 712 mg. A TEM image of the dried metal nanoparticles is shown in Figure 2.12. The image indicates that the particle size distribution is fairly monodisperse with an average particle diameter around 20 nm.

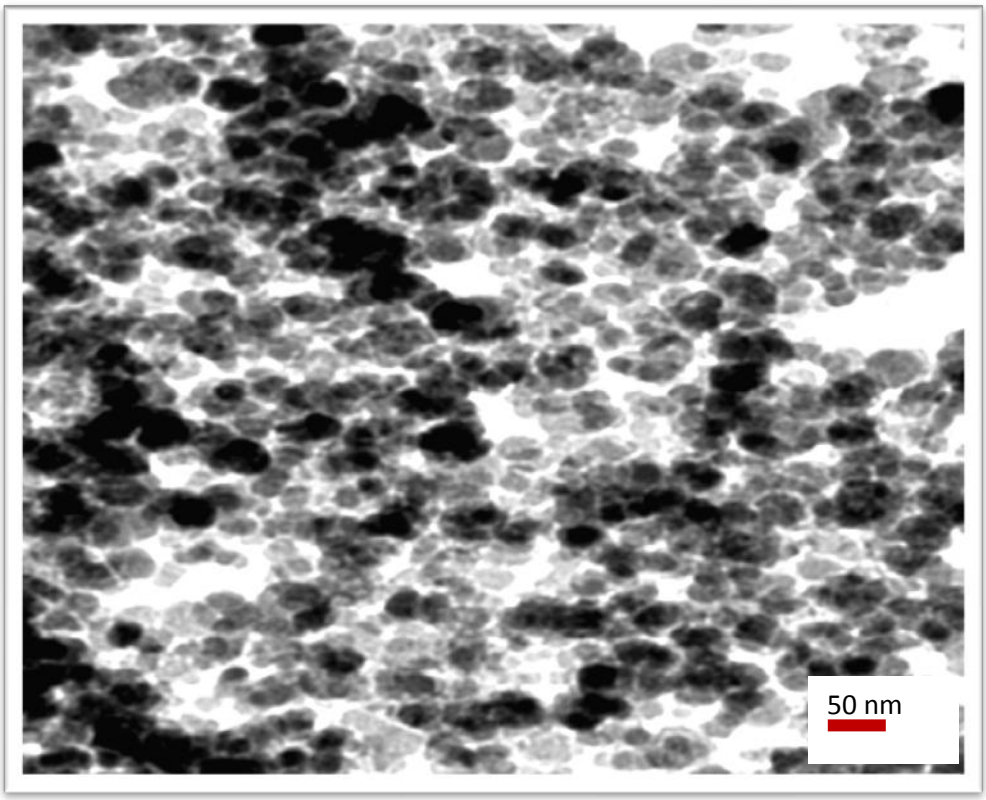

Figure 2.12 TEM image of a typical experiment involving one gram of iron (II) chloride tetrahydrate added to two grams of previously dissolved sodium hydroxide in a round bottom flask containing 25 mL of ethylene glycol.

.

2.4.1 Magnetic Characterization

The magnetic properties of the dried particles were investigated by using a vibrating sample magnetometer, or VSM. Magnetic analysis with a VSM requires a dry powder (usually 50 mg) to be placed between two pickup coils in the presence of a magnetic field. The sample becomes magnetized and therefore creates a magnetic field of its own. The sample is then vibrated at a known frequency and the modulation of the magnetic field produced by the sample will produce an electric field in the pickup coils. The current that is induced in the coils is amplified and will be proportional to the magnetization of the sample. A Lakeshore model 7300 vibrating sample magnetometer was utilized for all room temperature measurements (Figure 2.13).

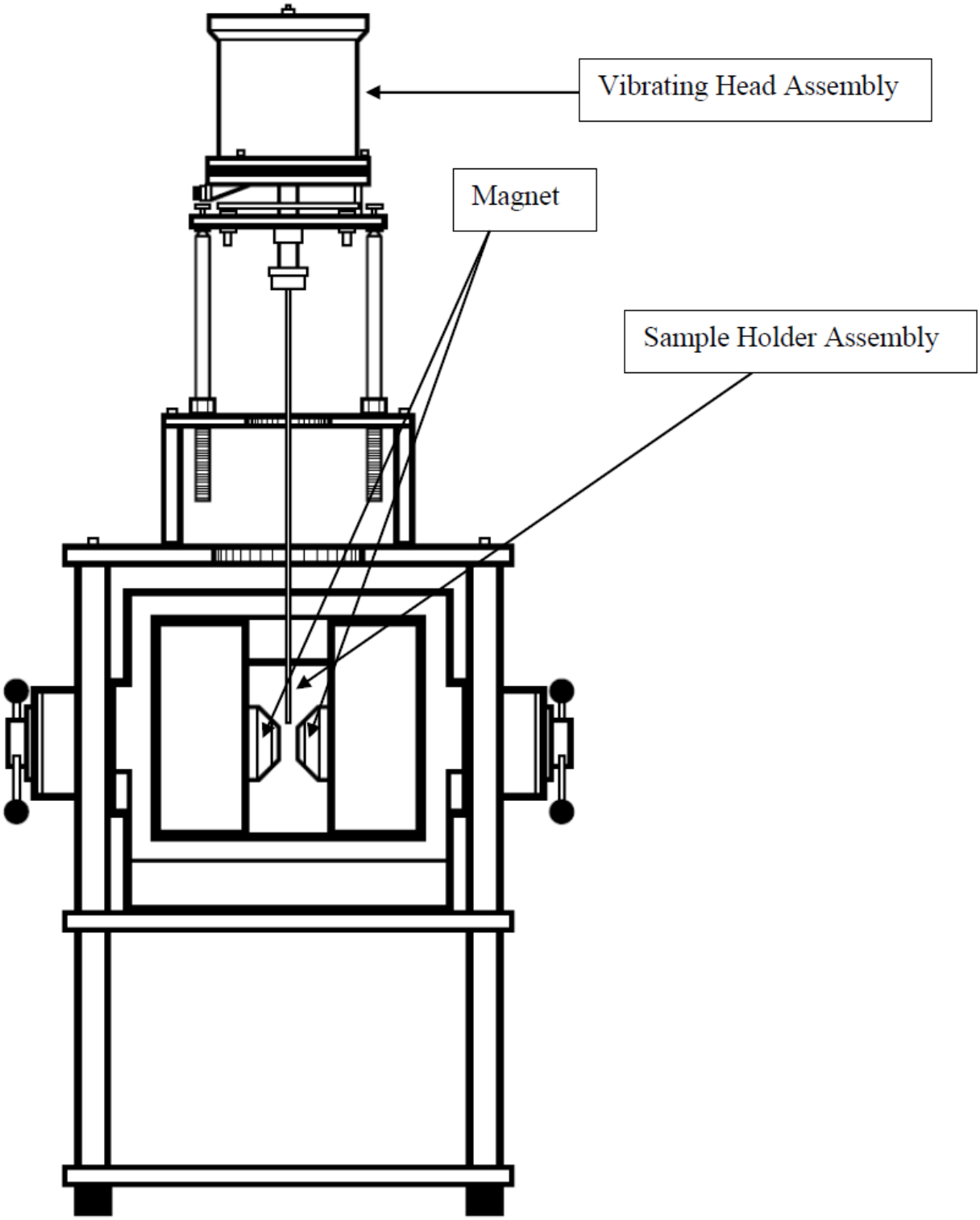

Figure 2.13 Schematic of a Lakeshore model 7300 vibrating sample magnetometer.

The saturation magnetization of the particles was found to be 76 emu/g with a coercive force of 75 Gauss (Figure 2.14). The values for bulk iron and magnetite are 220 emu/g and 130 emu/g respectively.

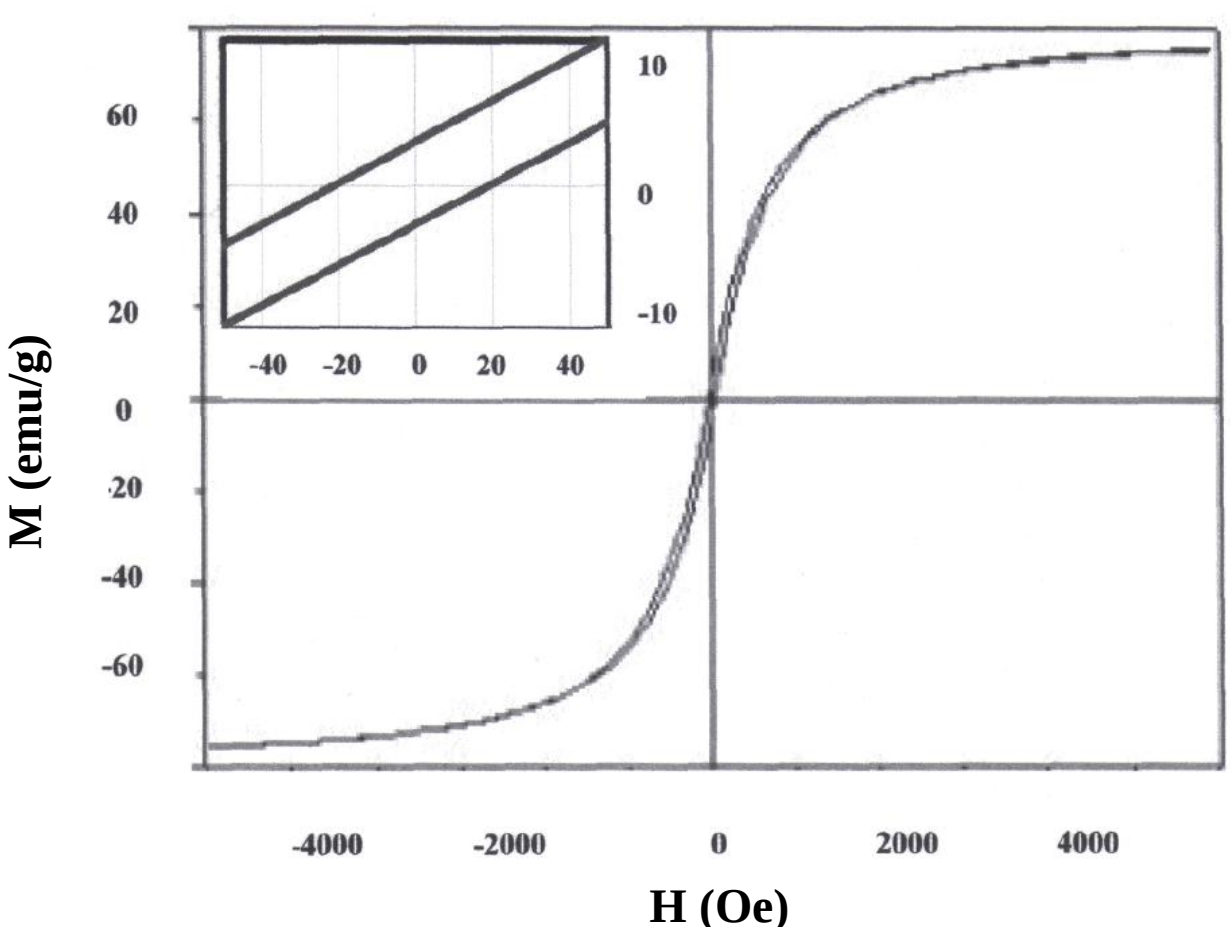

Figure 2.14 Room temperature VSM data plotted as magnetization (emu/g) versus applied field (Oe) for particles formed using one gram of iron (II) chloride tetrahydrate added to two grams of previously dissolved sodium hydroxide in a round bottom flask containing 25 mL of ethylene glycol.

Further characterization of the particles was carried out by XRD. Figure 2.15 shows an XRD plot of the dried particles. The plot shows two iron phases; one phase is a face centered cubic (fcc) magnetite (Fe_3O_4), and the other phase is a body centered cubic (bcc) α iron nanoparticle assembly. Magnetitie (Fe_3O_4) is a common magnetic iron oxide that has a cubic inverse spinel structure with oxygen forming a fcc closed packing with iron cations occupying interstitial tetrahedral and octahedral sites. Major diffraction peaks for magnetite occur at 30.125^o, 35.483^o, 37.117^o, 43.124^o, 53.501^o, and 57.033^o which correspond to the (220), (311), (222), (400), (422), and (511) miller indices respectfully. The diffraction peaks for α iron occur at 44.663^o and 65.008^o and correspond to the (110) and (200) miller indices respectively. The peaks were indexed by the International Center for Diffraction Data (ICDD) database for magnetite (fd3m, card#03-065-4899) and iron (Im3m, card#01-075-4899).[143] The average particle diameter of each phase can be estimated using Scherrer's formula. The average size of the as formed magnetite was estimated at 21 nm and the α iron was estimated at 18 nm.

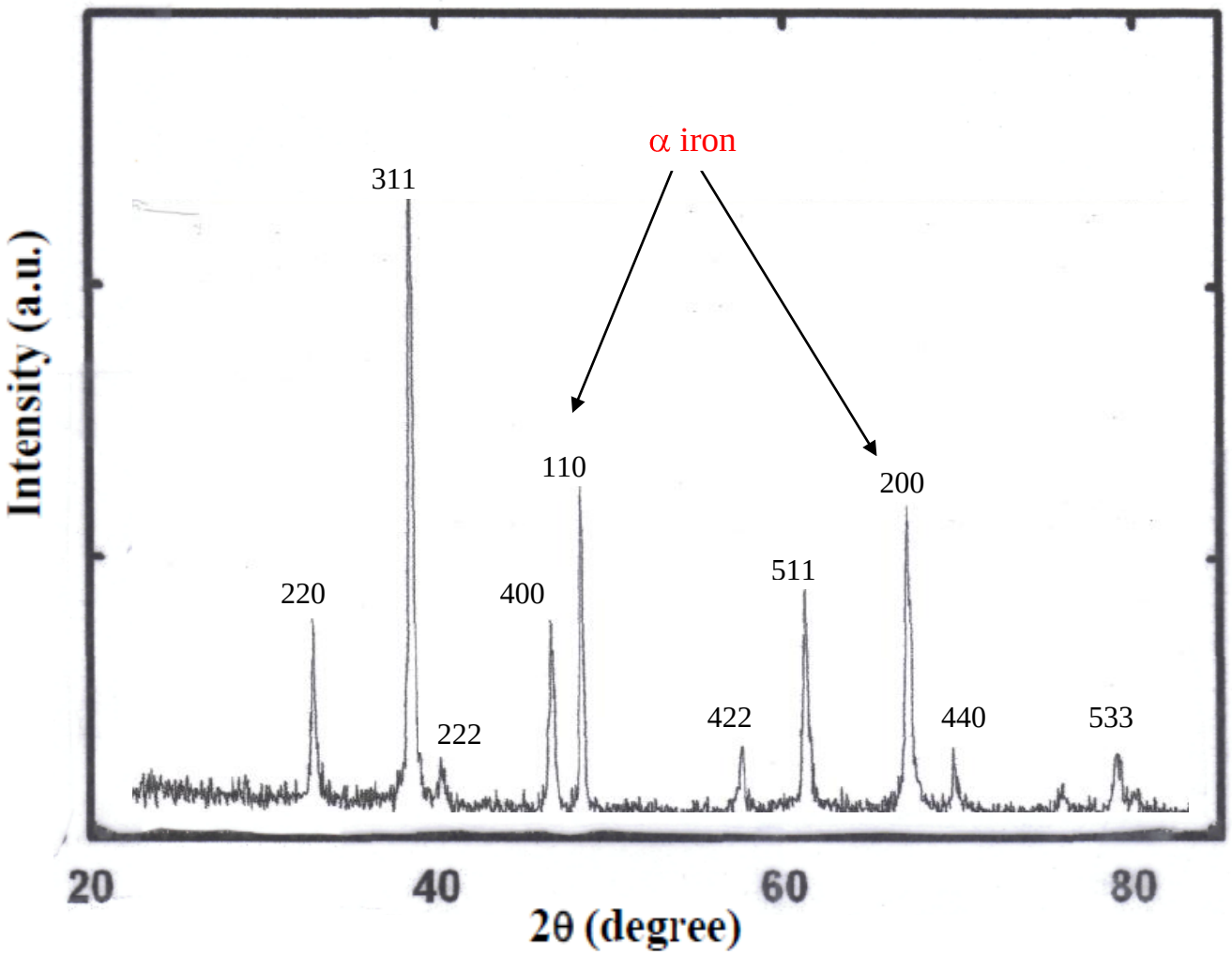

Figure 2.15 XRD pattern for particles synthesized in a typical experiment involving one gram of iron (II) chloride tetrahydrate added to two grams of previously dissolved sodium hydroxide in a round bottom flask containing 25 mL of ethylene glycol under reflux conditions.

It has been reported in the literature that α iron can be produced as the sole product without the production of magnetite as long as three experimental conditions are met.[160] First the initial concentration of the iron (II) species must be kept small, around 0.20 M. Second, the sodium hydroxide must be used in a large excess, around 2.0 M, and lastly, water must be completely removed during the reaction. Unfortunately, water is produced by polyols at high temperatures, especially with the temperatures utilized in the iron synthesis. However, if a distillation column is used instead of a reflux column, single phase α iron nanoparticles can be produced as shown by the XRD pattern in Figure 2.16. The diffraction peaks for α iron occur at 44.663 ^{o} and 65.008 ^{o} and correspond to the (110) and (200) miller indices respectively. The yield of single phase α iron particles is very small, (less than 5%) in comparison to the yields (greater than 70%) obtained by the protocol that produces both magnetite and α iron.

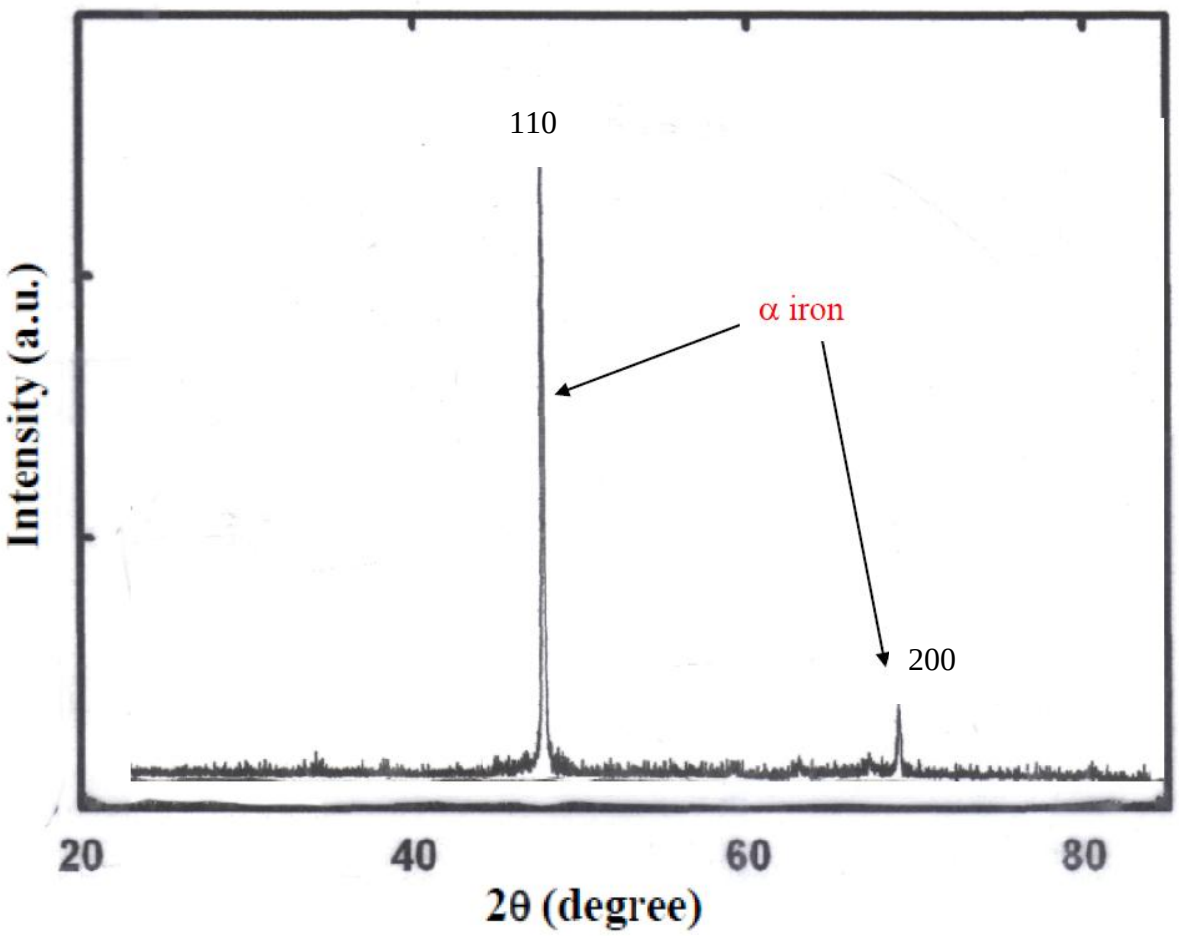

Figure 2.16 XRD pattern for particles produced in a typical experiment involving one gram of iron (II) chloride tetrahydrate added to two grams of previously dissolved sodium hydroxide in a round bottom flask containing 25 mL of ethylene glycol under distillation conditions.

Despite the ease at which a polyol reaction can be carried out, the mechanism of the reaction has been illusive in the literature until recently. It was not until 2000 that a proposed mechanism was put forth to describe the reduction of metals by the polyol process.[159] The first clue of a mechanism was in 1989 when the French chemist Fievet observed that acetaldehyde and diacetyl were observed in the reaction medium as degradation products of the polyol.[160] Therefore, it was predicted that the degradation of ethylene glycol takes place in two steps. The first step is a dehydration of the ethylene glycol producing acetaldehyde:

$$2\ CH_2OH\text{-}CH_2OH \longrightarrow 2\ CH_3CHO + 2H_2O$$

The second step is the duplicative oxidation of the acetaldehyde with the formation of diacetyl. This transformation was found to take place at the same time as the formation of the metallic powder:

$$2CH_3CHO + M(OH)_2 \longrightarrow CH_3COCOCH_3 + 2H_2O + M°$$

(M= Co or Ni)

It was also assumed that the reduction of the metal occurred only with the total oxidation of ethylene glycol into CO_2 and H_2O.[159] This led to the following proposed net reaction:

$$HO\text{-}CH_2\text{-}CH_2\text{-}OH + 5/x\ MO \longrightarrow 5/x\ M° + 2\ CO_2 + H_2O$$

The problem with this assumption, is that the total oxidation of ethylene glycol occurs at the boiling point (197 °C). From the initial research carried out in this work with silver and copper in the beginning of this chapter, it was found that the reduction of both silver and copper could occur below the boiling point of ethylene glycol. For example, the best range of temperatures to reduce silver in ethylene glycol was found to be between 160 °C and 180 °C, and the reduction of copper was also observed to initially take place at 150 °C. Therefore, a more descriptive mechanism was needed to describe the reduction of metals by the polyol method.

A proposed mechanism for the reduction of nickel metal in ethylene glycol has been recently reported that describes the reduction of nickel through a two step process.[161] In this mechanism, the first step involves the ligand exchange forming a nickel glycolate. The reaction then involves the formation of a carbanion by the base. The carbanion is believed to be the source for the two electrons required to reduce the metal. The products of the reaction are zero valent nickel, 2-hydroxyacetaldehyde, and 2-hydroxyethanolate.[161]

With the knowledge of the proposed mechanism for the reduction of nickel, and knowing that magnetite and α iron can be produced during reflux while only α iron is produced during distillation, I propose the following reaction pathway to describe the reduction of iron in ethylene glycol. First, when the reaction is carried out under reflux conditions, there is a ligand exchange with the chloride forming an iron glycolate. Then, as the temperature of the reaction is increased,

water will be produced through the dehydration of the ethylene glycol as discussed previously. This water, which is not removed during the reflux process, undergoes nucleophilic substitution and forms a reactive hydroxide intermediate. This hydroxide intermediate then undergoes disproportionation to produce α Fe and Fe_3O_4 as shown in Figure 2.17.

When the water is removed from the reaction through the use of a distillation column, only α Fe will be produced through the series of steps described in Figure 2.18. First, the chloride is exchanged forming an iron glycolate. The next step involves the removal of hydrogen from a carbon by the base with the formation of water. The electrons from the carbon form a double bond with the oxygen atom, which then moves two electrons onto the metal completing the reduction.

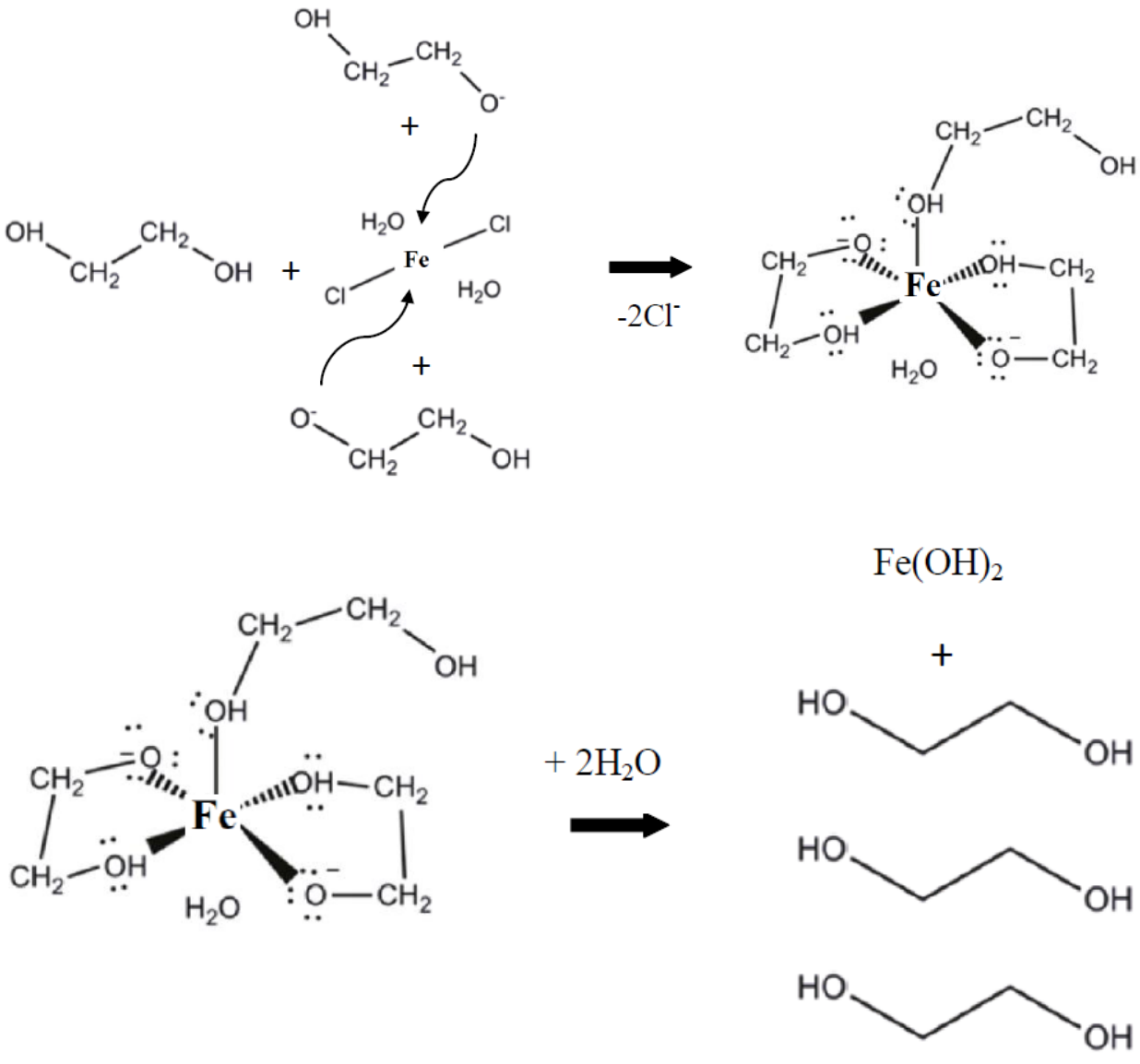

$$4\ Fe(OH)_2 \longrightarrow Fe + Fe_3O_4 + 4\ H_2O$$

Figure 2.17 Proposed mechanism for the reduction of iron under reflux conditions.

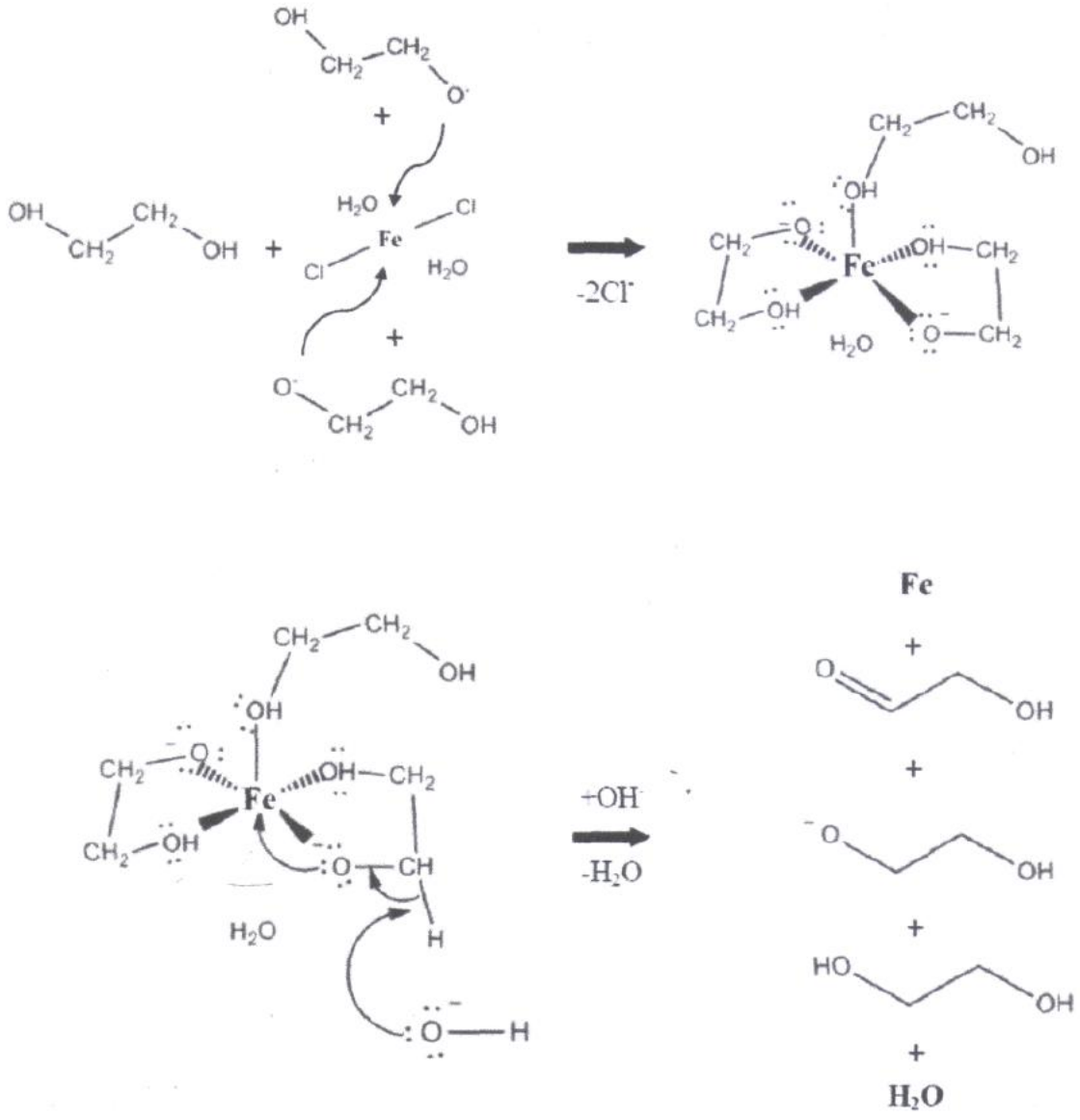

Figure 2.18 Proposed mechanism for the reduction of iron under distillation conditions.

With a demonstrated protocol for the production of monodisperse magnetic iron oxide nanoparticles in hand, the next step in this work was to produce alloyed based iron oxide nanoparticles by a polyol method to include a series of spinel ferrites, MFe_2O_4, where M = Co, Ni, or both Co and Ni. Chapter 3 will take a look at the synthesis and characterization of these magnetically interesting ferrites.

Chapter 3: Cobalt and Nickel Ferrites

3.1 Introduction

Ferrites are defined as a material that is composed of Fe^{3+} ions as the main cation component.[91] There are three main families of ferrites: spinel ferrites, garnet ferrites, and hexaferrites. The main form of iron oxide that is used to make ferrites is magnetite, or Fe_3O_4. Shown below in Table 3.1 are the most common oxides of iron along with their composition.

Table 3.1 The chemical composition of the most common oxides of iron.[91]

Mineral	Chemical Composition
Goethite	α-FeOOH
Lepidocrocite	γ-FeOOH
Akaganéite	β-FeOOH
Schwertmannite	$Fe_{16}O_{16}(OH)_y(SO_4)_z \cdot nH_2O$
	δ-FeOOH
Feroxyhyte	δ'-FeOOH
High pressure	FeOOH
Ferrihydrite	$Fe_5O_8 \cdot 4H_2O$
Bernalite	$Fe(OH)_3$
	$Fe(OH)_2$
Haematite	α-Fe_2O_3
Magnetite	Fe_3O_4
Maghemite	γ-Fe_2O_3
	ϵ-Fe_2O_3
	β-Fe_2O_3
Wüstite	FeO

The spinel ferrite nanoparticles of composition MFe_2O_4 where M is Co or Ni exhibit interesting magnetic properties that are potentially useful for a broad range of biomedical applications, especially in the field of magnetic resonance imaging. Greater stability in a variety of chemical environments, compared to metallic nanoparticles, makes ferrites especially beneficial for biological and medical applications. Changing the identity of M, and by changing the crystallite size of the ferrites can systematically produce nanocrystals with diverse magnetic properties. Once the preparation of the nanoparticles has been optimized, the particles need to be coated with a biocompatible material to prevent aggregation, sedimentation and to provide a scaffold for further functionalization. In this work, spinel ferrites of composition $CoFe_2O_4$, $NiFe_2O_4$, and $Ni_{.5}Co_{.5}Fe_2O_4$ were synthesized by a polyol method utilizing ethylene glycol as the solvent, reducing agent, and surfactant. The nanoparticles produced were surface coated with 3-aminopropyltriethoxysilane to increase solubility as well as to serve as an anchor for further conjugation with targeting substrates such as peptides and antibodies.

3.2 Experimental Section

All chemicals were of reagent grade and used without further purification. Ferric chloride hexahydrate ($FeCl_3 \bullet 6H_2O$ > 97%), ferrous chloride tetrahydrate ($FeCl_2 \bullet 4H_2O$ > 99%), cobalt (II) chloride hexahydrate ($CoCl_2 \bullet 6H_2O$ > 98%), nickel (II) chloride hexahydrate ($NiCl_2 \bullet 6H_2O$ > 98%), sodium carbonate (Na_2CO_3 > 99%), sodium bicarbonate ($NaHCO_3$ >99%), diethylene

glycol 99%, and phosphate buffered saline (PBS 10X Solution), were obtained from Fisher Scientific. 3-aminopropyltriethoxysilane {$NH_2(CH_2)_3Si(OC_2H_5)_3$ 97%} was obtained from TCI America. The alloyed nanoparticles were characterized by XRD in order to determine the phase, purity, crystallinity, and size of the produced particles. All of the samples analyzed in this work were performed on a PANanlytical X'pert pro diffractometer at a scanning step of 0.500^o, in a 2θ range from 20^o to 80^o with monochromatic CuKα radiation (λ = 0.51418 nm). The data was analyzed by the Highscore plus program which contains a diffraction library based on standards provided by the Joint Committee on Powder Diffraction Standards (JCPDS) and the International Center for Diffraction Data (ICDD).[143] Further characterization was performed by using a JEOL JEM-1230 transmission electron microscope (TEM) at 150 kV with a Gatan Ultra Scan 4000 SP 4Kx4K CCD camera. Samples were prepared by dispersing 7 μL of a methanol liquid suspension of particles onto a carbon film supported by carbon mesh (400 grid mesh) followed by the evaporation of the methanol. The magnetic properties of the dried particles were investigated by using a Lakeshore model 7300 vibrating sample magnetometer.

The synthesis of $CoFe_2O_4$ was carried out by making two separate solutions. Solution 1 was prepared by dissolving 2 mmol of $CoCl_2 \cdot 6H_2O$ and 4 mmol of $FeCl_3 \cdot 6H_2O$ into 20 mL of diethylene glycol into a round bottom flask. Solution 2 was prepared by dissolving 16 mmol of NaOH into 20 mL of diethylene glycol. Both solutions were then brought to 80 ^{o}C. Solution 2 was then poured into soulution 1 causing an immediate color change. The mixture was then heated under reflux for either 30 minutes or 1 hour depending on the desired size of nanoparticles. The 30 minute reflux process produced particles that had an average diameter of 20 nm, while

the 1 hour reflux produced particles that had an average diameter of 40 nm. After refluxing, the mixture was quenched by the addition of cold methanol. The mixture was centrifuged, washed in methanol, and then dried in the oven at 100 ^{o}C overnight. The yield of dark brown powder was 478 mg. The synthesis of the $NiFe_2O_4$ was carried out with the same protocol with $NiCl_2 \cdot 6H_2O$ as the starting material. The yield of $NiFe_2O_4$ was 512 mg with an average particle size of 30 nm for the 30 minute reflux, and 50 nm for the 1 hour reflux. In order to prepare the $Ni_{0.5}Co_{0.5}Fe_2O_4$ nanoparticles, the stochiometry of solution 1 was changed to 1 mmol $NiCl_2 \cdot 6H_2O$ and 1 mmol $CoCl_2 \cdot 6H_2O$ dissolved in 20 mL diethylene glycol.

3.3 Schematic of Reaction Sequence

The synthesis of the cobalt and nickel ferrites is accomplished by the following sequence of reactions illustrated in Figure 3.1.

(1) metal ion chelated polyol complex formation;

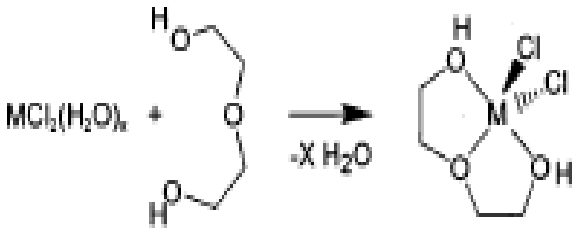

(2) ligand deprotonation with alkoxide formation;

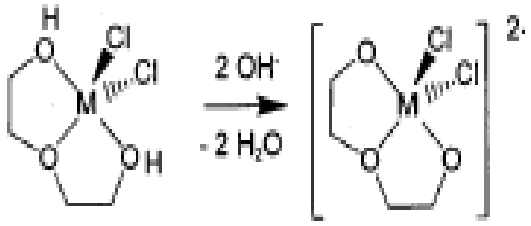

(3) high temperature hydrolysis;

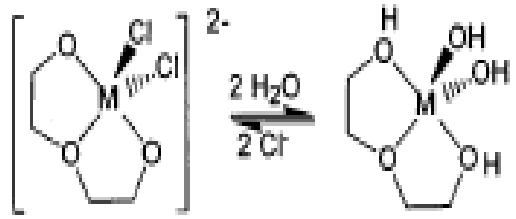

(4) crystal nucleation and growth.

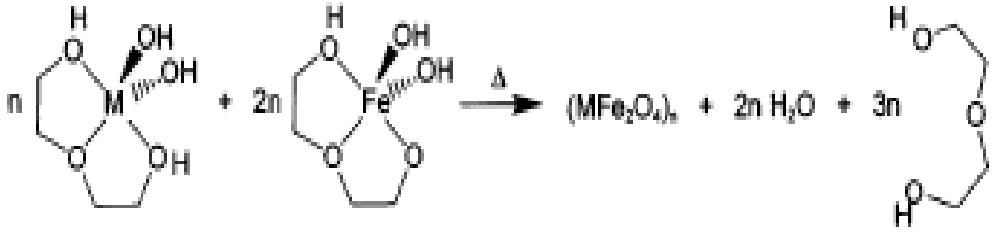

Figure 3.1 Scheme for reaction sequence in diethylene glycol.

Each of these reactions occurs based on previously well determined stochiometry, and therefore produces nanoparticles with a high quantitative yield. The rate of this reaction scheme is highly dependent on the reaction temperature, ranging from nonexistent at room temperature to instantaneous at the boiling point of diethylene glycol (245 ^{o}C). The ability to control the rate of the reaction is particularly useful as it offers control over the nucleation and growth of the nanoparticles. The function of the diethylene glycol is to not only be a solvent and a chelating agent, but also to act as a stabilizing agent. It remains a liquid over a wide range of temperatures (-10 ^{o}C to 245 ^{o}C), it has a high dielectric constant (ε = 32), and the structure of the molecule makes is ideal for forming chelated complexes with metals. Furthermore, many of the first row transition metal chlorides, as well as sodium hydroxide, are soluble in diethylene glycol.

3.4 Functionalization of Nanoparticles

The nanoparticles produced were surface coated with 3-aminopropyltriethoxysilane (APTES) in order to increase the solubility as well as to serve as an anchor for further conjugation with targeting substrates such as peptides and antibodies. The silanization takes place on the particle surfaces bearing hydroxyl groups as depicted in Figure 3.3. In order to surface coat the particles, 100 mg of nanoparticles were dispersed in 50 ml toluene/methanol (1:1 v/v) in a 3 neck round bottom flask equipped with a condenser, thermometer, and nitrogen gas flow. This mixture was heated at 95 $^{\circ}$C until 50 % of the solution evaporated. After evaporation, methanol was adde

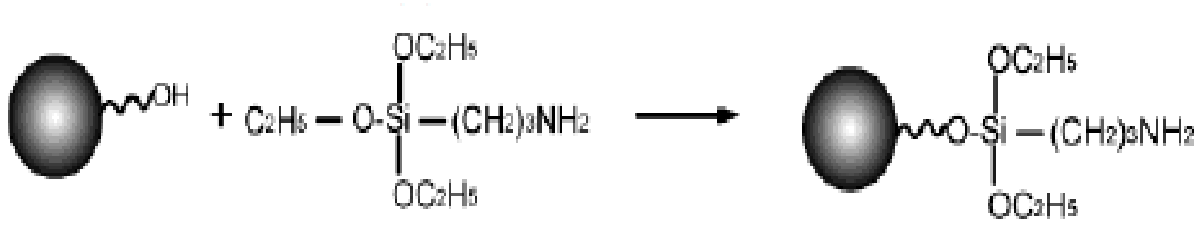

Figure 3.2 Functionalization of iron oxide particles by 3-aminopropyltriethoxy silane (APTES).

in equal volume and the mixture was re-evaporated again to one-half. This process was repeated three times to remove all residual water. Then, 250 μL of a 3 mM 3-aminopropyltriethoxysilane in a 1:1 v/v solution of toluene/methanol was added to the suspension. The silanization was carried out at 110 $^{\circ}$C for 12 hours under rapid stirring. Afterward, the powder was collected by an external magnet, washed several times with methanol, and re-dispersed into 1X phosphate buffered solution.

3.5 Characterization

As illustrated in Figure 3.3 and Figure 3.4, the polyol synthesized and APTES functionalized $CoFe_2O_4$ and $NiFe_2O_4$ nanopaticles are stable in water at a concentration of 450 μg/mL. Also shown in Figure 3.3 and Figure 3.4 are the XRD pattern and TEM image of the as synthesized particles. All of the diffraction peaks for $CoFe_2O_4$ (JCPDS card number 22-1086) and for $NiFe_2O_4$ (JCPDS card number 10-325) are characteristic of the spinel ferrites.[143]

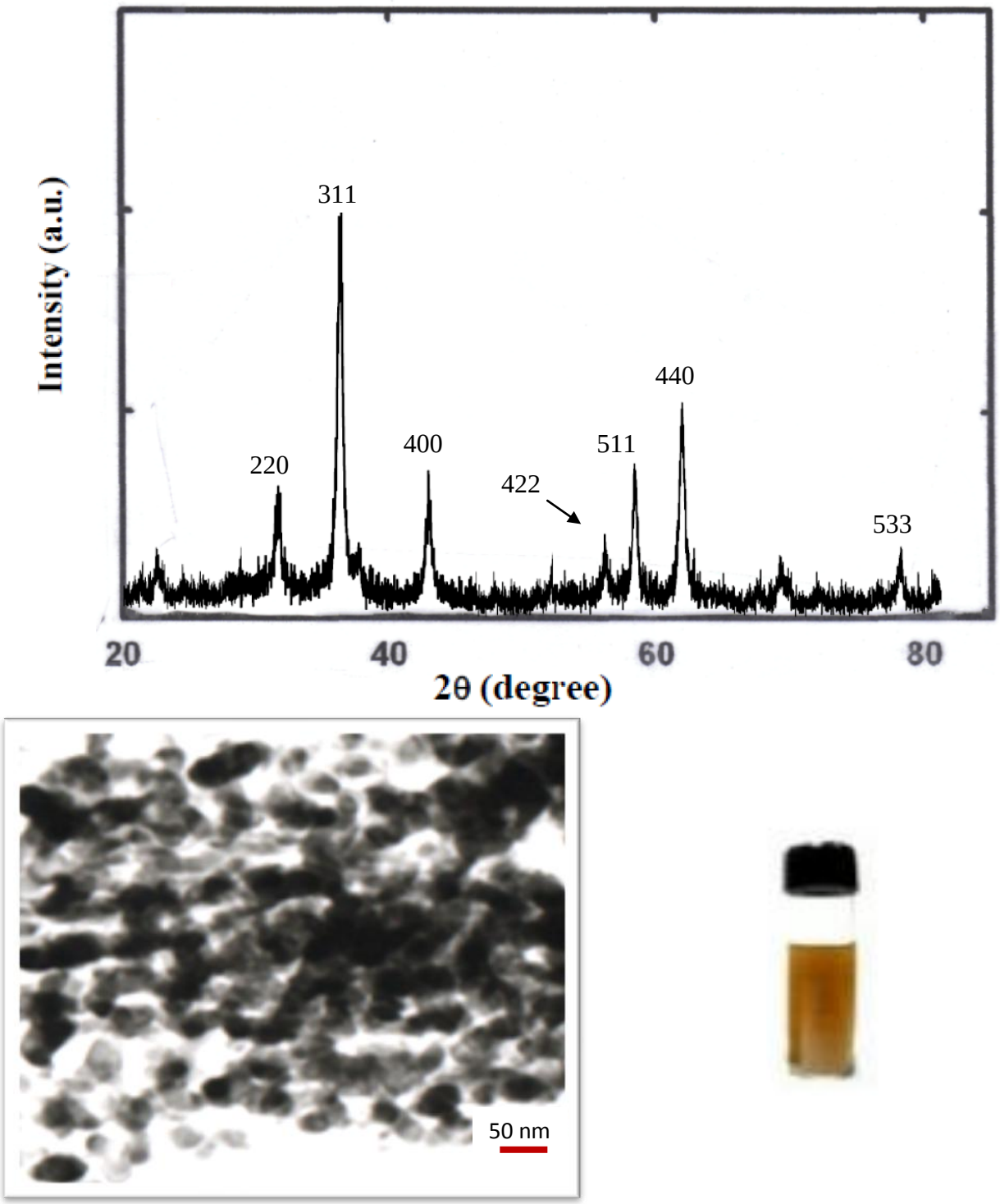

Figure 3.3 XRD pattern of $CoFe_2O_4$ (top), TEM image (lower left), and photograph of 450 μg/mL of $CoFe_2O_4$ in distilled water (lower right).

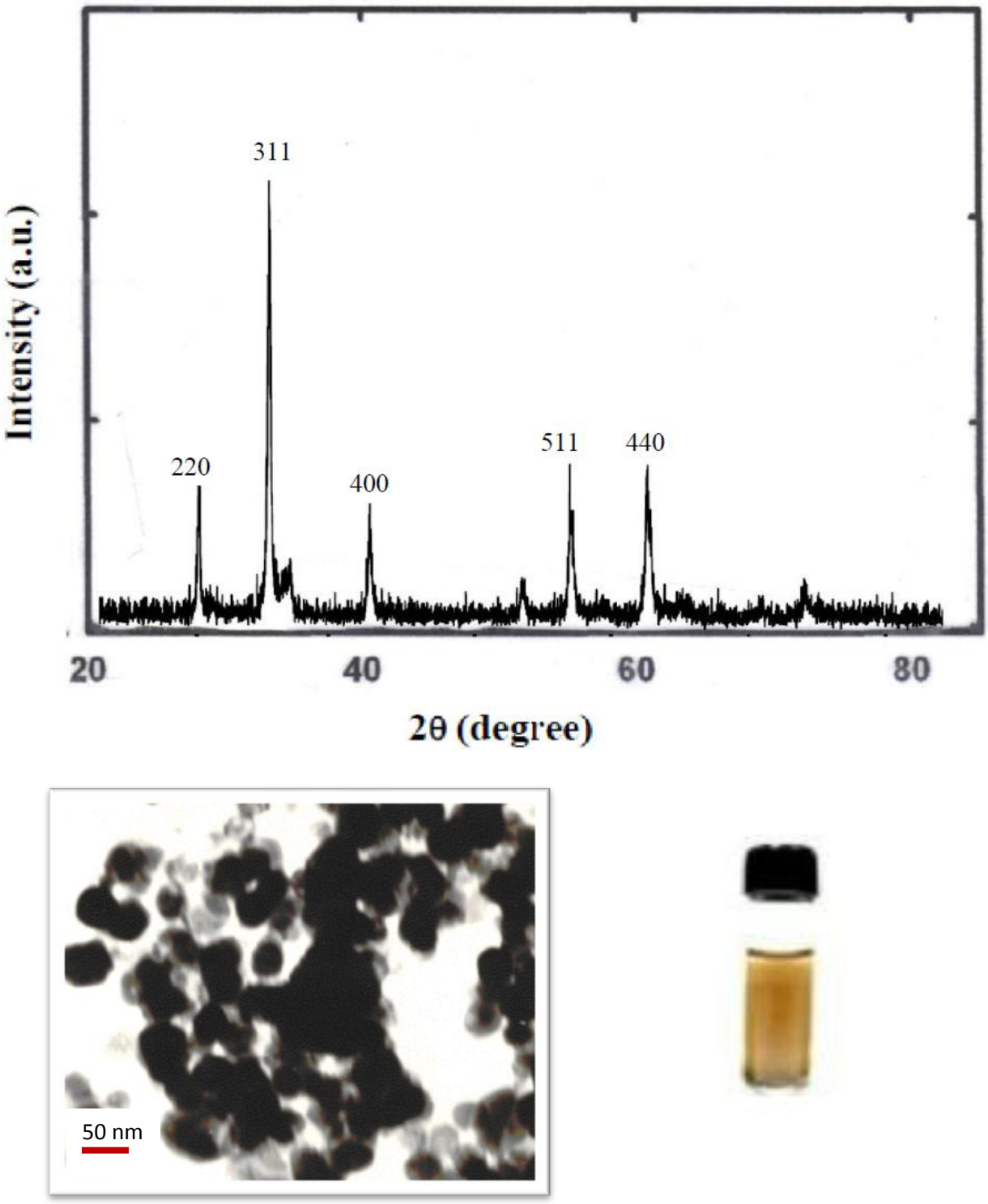

Figure 3.4 XRD pattern of $NiFe_2O_4$ (top), TEM image (lower left), and photograph of 450 μg/mL of $NiFe_2O_4$ in distilled water (lower right).

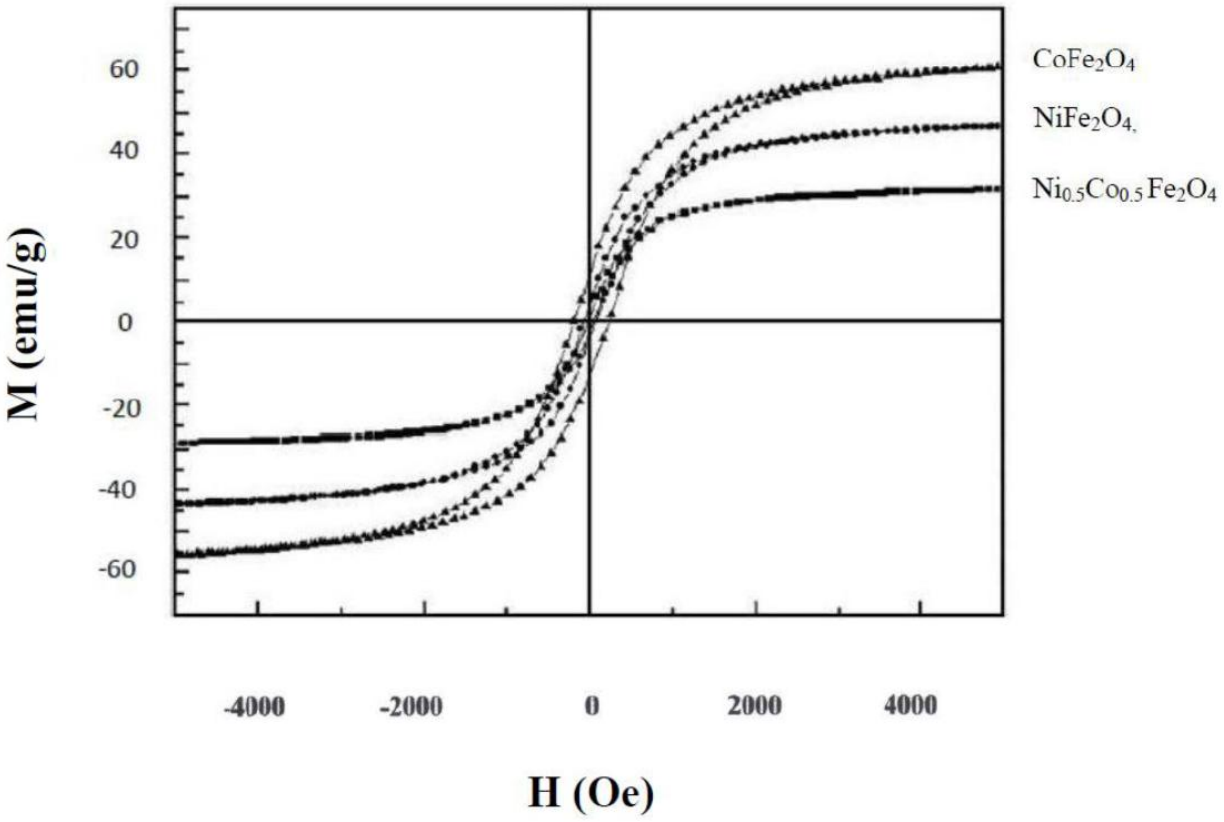

Figure 3.5 The room temperature hysteresis loops of $CoFe_2O_4$, $NiFe_2O_4$, and $Ni_{0.5}Co_{0.5}Fe_2O_4$.

The room temperature hysteresis loops for the nanoparticles are shown in Figure 3.5. The saturated magnetization (Ms) was found to be 56 emu/g for $CoFe_2O_4$, 44 emu/g for $NiFe_2O_4$, and 30 emu/g for the $Ni_{0.5}Co_{0.5}Fe_2O_4$ nanoparticles. The remnant magnetization (M_R) was 19 emu/g, 7 emu/g, and 8 emu/g, respectively. The coercivity was found to be 905 Oe, 70 Oe, and 291 Oe, respectively.

The metal content of the mixed metal ferrites was analyzed by inductively coupled plasma – optical emission spectroscopy (ICP-OES). Inductively coupled plasma – optical emission spectroscopy is a quantitative method utilized to determine trace elements from liquid samples. A typical ICP-OES system will contain basically three components: (1) a source, which is used to generate the high temperature plasma required to atomize and ionize the analyte, (2) a spectrometer capable of separating the emission lines generated by the source, and (3) a detection system that can measure and interpret the emitted light. A schematic of a typical ICP-OES instrument is shown below in Figure 3.6.

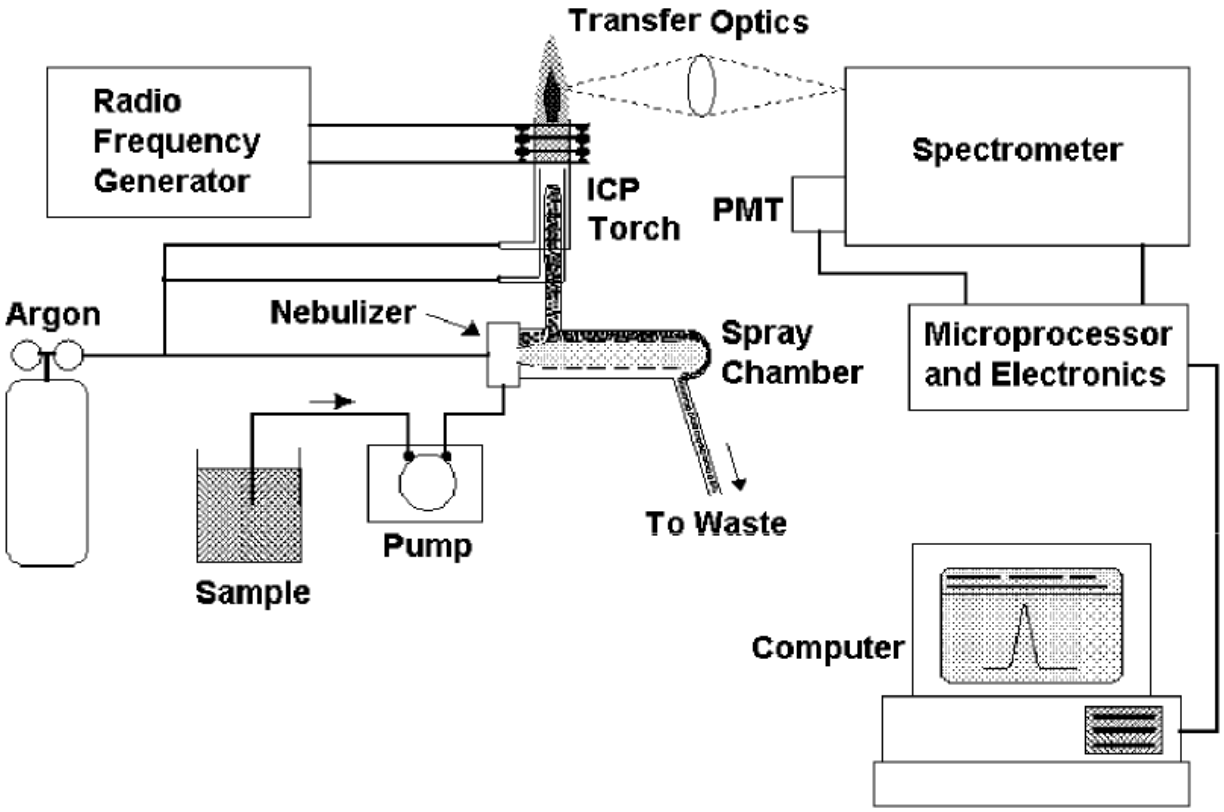

Figure 3.6 Schematic of a typical ICP-OES instrument.[149]

A solid sample for ICP-OES analysis is typically dissolved in an acid digestion bomb at high temperature and pressure. Most samples begin as liquids that are nebulized into aerosol in order to be introduced into the ICP. The sample is then carried into the center of the plasma by argon gas flow. First, the solvent is removed from the analyte. The next steps involve the decomposition of the particles into separate individual molecules that are then dissociated into atoms. Once the sample has been desolvated, vaporized, and atomized, the plasma will then excite one of the atoms electrons to a higher energy level. Figure 3.7 depicts the processes that take place when a sample is introduced into an ICP. As the atoms decay back to their ground

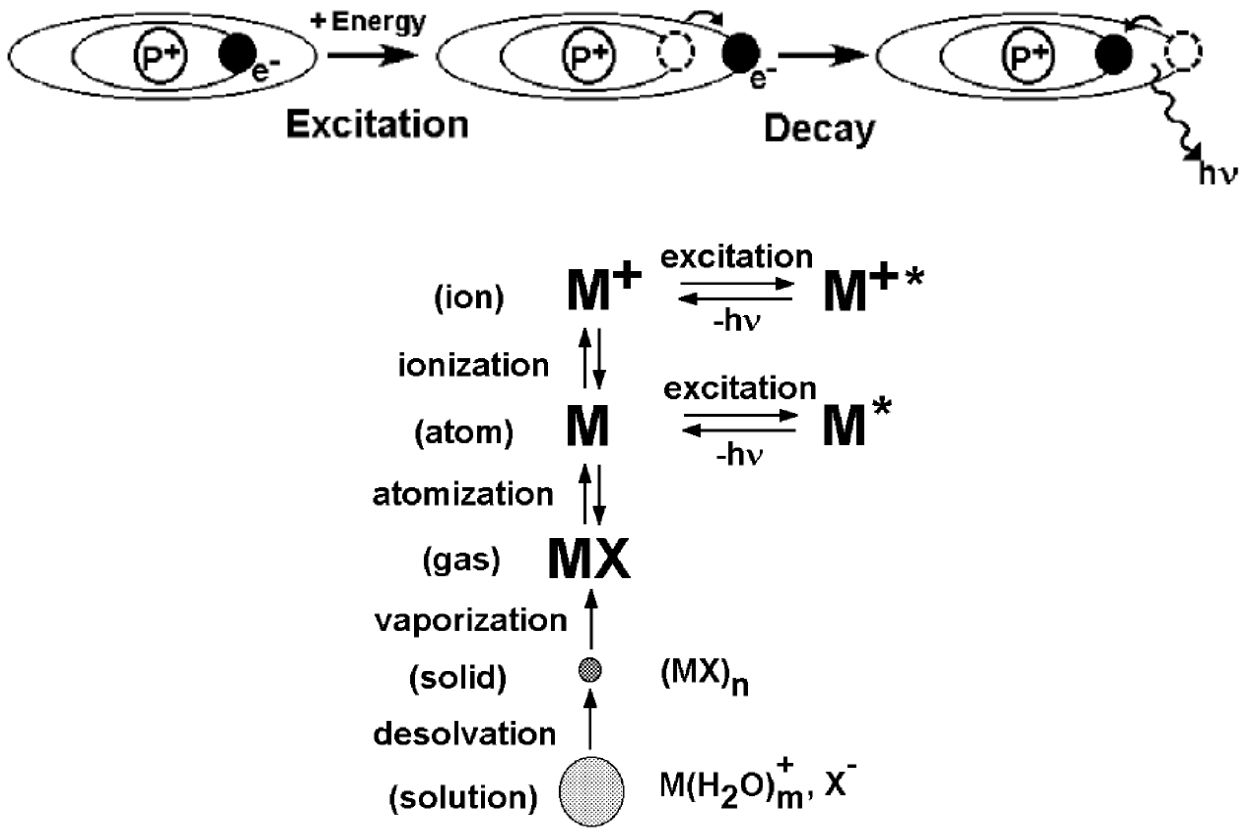

Figure 3.7 Schematic of the processes that take place in the ICP torch.[149]

state, they will emit a wavelength of light that is characteristic of the element. A schematic of the emission of various wavelength of light as atoms decay back to their ground state is shown below in Figure 3.8

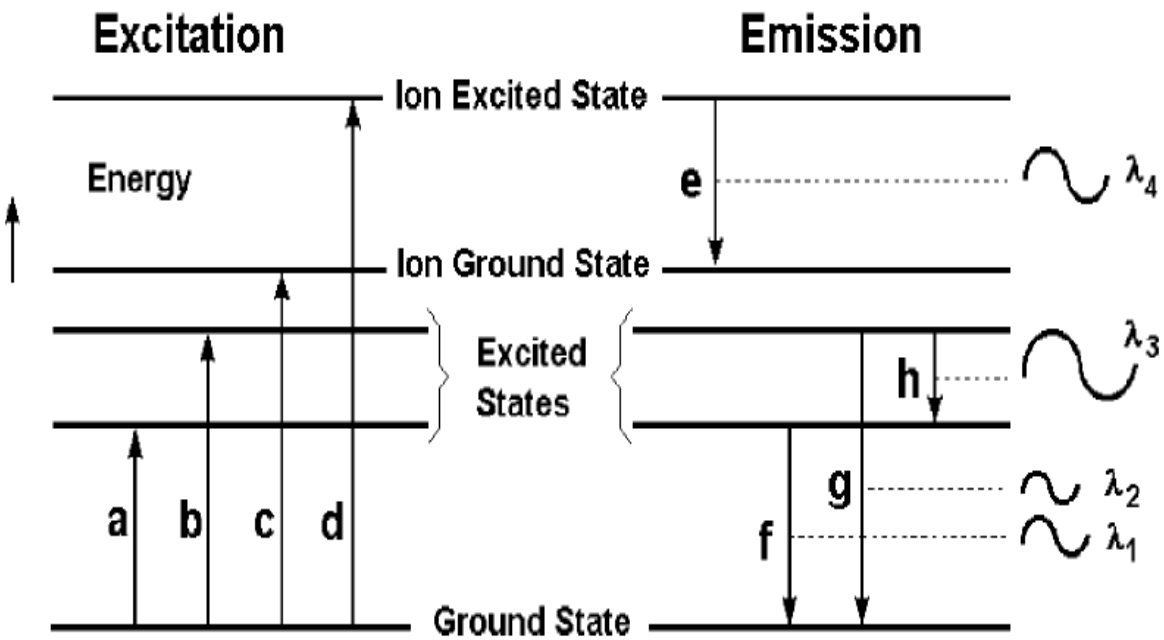

Figure 3.8 Schematic illustrating the excitation and emissions processes of ICP-OES.[149]

Obtaining quantitative information as to how much of an element is in a sample is accomplished by using a plot of emission intensity versus concentration. First, solutions with known concentrations, or standards, that are in the range of the sample concentration, are run through the ICP-OES. These emission intensities can be plotted versus the concentration of the standards to produce a calibration curve. When the emission intensity from the sample is run through the ICP-OES, the intensity can be compared to the calibration curve in order to determine the sample concentration. Figure 3.9 shows a hypothetical calibration curve for an ICP-OES analysis showing how the concentration of a unknown sample can be determined.

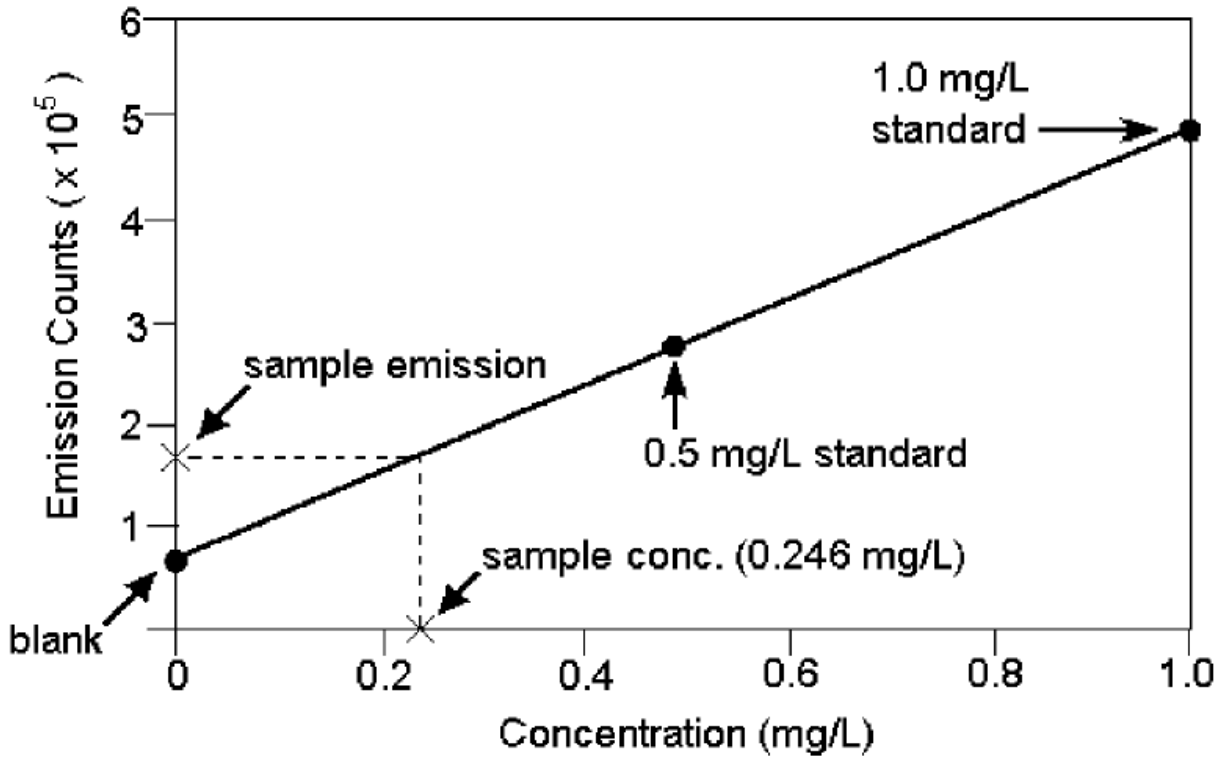

Figure 3.9 A hypothetical calibration curve for an ICP-OES analysis.

The metal content of the mixed metal ferrites was analyzed by inductively coupled plasma – optical emission spectroscopy (ICP-OES). The results are displayed below in Table 3.2. The elemental analysis showed that the ratio of Co/Fe in $CoFe_2O_4$ and the ratio of Ni/Fe in $NiFe_2O_4$ are consistent with that of the initial metal precursors utilized. With a demonstrated procedure for the production of mixed metal ferrites by a polyol process, the next step in this dissertation was to utilize these nanoparticles in the biological applications of cellular separations and magnetic resonance imaging enhancement. Chapter 4 will address cellular separations with ferrites, and Chapter 5 will take a look at the ability of ferrites to efficiently shorten T_2 of water protons in magnetic resonance imaging.

Table 3.2 Elemental analysis by ICP-OES of the mixed metal ferrites produced in ethylene glycol.

Ferrite	Metal Oxide Content (% by wt)	Metals Content (% by wt)	Mole Ratio of Metals Fe:M (M=Co, Ni)
$CoFe_2O_4$	60.7% ± 5.7%	Fe 49.9 % ± 6.2% Co 23.6% ± 5.3%	2.16 ± 8.3%
$NiFe_2O_4$	68.9% ± 4.9%	Fe 48.5% ± 4.6% Ni 25.4% ± 5.4%	1.92 ± 6.2%
$Ni_{0.5}Co_{0.5}Fe_2O_4$	65.2% ± 6.1%	Fe 51.7% ± 5.8% Ni 12.4% ± 4.9% Co 11.5% ± 5.2%	Ni 3.87 ± 4.9% Co 4.23 ± 5.7%

Chapter 4: Cellular Separations with Ferrites

4.1 Introduction

In the last 25 years, there has been a large increase in the emergence of antibiotic-resistant bacteria, causing elevated bacterial pathogenesis. Each year in the United States, an estimated 76 million food borne illnesses cause over 325,000 hospitalizations and 5000 deaths.[136] In 1997, the cost from foodborne illnesses were estimated at $35 billion based on medical expenses and lost productivity.[136] In particular, *Escherichia coli* O157:H7 is one of the most harmful foodborne pathogenic bacteria and alone is responsible for an estimated 73,000 cases of infection and 60 deaths that occur each year.[137] Some of the sources of infection are through the consumption of contaminated beef, lettuce, salami, milk, and various juices. Therefore, developing sensitive and cost effective detection protocols that can rapidly identify pathogenic bacteria is critical for the treatment and prevention of epidemics. The work presented in this chapter presents an immunomagnetic separation for the rapid detection of bacterial targets that requires less preparation time, smaller sample sizes, all with enhanced sensitivity and faster reaction kinetics.

4.2 Synthesis

The synthesis of $FeFe_2O_4$ was carried out by making two separate solutions. Solution 1 was prepared by dissolving 2 mmol of $FeCl_2.4H_2O$ and 4 mmol of $FeCl_3.6H_2O$ into 20 mL of diethylene glycol into a round bottom flask. Solution 2 was prepared by dissolving 16 mmol of NaOH into 20 mL of diethylene glycol. Both solutions were then brought to 80 ^oC. Solution 2 was then poured into solution 1 causing an immediate color change. The mixture was then heated under reflux for either 30 minutes or 1 hour depending on the desired size of nanoparticles. The 30 minute reflux process produced particles that had an average diameter of 20 nm, while

the 1 hour reflux produced particles that had an average diameter of 40 nm. After refluxing, the mixture was quenched by the addition of cold methanol. The mixture was centrifuged, washed in methanol, and then dried in the oven at 100 ^{o}C overnight. The yield of dark brown powder was 506 mg.

4.3 Characterization

The room temperature VSM data for the iron oxide nanoparticles is shown in Figure 4.1. The saturation magnetization of the particles was found to be 76 emu/g with a coercive force of 75 Gauss. The value for bulk magnetite is 130 emu/g. Also shown in Figure 4.1 is the TEM image of the particles showing the particle size distribution with an average particle size of 20 nm. Figure 4.2 shows the XRD plot of the dried particles. The major diffraction peaks for magnetite occur at 30.125^{o}, 35.483^{o} , 43.124^{o}, 53.501^{o}, 57.033^{o}, and 63.231 ^{o} which correspond to the (220), (311), (222), (400), (422), and (511) miller indices respectfully. The peaks were indexed by the International Center for Diffraction Data (ICDD) database for magnetite (fd3m, card#03-065-4899) which is shown in the bottom of Figure 4.2.[143] The average particle size of 20 nm was estimated by using Scherrer's formula, as described previously.

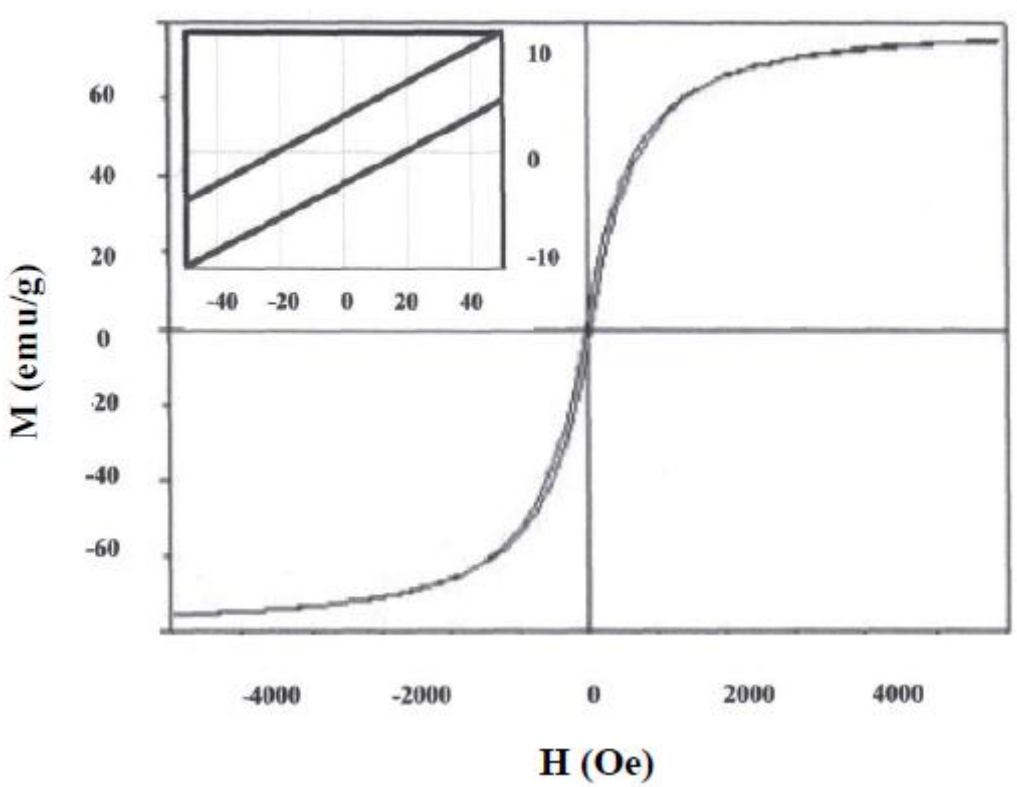

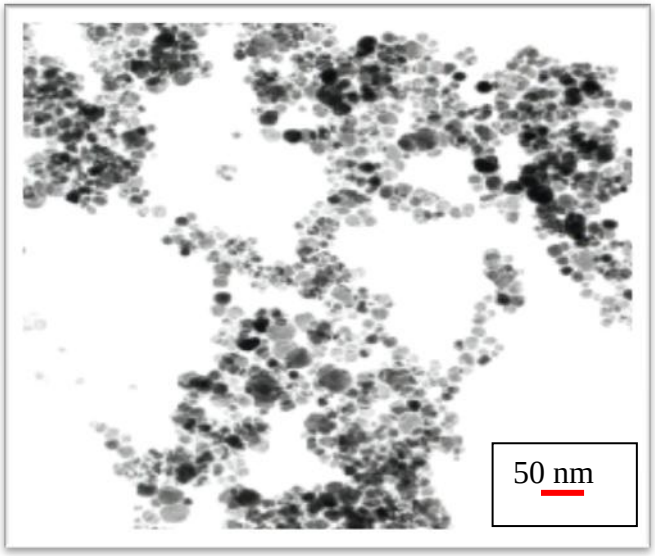

Figure 4.1 Room temperature VSM data of $FeFe_2O_4$ (top) and TEM image of the same particles (bottom).

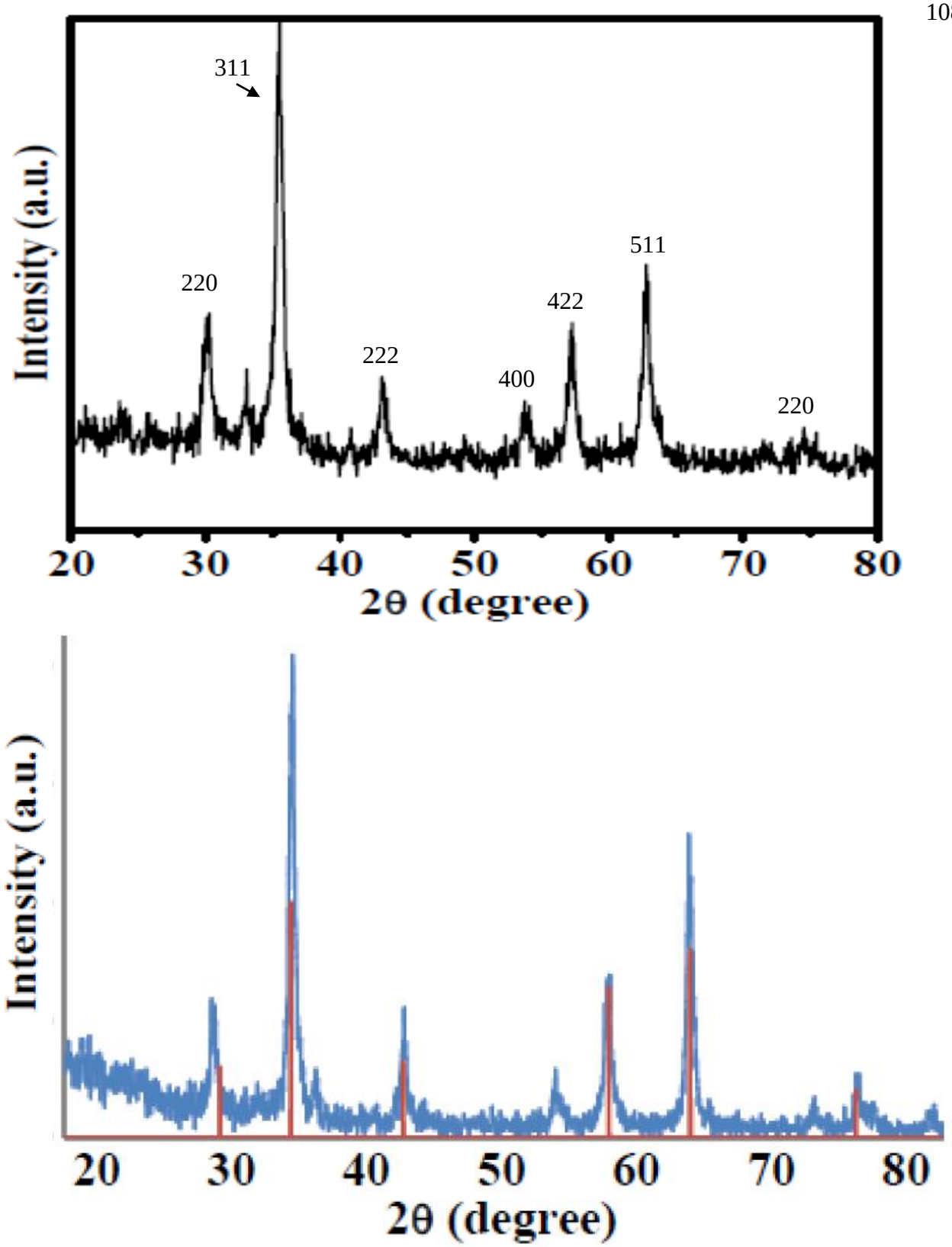

Figure 4.2 XRD pattern of the polyol synthesized $FeFe_2O_4$ (top) and magnetite pattern from the International Center for Diffraction Data (ICDD) database for magnetite (bottom), card # 03-065-4899. http://www.icdd.com/index.htm

4.4 Functionalization

Functionalization was carried out by the introduction of amine groups onto the surface of the nanoparticles by the utilization of 3-aminopropyltriethoxy silane (APTES). The silanization takes place on the particle surfaces bearing hydroxyl groups. As described previously, a typical procedure involved 100 mg of the above prepared iron oxide nanoparticles dispersed into 50 ml toluene/methanol (1:1 v/v) into a 3 neck round bottom flask equipped with a condenser, thermometer and nitrogen gas flow. This mixture was heated at 95 ^{o}C until 50 % of the solution was evaporated. After evaporation, methanol was added in equal volume and the mixture was re-evaporated again to one-half. This process was repeated three times until all residual water was thoroughly removed. Then, 250 μL of a 3 mM 3-aminopropyltriethoxysilane in toluene/methanol (1:1 v/v) was added to the suspension. The silanization was carried out at 110 ^{o}C for 12 hours under rapid stirring. Afterward, the powder was collected by an external magnet, washed several times with methanol, and re-dispersed into 1X phosphate buffered solution. The terminal amine group can now be attached with a bio-molecule of interest by taking advantage of well established chemical cross-linking procedures for proteins as shown in Figure 4.3.

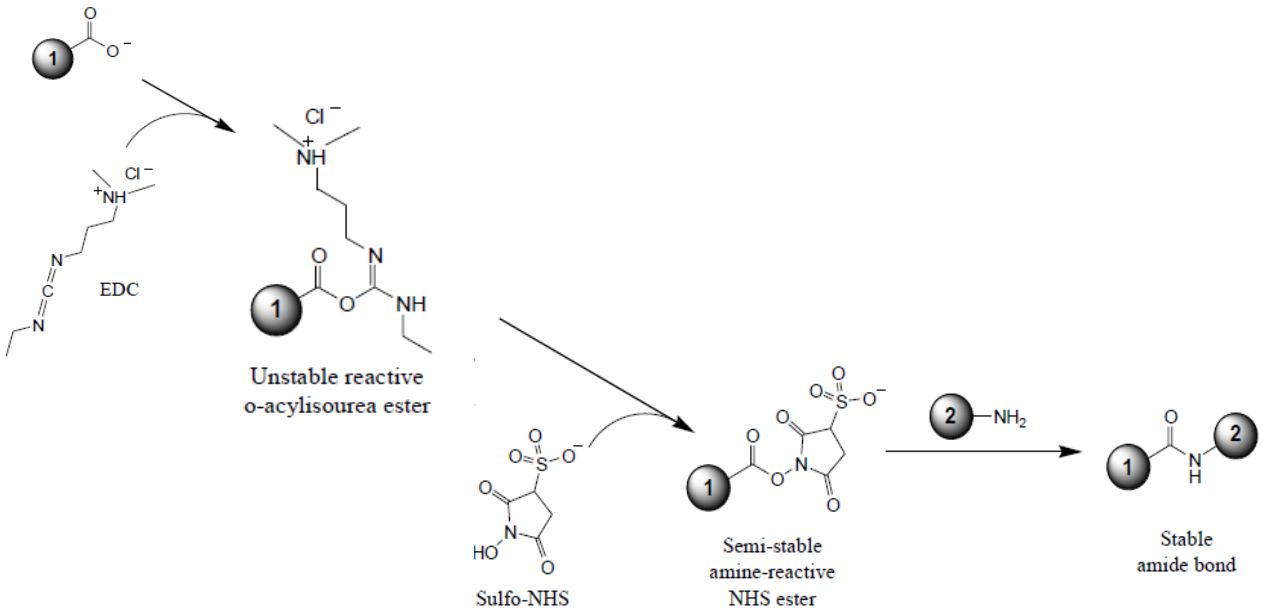

Figure 4.3 Attachment scheme showing the sequence of steps involved in attaching an antibody (1) to the surface of the iron oxide nanoparticles (2).[150]

4.5 Antibody Attachment

To attach the *E. coli* antibody to the iron oxide nanoparticles, five solutions were prepared. These solutions are; 3.0 mg EDC (1-ethyl-3-[3-dimethylaminopropyl] carbodiimide hydrochloride) /ml 1X PBS buffer (8.0 g NaCl, 0.2 g KCl, 1.44 g Na_2HPO_4, 0.24 g KH_2PO_4 in 1.0 liter distilled water), 4.0 mg NHS (N-hydroxysuccinimide) /ml 1X PBS buffer, 3.0 mg nanoparticles /ml 1X PBS buffer, 0.775 mg anti-*E. coli* O157:H7 (obtained from US Biological) /ml 1X PBS buffer, and a 0.177 M carbonate-bicarbonate solution with 1.09 g Na_2CO_3 and 0.63 g $NaHCO_3$ in 100 ml of Milli-Q water. In a 3 ml vial, 130 µL of anti-*E. coli* O157:H7 solution, 90 µl of EDC/1X PBS buffer solution, and 120 µL of NHS/1X PBS buffer solution prepared above were added and mixed thoroughly for 15 minutes at room temperature. After mixing, 400 µL of nanoparticle solution was added. The solution was mixed thoroughly and allowed to react at room temperature for 4 hours. The particles were then separated with a magnet, and the 0.177 M carbonate-bicarbonate buffer (pH = 10) prepared above was added and allowed to react for 15 minutes to quench the reaction. The particles were collected using an external magnet and washed four times with a 0.5% BSA in 1X PBS solution. The beads were re-suspended with a 0.1% BSA in 1X PBS solution and stored at 4 ^{o}C. Figure 4.4 illustrates the attachment of the nanoparticles to the *E. coli* antibody.

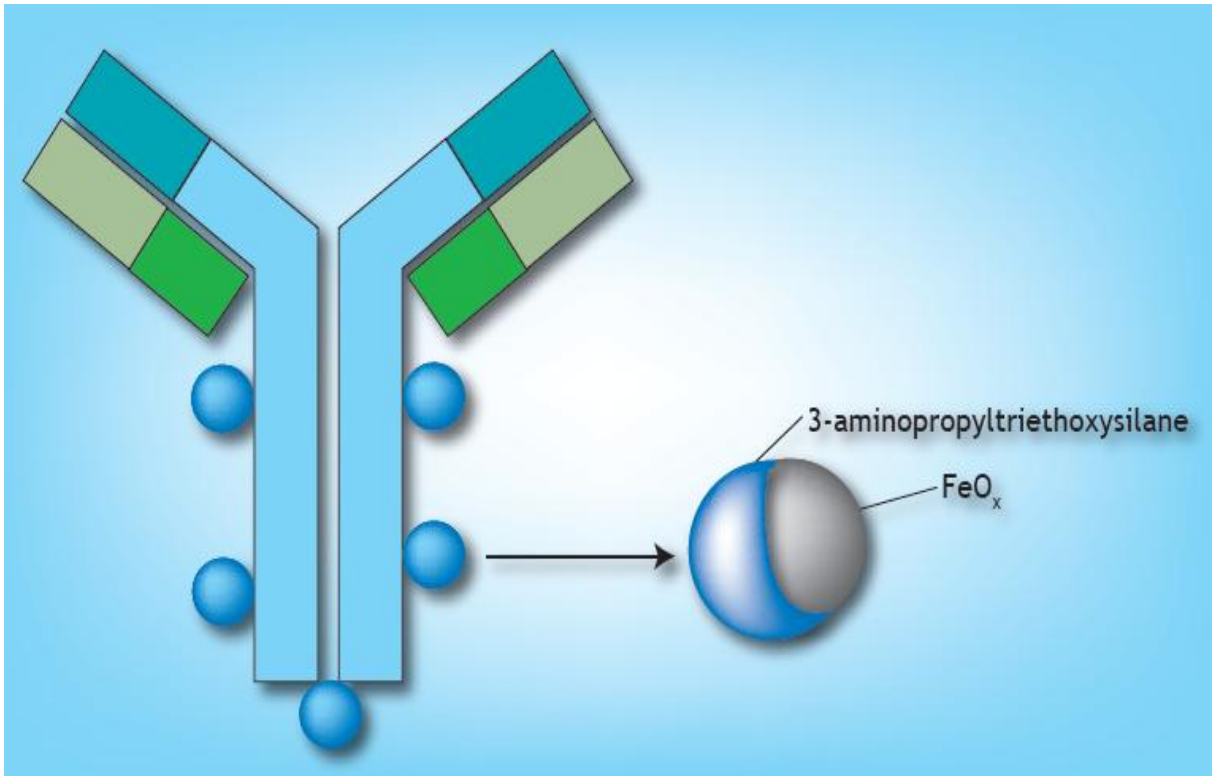

Figure 4.4 Illustration (not to scale) showing iron oxide nanoparticles attached to the *E. coli* antibody.

Antibodies, also referred to as immunoglobulins (Ig), are proteins that are produced by lymphocytes that can selectively bind to a wide variety of antigens. Their presence is essential for the prevention and cure of a multitude of bacterial infections. Antibodies are contained within the gamma fraction of electrophoresed serum and therefore the term gammaglobulin was used.[151] The pattern of serum protein electrophoresis depends on two major types of proteins, the albumin and the globulins.[152] Albumin, which is the major component of serum, is the largest peak that is closest to the positive electrode. The next five components (globulins) are labeled alpha$_1$, alpha$_2$, beta$_1$, beta$_2$, and gamma. The peaks for these components are found closer to the negative electrode, with the gamma peak being closest to the negative electrode.[152] Figure 4.5 shows a typical pattern for the distribution of proteins as determined by serum protein electrophoresis.[151]

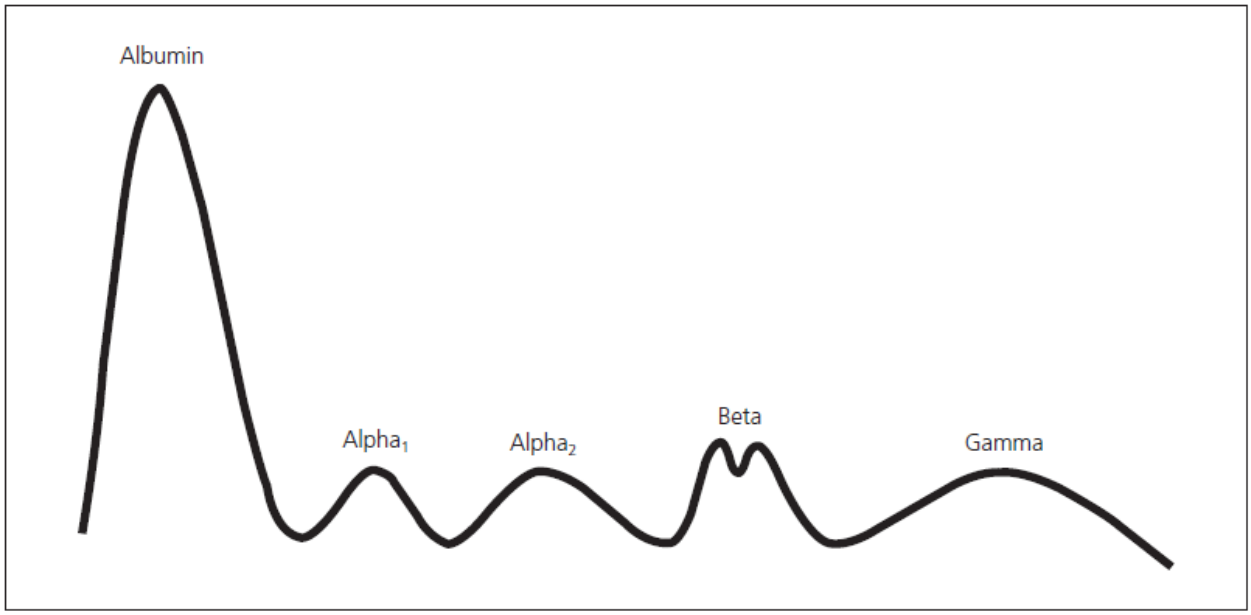

Figure 4.5 Typical pattern for the distribution of proteins as determined by serum protein electrophoresis.[151]

There are a number of immunoglobulins that react specifically with an antigen. Five immunoglobulin classes are described based on their heavy chain composition. They are IgG, IgM, IgA, IgE, and IgD.[153] IgG is the main immunoglobulin found in the serum making up about 75% of the total serum antibodies found in the serum.[152-154] It can move out of the blood stream and into the extravascular space. Its concentration in tissue fluids is greatly increased during inflammation. Furthermore, it is very effective at fighting bacterial toxins, such as the toxins secreted by *E. coli* 0157:H7. [152-154] IgG is the model for studying the structure and function of antibody molecules, and understanding the structure and biochemical properties of IgG is useful to its function in cellular separations by iron oxide nanoparticles. A generalized structure of an immunoglobulin (IgG) is shown in Figure 4.6.

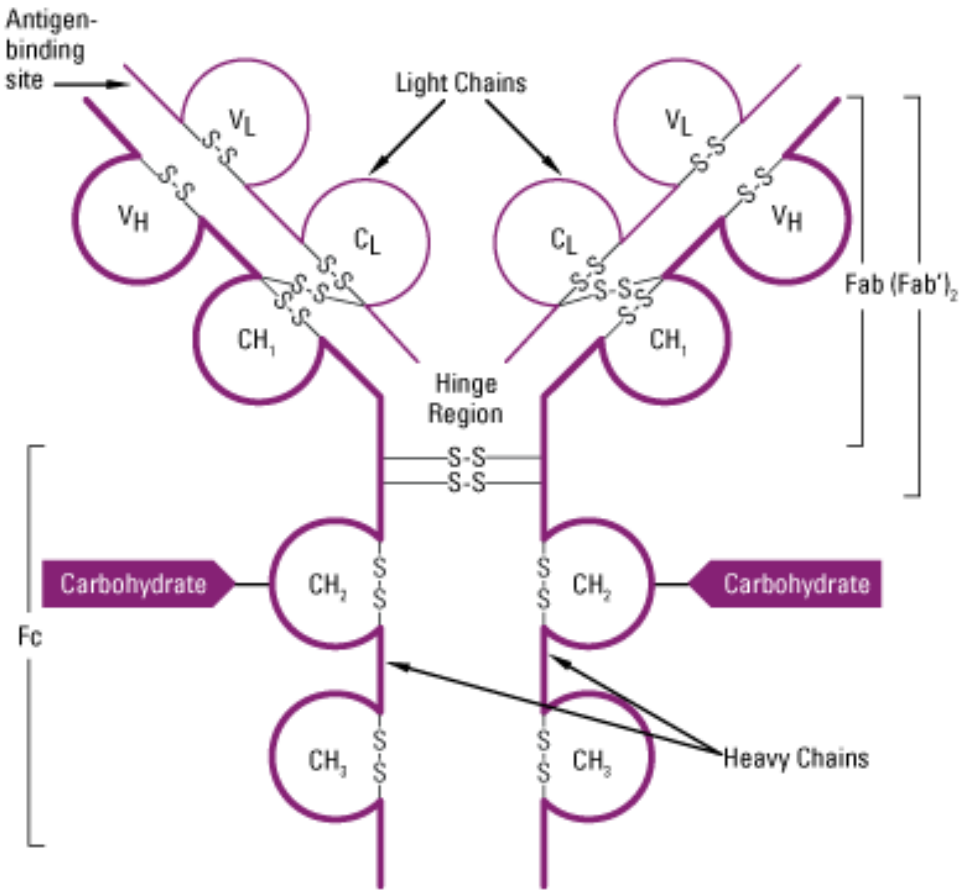

Figure 4.6 A generalized structure of an immunoglobulin (IgG)[152-154]

IgG is a protein with a molecular weight of about 150,000 daltons. It consist of two identical heavy chains, each with a molecular weight of about 50,000 daltons, and two identical light chains, each with a molecular weight of about 25,000 daltons. Each light chain is connected to a heavy chain, and the two heavy chains are connected to each other by disulfide bonds. The IgG molecule is typically drawn to resemble the letter Y with the stem of the Y called the Fc region which consists of the two halves of the identical heavy chains. The top of the Y consists of one complete light chain, and one half of one of the heavy chains. The base of the Y contains the carboxy terminus, and the top of the Y contains the amino terminus of the heavy and light chains. The top of the Y is called the Fab region, and is the location for the antigen binding portion of the antibody. A very specific region of the antigen will react with the antigen binding region of the Fab region of the antibody. Therefore, since the IgG molecule contains two locations for antigen binding, it has the capacity to bind two antigens, and is referred to as being divalent. The polypeptide composition of the Fc region of the IgG antibody is relatively constant; however, the Fab regions will always differ in their amino acid sequence depending on their specificity for a particular antigen. Since the IgG molecule can bind two antigens, it can crosslink antigen molecules, which may promote precipitation, or agglutination of the antigen from its surrounding matrix.

The amount of protein that was bound onto the surface of the nanoparticles was quantitatively determined by the Bradford protein analysis method.[156] The Bradford analysis is a colorimetric protein assay technique in which the bound and free form of the Coomassie® dye absorb at different wavelengths of light as shown in Figure 4.7. The bound form of the dye has an absorption maximum at 595 nm (blue), and the unbound forms have absorption maxima at either 650 nm (green), or 470 nm (red) depending on the pH of the solution.[156] At a pH of around zero, all three nitrogens will be positively charged and the dye will be a cation with an overall charge of +1. The cation form of the dye will appear red. At a pH of around 1, the dye will not have an overall charge and will be in the green form. At a pH of 2 up to 7, only one nitrogen will carry a positive charge, and the dye will have an overall charge of -1. The anion form of the dye will appear blue. At a pH greater than 7, the final proton will be lost, and the dye will appear pink. The pink form does not play a key role in biochemical analysis.

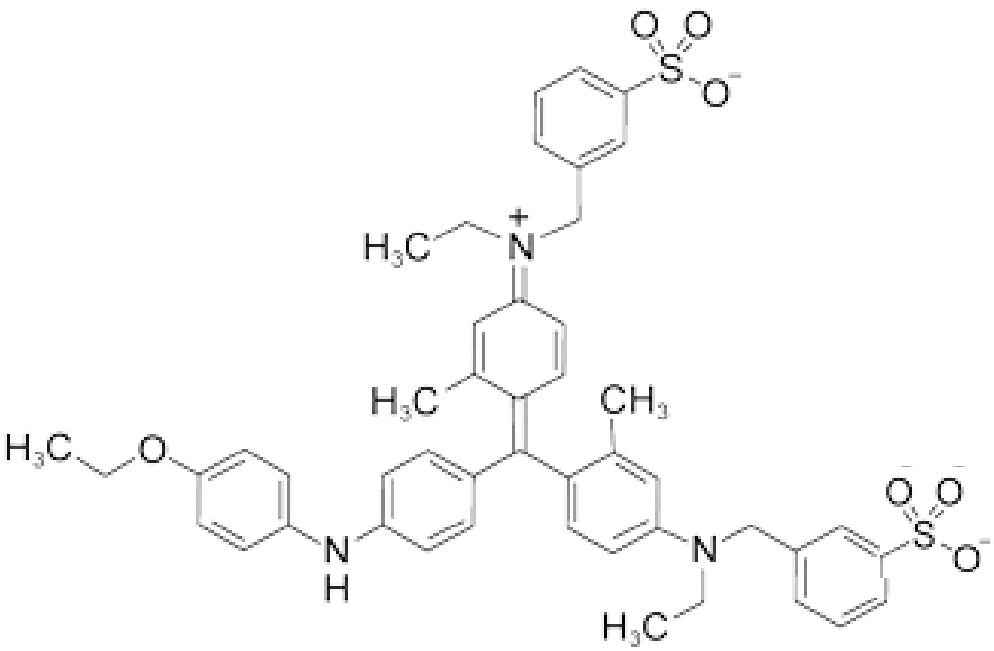

ANION $\underset{H^+}{\overset{OH^-}{\rightleftharpoons}}$ NEUTRAL SPECIES $\underset{H^+}{\overset{OH^-}{\rightleftharpoons}}$ CATION.

595 nm (blue) 650 nm (green) 470 nm (red)

Figure 4.7 The structure of the Coomassie® dye reagent (top), and the various colors formed depending on the charge of the dye (bottom).[156]

The Coomassie® blue reagent was prepared by dissolving 100 mg of the reagent in 50 mL of 95% ethanol. To this solution, 100 mL of 85% phosphoric acid was added. The resulting solution was diluted to 1 L with deionized water. This dilute reagent may be used for up to two weeks when kept at room temperature. A series of ten standards containing the protein anti-*E.coli* O157:H7 were prepared in PBS buffer in a volume up to 0.1 mL in the concentration range of 10 µg/mL to 100 µg/mL. To this solution, 5.0 ml of the previously prepared Coomassie® blue reagent was added, and the resulting solution was vortexed. The absorbance was then measured

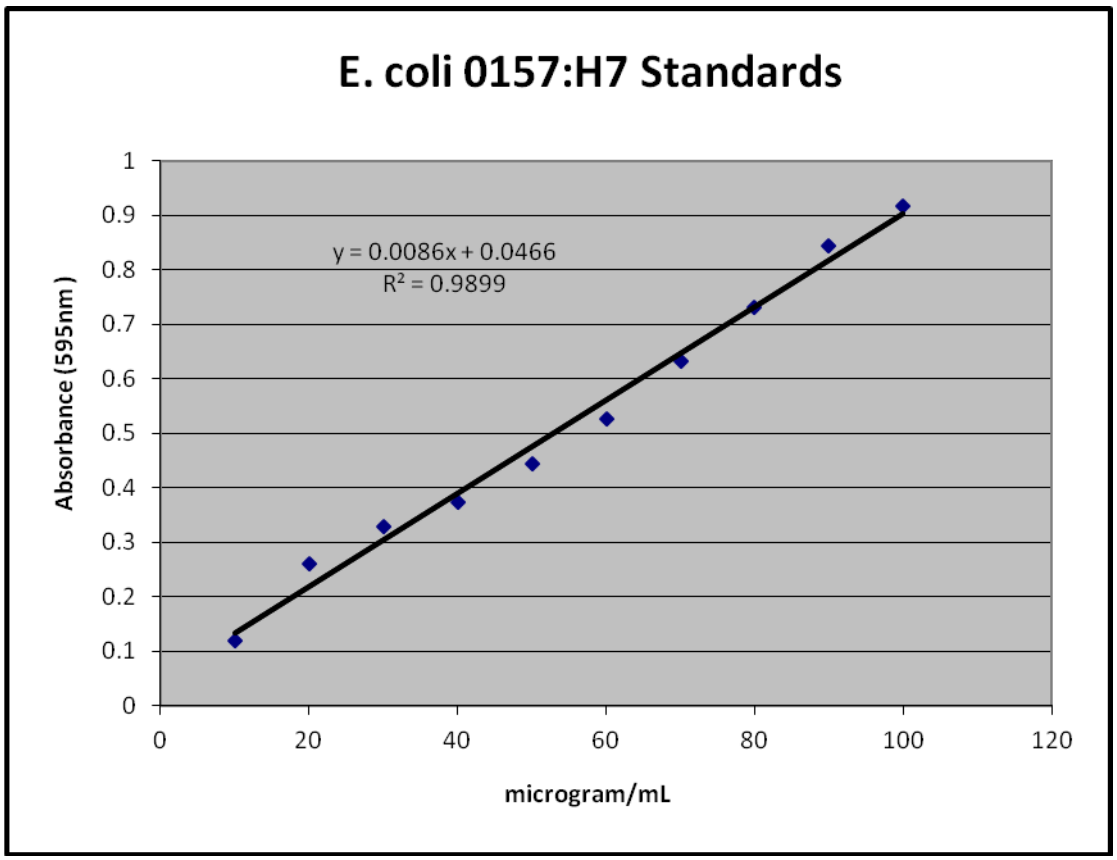

Figure 4.8 Standard calibration curve for the protein anti-*E.coli* O157:H7 analyzed by the Bradford protein analysis.

at 595 nm compared to a reagent blank which contained 0.1 mL of buffer and 5.0 mL of Coomassie® blue reagent. The increase in absorption at 595 nm is proportional to the protein bound dye and therefore to the amount of protein in the sample. The results for the standards are shown in Figure 4.8.

The Bradford method is a simple and accurate procedure used for determining the concentration of proteins in solution. It involves the addition of the acidic dye Coomassie® blue to a protein solution. During the formation of the dye-protein complex, the hydrophobic pockets of the protein will interact by van der Waal forces with the hydrophobic regions of the dye. This interaction positions the positive charge of the amine groups in the protein within close proximity to the negative charge of the dye. The interaction is stabilized through ionic interactions between the two, and it is this stabilization of the blue anion form of the dye by the protein that will allow quantitative estimation of the amount of protein in solution. The Coomassie® dye binds to predominately basic amino acids, especially arginine, as a result of this ionic stabilization.[156] Figure 4.9 illustrates the structure of the basic amino acids of lysine, arginine and histidine. Also shown in Figure 4.9 are the resonance structures of the basic amino acid arginine, which is predicted to play a major role in the binding to the Coomassie® dye.

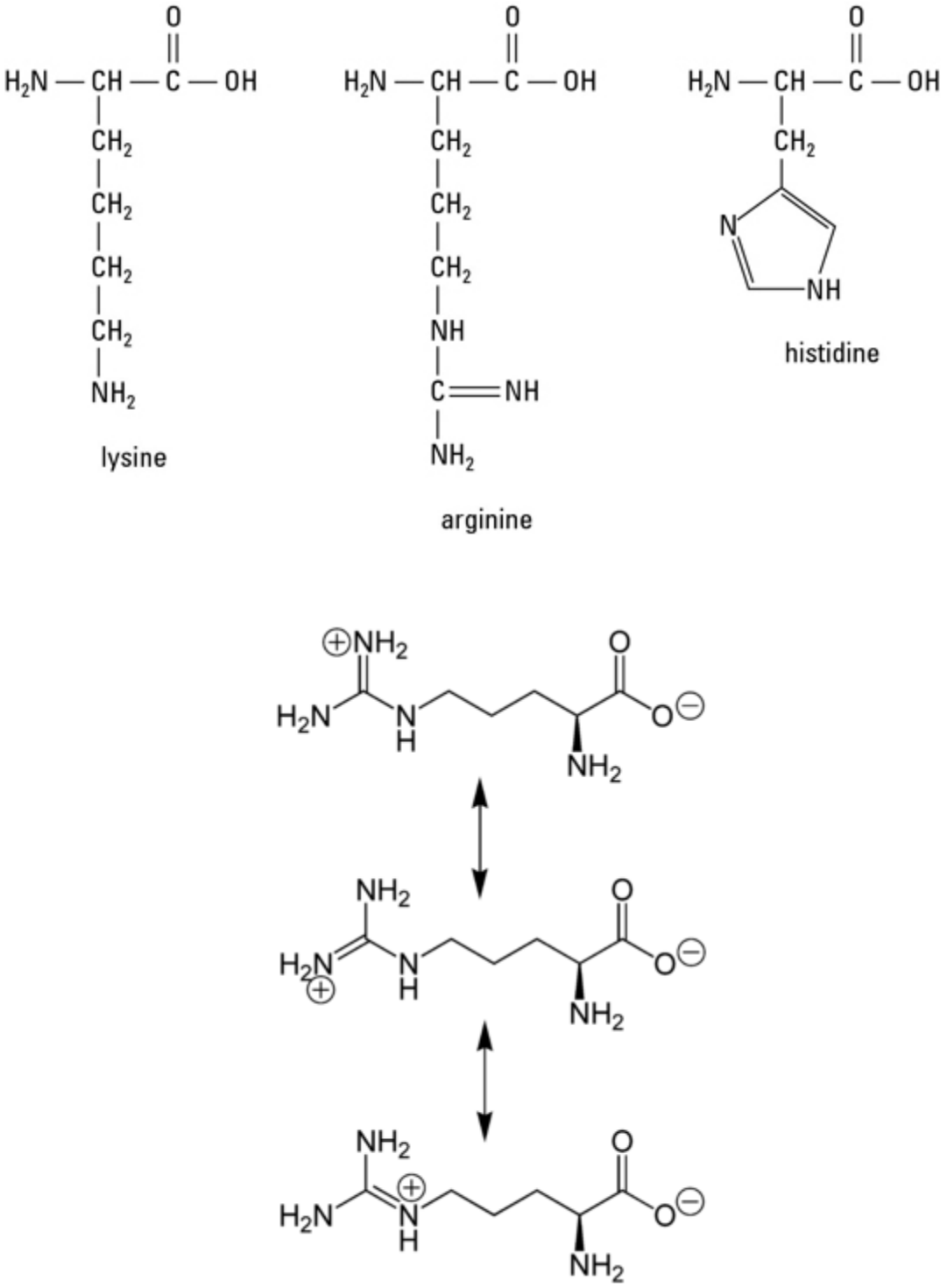

Figure 4.9 The structure of the basic amino acids of lysine, arginine, and histidine (top) and the resonance structures of arginine (bottom).

By using the Bradford method, the iron oxide nanoparticles were found to bind approximately 96 ± 11.3% µg of the protein anti-*E.coli* O157:H7 when reacted with 1.2 mg of particles. The unoccupied sites on the nanoparticles were then blocked by washing the particles in a 0.5 % bovine serum albumin in phosphate buffered saline solution. It is very important to block the unoccupied sites on the surface of the particles in order to reduce the amount on nonspecific binding of proteins. A variety of blocking buffers, such as nonfat milk to very pure proteins have been used to block un-reacted sites. The proper choice of blocker for a giving protocol will depend on the antigen and of the antibody to be used. The best blocking agent will bind to all sites of nonspecific interaction without changing the active site for antigen binding. Using inadequate or excessive amounts of blocker may greatly alter the antigen-antibody interaction. The blocker used for blocking the unoccupied sites on the nanoparticles was a wash in 0.5% BSA in phosphate buffered saline followed by storage in a 0.1% BSA solution. With particles activated with the anti *E. coli* 0157:H7, the next step was to evaluate their effectiveness in extracting *E. coli* 0157:H7 from various biological media.

4.6 Extraction of *E. coli* O157:H7

The extraction of *E. coli* O157:H7 was accomplished by mixing 20 µl of modified iron oxide nanoparticles with 1 ml of sample. Samples were vortex mixed for 30 seconds to ensure good distribution of the iron oxide nanoparticles in the sample, and then gently mixed for 30 minutes. An external magnet of 3500 Gauss was used to sequester the iron oxide nanoparticles on the side of the sample tube. The sample liquid was removed by pipette, leaving the iron oxide nanoparticles bound to the bacteria behind. The nanoparticles were washed with 1 ml of PBS buffer three times and suspended in 100 µl of PBS buffer. Fifty microliters of this final suspension was transferred to a growth plate, containing differential agar, and streaked for isolation. The differential agar was used to distinguish the *E. coli* O157:H7 from other species of *E. coli*. Plates were incubated for 18 to 24 hours at 37ºC. *E .coli* O157:H7 species appeared pink on the differential agar, while non O157:H7 species appeared blue or gray. Using growth media spiked with 1:1000 *E. coli* O157:H7 to non *E. coli* O157:H7, iron oxide nanoparticles were compared to commercial particles for capture efficiency. Counting colonies extracted using iron oxide nanoparticles yielded an estimated 2000 colonies, while current commercial beads yielded an estimated 1800 colonies as shown in Figure 4.10.

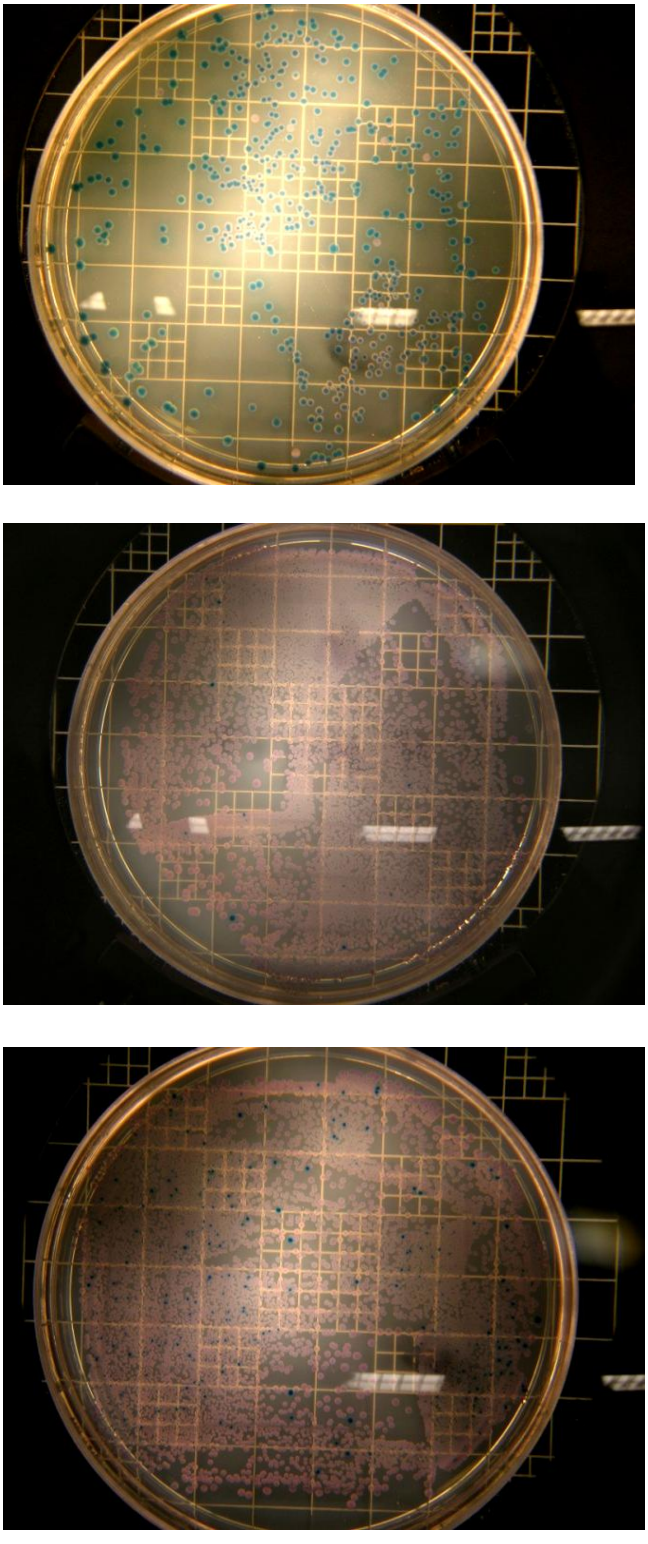

Figure 4.10 Photograph of non-*E.coli* O157:H7 (top). Photograph of iron oxide particles showing capture efficiency. Counting colonies using nanoparticles yielded an estimated 2000 colonies (middle). Photograph of commercial beads showing capture efficiency. Counting colonies using commercial beads yielded an estimated 1800 colonies (bottom).

Detection of *E. coli* O157:H7 was also performed by Matrix Assisted Laser Desorption Ionization Time of Flight/Mass Spectrometry (MALDI-TOF/MS). Once the *E. coli* O157:H7 was extracted; it was washed three times with 500 µl of sterile water. The iron oxide nanoparticles with bacteria attached, were re-suspended in 150 µl of 50:50 acetonitrile/water (0.1% TFA). This solution was vortex mixed for 1 minute, and spotted onto a MALDI target plate in a 1:1 ratio with sinapinic acid and allowed to dry prior to mass spectrometry. Mass spectra obtained from cultures show biomarkers for *E. coli* O157:H7 and non-O157:H7. The mass/charge peak at 9747 is the most important biomarker, and is found only in *E. coli* O157:H7, whereas the peaks at 8321, 7269, and 9944 are biomarkers found in non-O157:H7 species. Comparison of *E. coli* O157:H7 mass spectra obtained with iron oxide nanoparticles to spectra of *E. coli* O157:H7 obtained with commercial beads is shown in Figure 4.11 with biomarkers ions denoted.

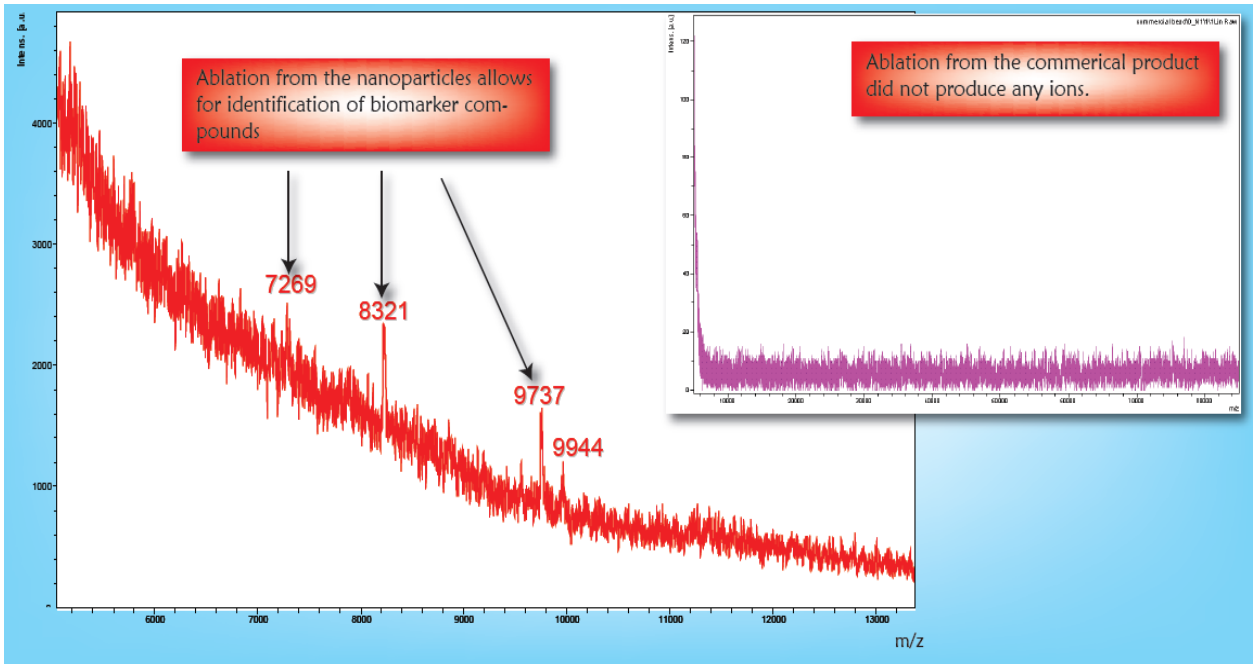

Figure 4.11 Mass spectra of nanoparticles (left) compared to commercial beads (right).

The iron oxide nanoparticles provided a much cleaner spectrum. The noisy mass spectra resulting from the commercial product is likely attributed to the polystyrene coating as shown in Figure 4.12.

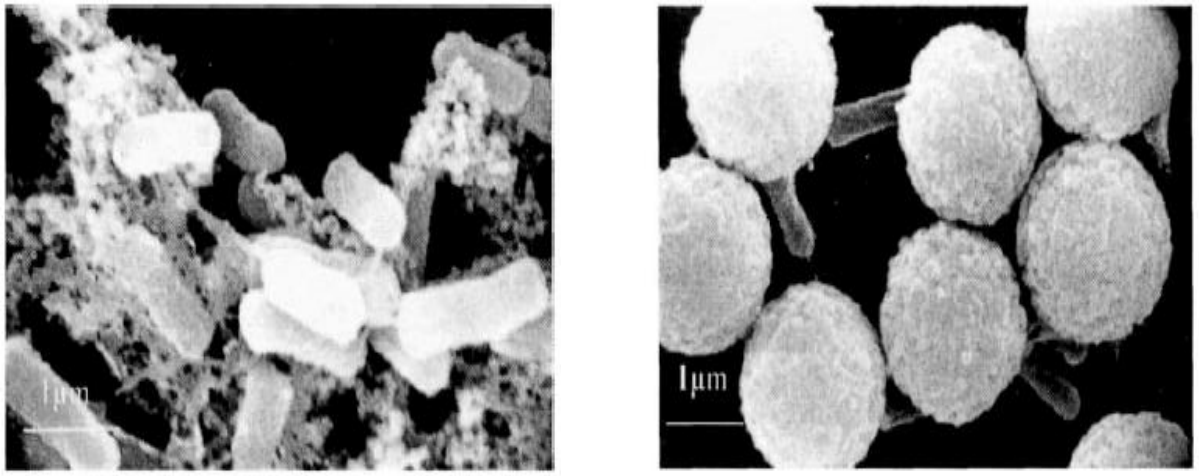

Figure 4.12 SEM image of nanoparticles (left) and commercial beads (right) attached to *E. coli* O157:H7.

4.7 Commercial Beads Characterization

Table 4.2 Magnetic properties of commercially prepared beads (MyOne Dynabeads® anti-E coli O157 Dynal Biotech)

Dynabeads product	Diam. (µm)	Magnetic Susceptibility[1] (dry substance)		Saturation Magnetisation[2] (kA/m)		Iron content (%, w/w dry substance)
		m^3/kg (mass)	Dimensionless (volume)	$A \cdot m^2/kg$ (mass)	kA/m (volume)	
MyOne Dynabeads	1.0	$8 \cdot 10^{-4}$	1.4	24	43	26
M-270 Dynabeads	2.8	$6 \cdot 10^{-4}$	1.0	13	20	14
M-280 Dynabeads	2.8	$5 \cdot 10^{-4}$	0.7	10	14	12
M-450 Dynabeads	4.5	$10 \cdot 10^{-4}$	1.6	19	30	20

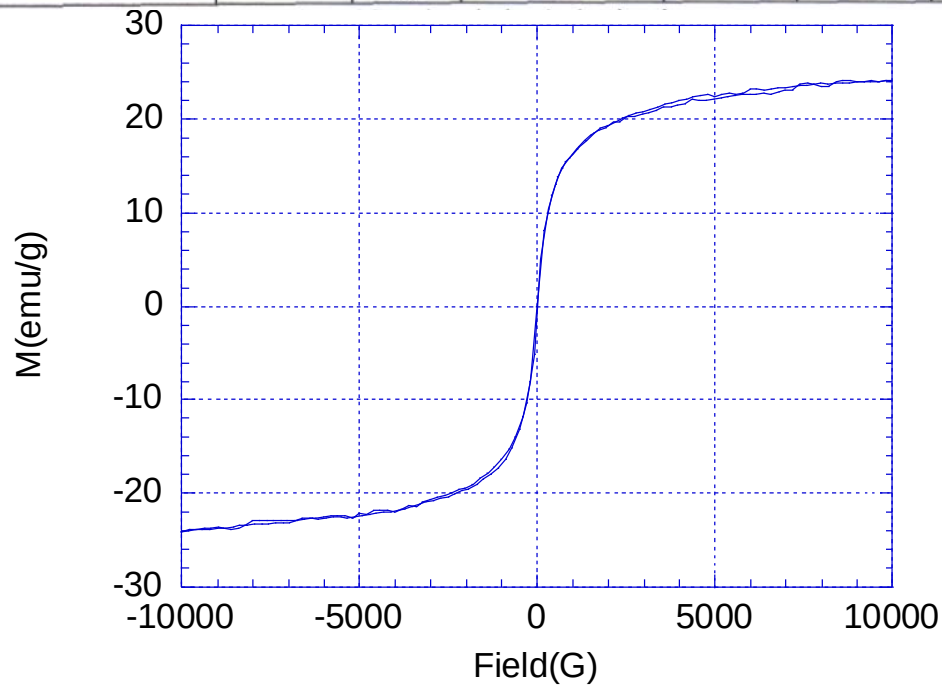

Figure 4.13 Room temperature VSM data of the commercial beads plotted as magnetization (emu/g) versus applied field (G). (MyOne Dynabeads® anti-E coli O157 Dynal Biotech)

4.8 Conclusions

Commercial beads currently used in *E. coli* O157:H7 separations typically have a size range of 1 micrometer with a calculated surface area between 10 – 16 m^2/g as shown in Table 4.2 and a saturation magnetization of 24 emu/g as shown in Figure 4.13. This compares to nanoparticles which are 20 nanometer in size with a calculated surface area between 50 – 60 m^2/g and a saturation magnetization of 76 emu/g. Nanoparticles with their reduced sized and greater magnetic moment provide greater sensitivity based on design alone. The reduced size of the nanoparticle will allow for better mixing in a variety of food matrices and the increased magnetic moment would allow for quicker and more uniform extractions, especially in viscous food matrices. Nanoparticle extraction followed by mass spectrometry could provide a valuable and rapid analytical tool for the determination of pathogenic bacteria that is not presently possible by commercially prepared beads.

Chapter 5: Applications of Ferrites in MRI

5.1 Introduction

One current challenge in the biomedical arena is the sensitive imaging of biological targets by noninvasive processes. Currently, processes such as fluorescence, ultrasound, positron emission tomography (PET) and magnetic resonance imaging (MRI) are being increasingly developed to meet these challenges. Unfortunately, in many cases, the resulting images are of poor quality to provide adequate detailed biological information. Therefore, the success of many imaging modalities is greatly dependent on imaging agents which make it possible to not only detect diseases, but also to localize and monitor therapeutic agents *in vivo*. The successful development of imaging probes is a challenging task; however, because of their small size and multifunctional ability, nanoparticles are now emerging as excellent, ultra sensitive imaging agents.

Imaging of soft tissue has become the domain of MRI due to its superiority over other imaging techniques. The fundamental principle of MRI is that the unpaired nuclear spins of hydrogen from water align themselves when exposed to an external magnetic field. MRI depends on the counterbalance between the very small magnetic moment on a proton, and the extremely large number of protons found in biological tissues. Since most biological tissues range in water content from 70% to 90% water, and since there are 6.6×10^{19} protons in every mm^3 of water, an effective signal can therefore be observed.[139] Protons from different tissues react differently depending on their surrounding chemical environment, and it is the total of these various events that produce anatomical images.

5.2 MRI Background

The theory of MRI is rather complex. Protons in a magnetic field have spin, and this spin has a magnetic vector, causing the proton to act like a miniature magnet with a north and a south pole. When protons are placed in a magnetic field, the protons will either align in a low-energy state in the direction of the field, or in a high-energy state against the field. These energy levels are discrete as shown in Figure 5.1.

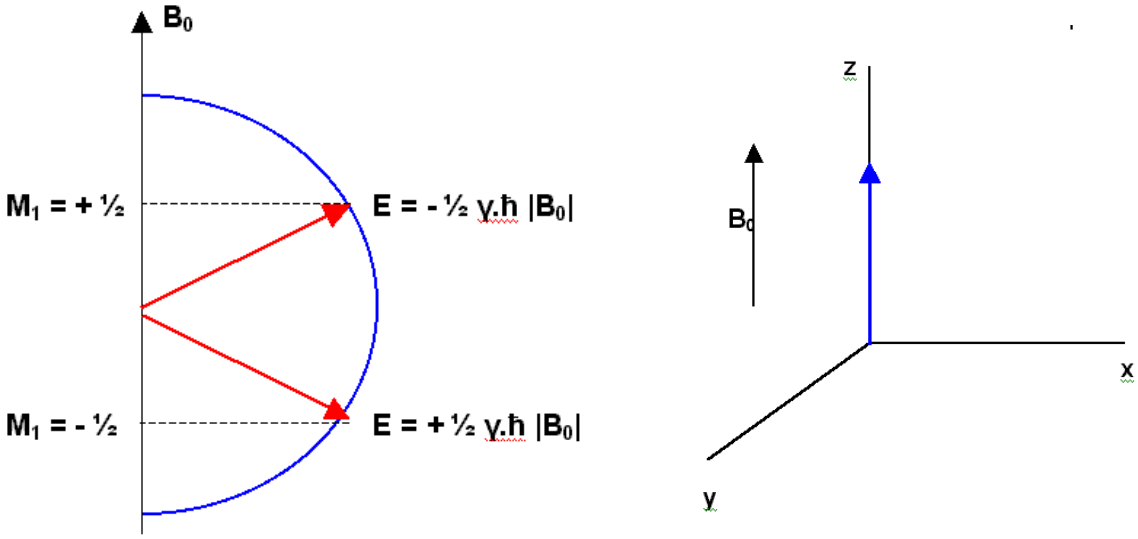

Figure 5.1 The energy levels of protons (spin ± ½) in a static magnetic field B0 (left), and the room temperature alignment of the lower energy proton with the external field (right).[139]

At room temperature, slightly more protons occupy the lower energy state, creating a small net magnetization in the direction of the external field as shown in Figure 5.1. Applying a radio

frequency pulse (B_1) in the x-y plane will rotate the net magnetization out of the B_0 direction and into the traverse plane. The flip angle is designated by theta θ, and depends on the strength and duration of the radio frequency pulse.

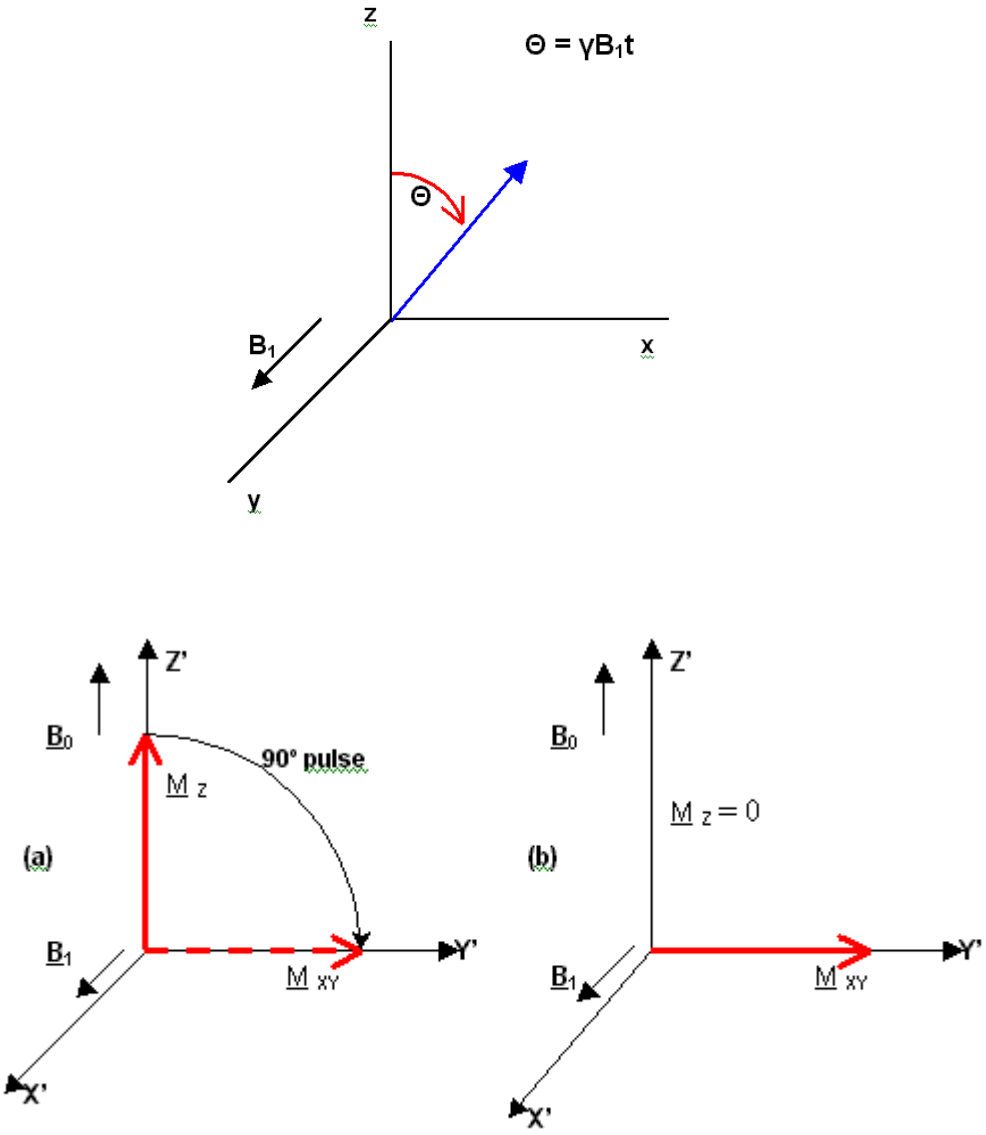

Figure 5.2 Excitation by radio frequency pulse (B_1) in the x-y plane (top) will rotate the net magnetization out of the B_0 direction and into the traverse plane (bottom).[139]

After radio frequency excitation, the magnetization (M) rotates around the applied field direction. If the pulse angle is 90°, there will be no component of magnetization (M) remaining in the M_z direction and all of the magnetization will be pushed into the x-y plane as shown in Figure 5.2. Following this excitation, the T_1 and T_2 relaxation times begin.

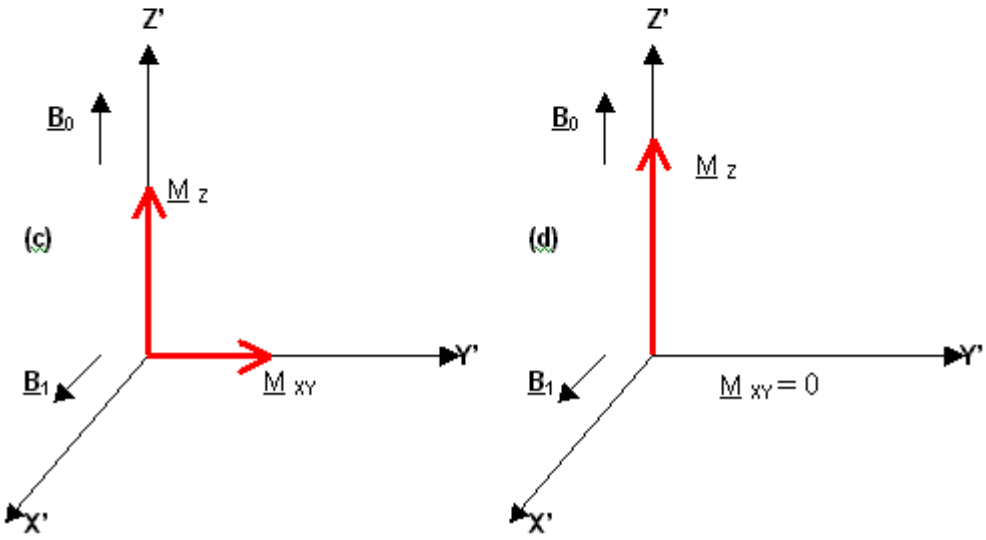

Figure 5.3 Re-growth of magnetization back into the M_z axes with loss of magnetization in the xy plane.[113]

Table 5.1 T_1 data at 0.5T and 1.5T along with T_2 data at 1.5T for various tissues.[139]

Tissue	T1 (0.5T) (msec)	T1 (1.5T) (msec)	T2 (msec)
Fat (adipose)	210	260	80
Liver	350	500	40
Muscle	550	870	45
White matter	500	780	90
Grey matter	650	900	100
CSF	1800	2400	160

The relaxation processes of T_1 and T_2 are related to biological parameters, such as tissue type, as illustrated in Table 5.1, and therefore provide a method of differentiating among tissues. T_1 is called the spin-lattice relaxation time, or longitudinal relaxation time, and is the time constant describing the rate at which excited protons dissipate excess energy to the environment or lattice. T_1 is the time it takes for the longitudinal magnetization to relax back to 63.2% of its initial value. After 5 times T_1, the sample is considered to be back to complete longitudinal magnetization. T_1 values range from 0.1 seconds to 1.0 second in soft tissues and from 1.0 second to 4 seconds in aqueous tissues. The T_1 relaxation time increases with external magnetic field strength as shown in Table 5.1. T_2 is the spin-spin or transverse relaxation time and is the time constant for the relaxation process in the x-y or traverse plane. T_2 is the time constant that describes the rate at which excited protons exchange energy, or lose phase coherence with each other. The time between the maximum transverse signal and 36.8% of the maximum is the T_2 decay constant. The relaxation processes of T_1 and T_2 are shown graphically in Figure 5.4.

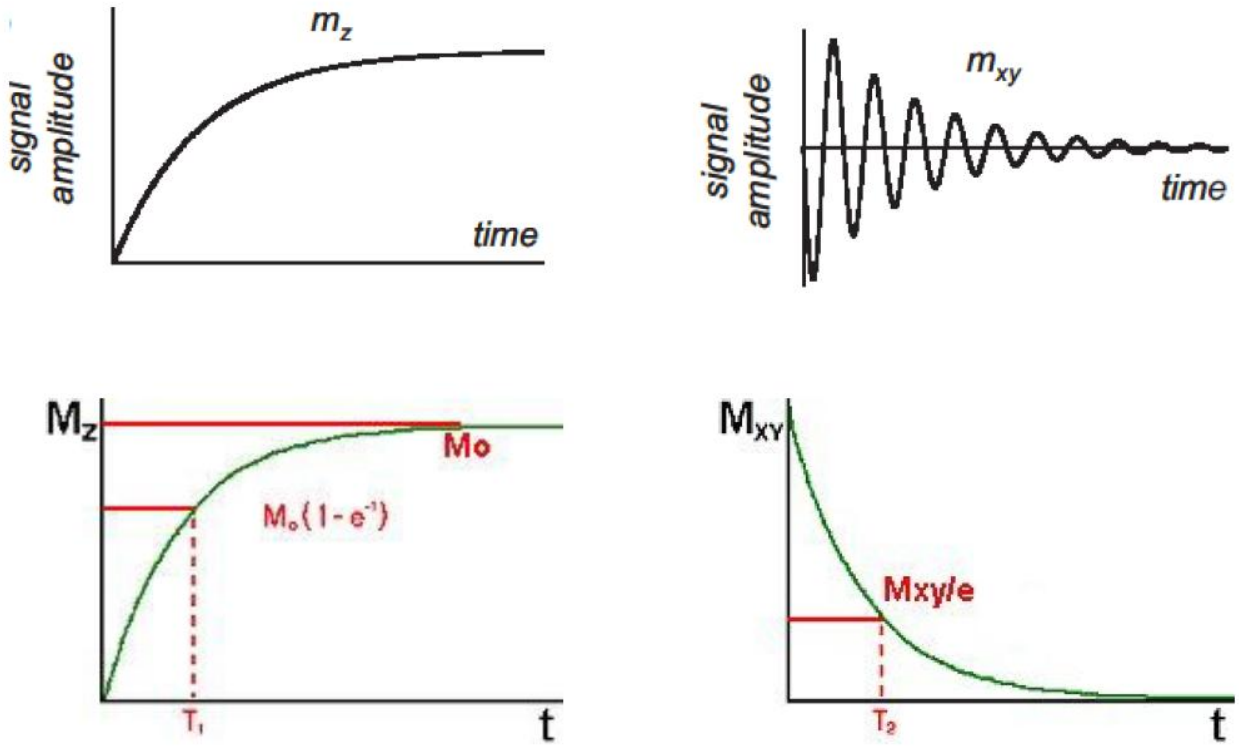

Figure 5.4 T_1 relaxation (left) and T_2 relaxation (right).[139]

Both T_1 and T_2 can be shortened by the use of magnetic contrast agents. The most common contrast agents are gadolinium ion complexes and iron oxide nanoparticles. Gadolinium agents are utilized for their ability to shorten T_1. T_1 agents generally increase the longitudinal or spin lattice relaxation rates of protons in tissues more than the transverse or spin-spin relaxation rates. Iron oxide agents are T_2 agents. Table 5.2 shows some of the gadolinium and iron oxide contrast agents that are in use today. A MRI image will appear brighter in the presence of gadolinium and appear darker in the presence of iron oxide. Figure 5.5 illustrates the effect of spin density as well as the contrast between T_1 and T_2 imaging times.

Table 5.2 Gadolinium and iron oxide contrast agents that are currently in use as MRI contrast agents.[139]

MR contrast agent	Main use	Molecular weight or PCS size	Relaxivity/(mM s)$^{-1}$	Target
Gd–DTPA	T_1-agent	0.6 kDa	$R_1 = 3.7$	• Extracellular
Dextran–Gd–DTPA	T_1-agent	75 kDa	$R_1 = 11$	• Blood-pool • Capillary permeability
Carboxydextran-coated SPIO SHU-555[b]	T_2-agent	62 nm	$R_1 = 12$; $R_2 = 188$ (0.94 T)	• MPS organs (liver)
Dextran-coated SPIO AMI-25[c]	T_2-agent	58 nm	$R_1 = 24$; $R_2 = 107$ (0.47 T)	
Dextran-coated USPIO MION-46L[d]	T_2-agent	18–24 nm	$R_1 = 16$; $R_2 = 35$ (0.47 T)	• MPS organs
Dextran-coated USPIO AMI-227[e]	T_2-agent	17–20 nm	$R_1 = 23$; $R_2 = 53$	• Lymph nodes

[a] Relaxivities were measured at 37 °C and the static magnetic field B_0 expressed in Tesla is noticed in brackets. [b] Ferucarbotran Resovist® from Schering, Germany [c] Endorem® from Guerbet, France or Feridex® from Advanced Magnetics, USA [d] Massachusetts General Hospital, Boston, USA [e] Sinerem® from Guerbet, France or Combidex® from Advanced Magnetics, USA

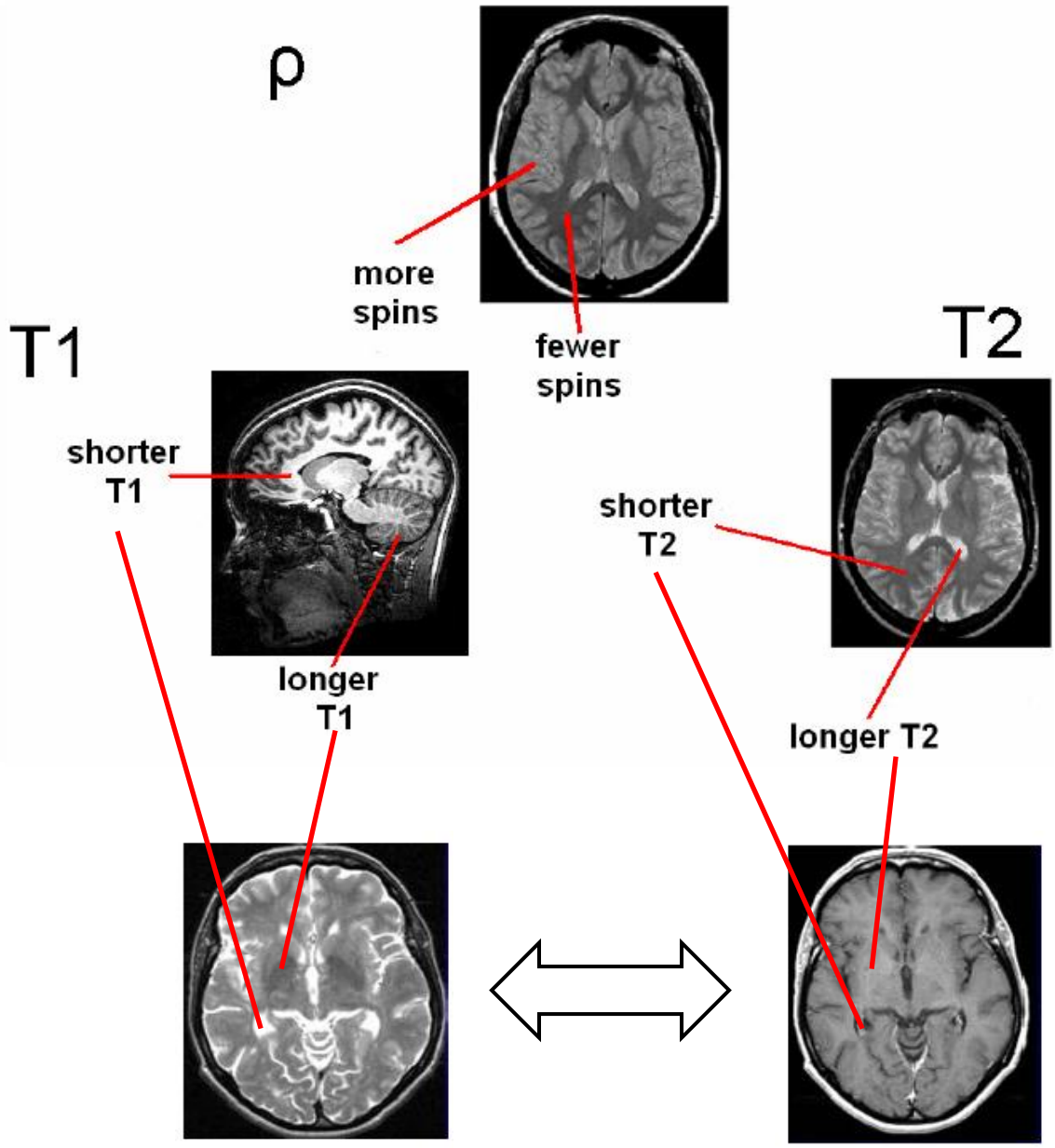

Figure 5.5 The effect of spin density (top) and the contrast between T_1 (left) and T_2 (right) imaging time parameters.[139]

Superparamagnetic iron oxide nanoparticles (SPIO) are used as contrast agents for their ability to shorten T_2 of water protons. The ability of the SPIO to reduce T_2 is related to the magnetic properties of the nanoparticles that produce a strong magnetic susceptibility effect on the water protons that diffuse around the nanoparticle. The magnetic susceptibility is directly related to the crystallinity and size of the nanoparticles. Most SPIO's are magnetite coated with a suitable biocompatible material with an average diameter between 60 and 250 nm. Particles with size ranges between 20 and 50 nm are commonly referred to as ultra-small superparamagnetic (USPIO) and produce a longer T_2 than their larger counterpart the SPIO. The role played by the particle size to affect T_2 is one of the challenges associated with using iron oxide nanoparticles as contrast agents, and is one of the focal points of the work done in this dissertation. The ability to effectively control the size, dispersion, and reproducibility is often a difficult process to control due to the colloidal nature of ferrites. Therefore, the search for experimental parameters that produce a monodisperse population of highly crystalline particles that are capable of being scaled up is a very active area of research of which this dissertation addresses. In addition to nanoparticles based solely on iron, alloy-based nanoparticles are beginning to appear which have a greater relaxivity than current particles that are based solely on iron. Some of these alloyed based particles include $CoFe_2O_4$ and $NiFe_2O_4$, both of which were a focus of this dissertation.

5.3 MRI Experimental

The cobalt and nickel ferrites described in Chapter 3 were investigated *in vitro* by magnetic resonance relaxivity measurements for its application in magnetic resonance imaging. The magnetic resonance imaging (MRI)/spectroscopic experiments were performed on a 2.4 T/40 cm bore MR system (Biospec/Bruker). Spectroscopic T_2 ^1H relaxation measurements of the aqueous ferrites were conducted using an inversion recovery sequence with eight inversion times (T_I) and repetition times (T_R) at least five times the expected T_1 value. For the T_2 measurements, a multi-spin-echo CPMG sequence was employed with several echo times (T_E) and T_R values at least five times the expected T_1. The relaxation times were computed from least-squares fitting of the exponentially varying signals using analysis routines available at the MR system.

5.4 MRI Data

Shown below in Figure 5.7 are the T_2 weighted MRI images of the 30 nm $CoFe_2O_4$ and 50 nm $CoFe_2O_4$ nanoparticles described previously in Chapter 3. The relaxivity rate, r_2, of the 30 nm $CoFe_2O_4$ was 192.8 $mM^{-1}s^{-1}$, and the relaxivity rate, r_2, of the 50 nm $CoFe_2O_4$ particles was 288.5 $mM^{-1}s^{-1}$.

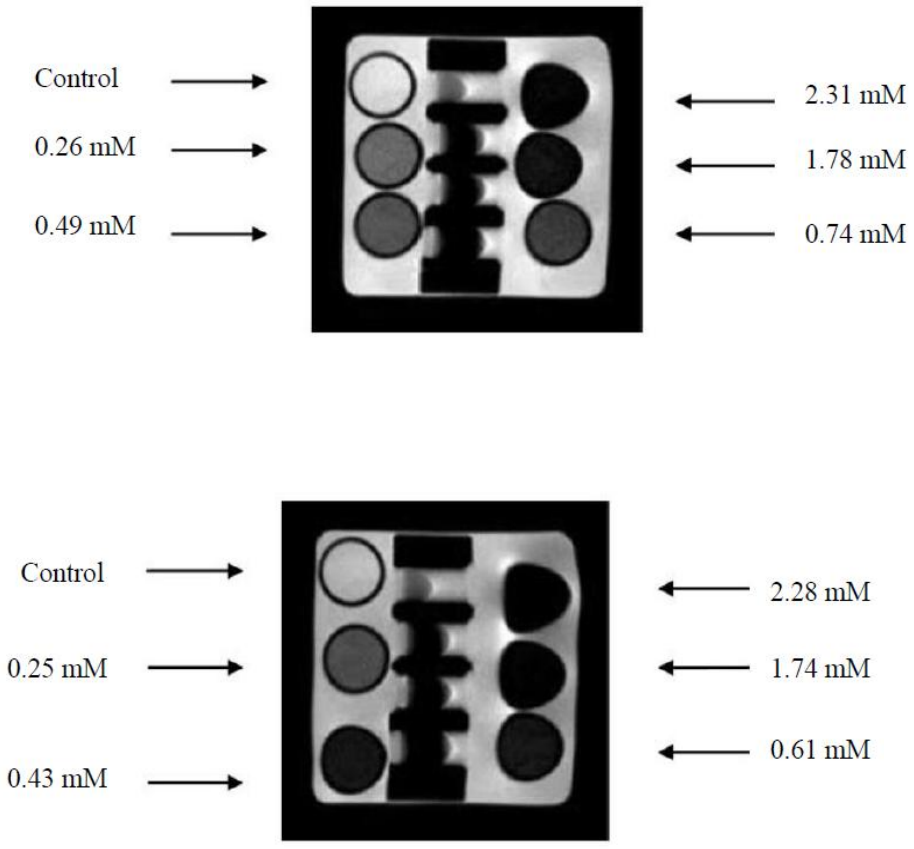

Figure 5.6 T_2 weighted images of the 30 nm $CoFe_2O_4$ particles (top) and the 50 nm $CoFe_2O_4$ particles (bottom).

Shown below in Figure 5.8 are the T_2 weighted MRI images of the 30 nm $NiFe_2O_4$ and 50 nm $NiFe_2O_4$ nanoparticles. The relaxivity rate, r_2, of the 30 nm $NiFe_2O_4$ was 175.1 $mM^{-1}s^{-1}$, and the relaxivity rate, r_2, of the 50 nm $NiFe_2O_4$ was 204.3 $mM^{-1}s^{-1}$.

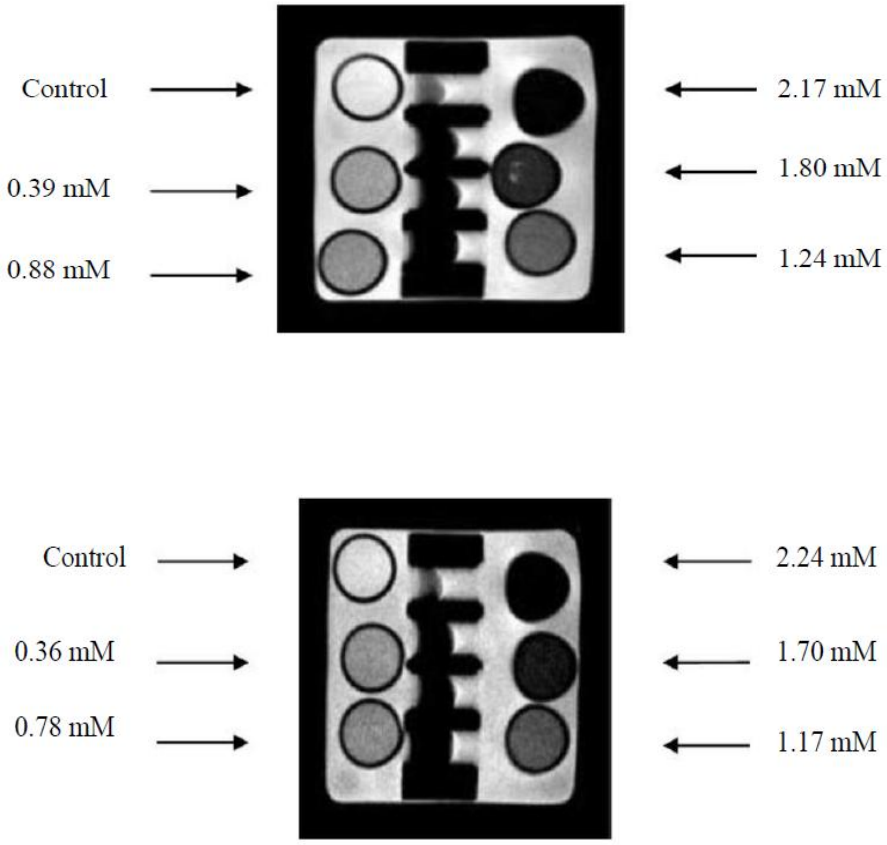

Figure 5.7 T_2 weighted images of the 30 nm $NiFe_2O_4$ particles (top) and the 50 nm $NiFe_2O_4$ particles (bottom).

Shown below in Figure 5.9 are the T_2 weighted MRI images of the 30 nm $Ni_{0.5}Co_{0.5}Fe_2O_4$ and 50 nm $Ni_{0.5}Co_{0.5}Fe_2O_4$ nanoparticles. The relaxivity rate, r_2, of the 30 nm $Ni_{0.5}Co_{0.5}Fe_2O_4$ was 121.4 $mM^{-1}s^{-1}$, and the relaxivity rate, r_2, of the 50 nm $Ni_{0.5}Co_{0.5}Fe_2O_4$ was 132.3 $mM^{-1}s^{-1}$.

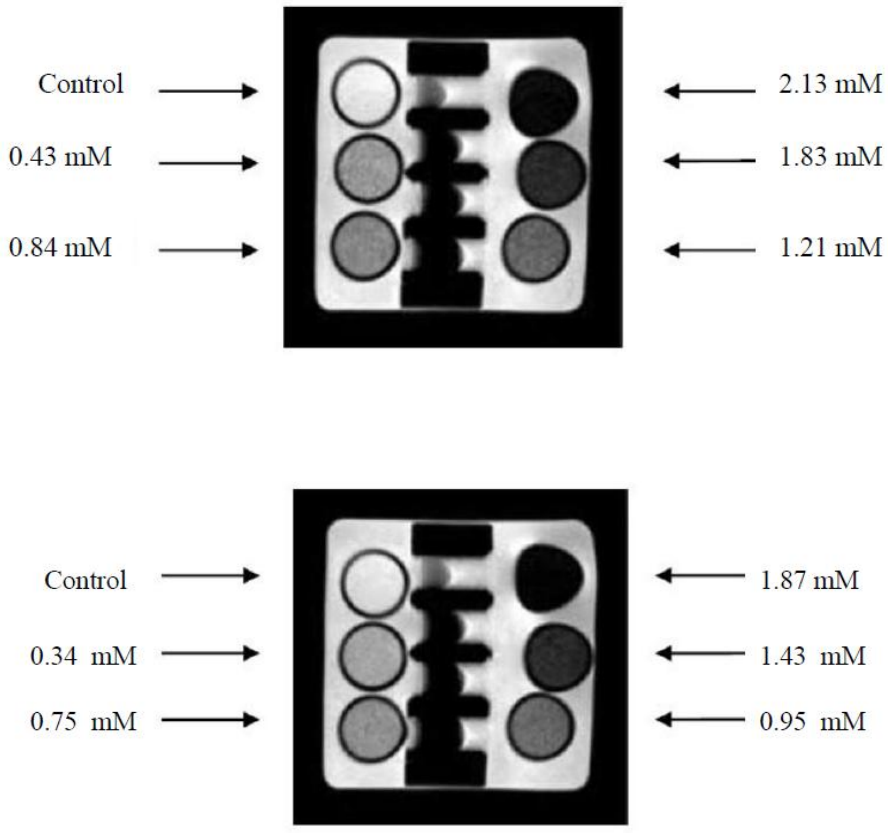

Figure 5.8 T_2 weighted images of the 30 nm $Ni_{0.5}Co_{0.5}Fe_2O_4$ particles (top) and the 50 nm $Ni_{0.5}Co_{0.5}Fe_2O_4$ particles (bottom).

5.5 Conclusions

Magnetic resonance imaging (MRI) was carried out to measure the transverse relaxation time (T_2) of a series of polyol produced, surface coated mixed metal ferrites of $CoFe_2O_4$, $NiFe_2O_4$, and $Ni_{0.5}Co_{0.5}Fe_2O_4$. The r_2 relaxivities were found to be in the range of 121.43 $mM^{-1}s^{1}$ to 288.48 $mM^{-1}s^{-1}$. These values can be compared to those of the commercial contrast agent Feridex, which is 191 $mM^{-1}s^{-1}$. Also noted was the size dependency of the nanoparticles on the measured relaxivity (r_2). The higher relaxivity values observed for larger nanoparticles are expected, as faster spin-spin relaxation processes of water molecules are brought about by particles with larger magnetization values. Among the mixed metal ferrites studied, the 50 nm $CoFe_2O_4$ had the greatest MRI enhancement effect and the 30 nm $Ni_{0.5}Co_{0.5}Fe_2O_4$ had the lowest effect. Further understanding of how ferrite composition and crystallite size effect their magnetic properties and resulting MRI contrast abilities will provide insight into the best materials for the next generation of contrast agents.

Chapter 6: Conclusions and Future Work

This work has focused on several area of nanoparticle research that would have broad implications in biological separations and magnetic resonance imaging contrast enhancement. The use of magnetic nanoparticles in biological separations has made major developments in recent years in the range of tools available to scientist and clinicians. For example, in biomedicine it is very advantageous to separate biological entities from their environment in order to concentrate samples for subsequent analysis. Magnetic separations using biocompatible iron oxide nanoparticles are one way to achieve this with high precision. It is a three step process, involving (i) the synthesis of high quality magnetic particles with size tunable properties, (ii) surface coating the particles with organic and inorganic matrixes to promote stabilization and provide functionalization for attachment to bio-molecules of interest, and (iii) the magnetic separation of the nanoparticle and its tagged entity from their surroundings for subsequent analysis.

The synthesis of magnetic nanoparticles has made substantial progress, especially in the past ten years; however, synthesis of high quality nanoparticles in a controlled manner with a detailed understanding of the mechanisms of nucleation and growth during particle formation are still challenges to address in the coming years. Furthermore, the large scale synthesis of iron oxide nanoparticles requires a reproducible and industrial process without a labor intensive purification steps. Also, a recurring problem associated with nanoparticles is their instability over long periods of time. Nanoparticles tend to form agglomerates; therefore, it is necessary to

develop coating strategies to improve the chemical stability of the particles. The influence of the coating layer on the structural and magnetic properties of iron oxides needs to be further investigated in order to be able to better describe the forces involved in the surface binding of the coatings. Surface coatings can lead to a decrease in the magnetization of nanoparticles. This reduction has been associated with the existence of a magnetically dead layer on the surface of the particle. The nature of the surface coatings as well as the physical arrangement of the coating on the iron oxide surface will not only determine the size of the nanoparticle, but also regulate the bio-distribution properties.

The use of appropriately coated nanoparticles to separate out *E. coli* O157:H7 from a food suspension with subsequent analysis by MALDI-TOF/MS was demonstrated in Chapter 4. The knowledge gained by this process can be extended to the rapidly growing field of proteomic research. MALDI-TOF/MS peptide mapping is a powerful analytical technique for the identification and characterization of proteins. This technique involves enzymatic cleavage of the intact protein by proteases, followed by the mass determination of the generated peptides and identification of the protein by matching the peptide fragments to a theoretical digestion pattern in a database.[140] The ability of nanoparticles to disperse in the small sample volumes present on a MALDI plate could make the process of sample digestion, removal of the nanoparticle from MALDI plate, and subsequent mass analysis a short and simple process as demonstrated in Figure 6.1. This simplistic approach to protein digestion directly on the MALDI plate should offer a promising method for rapid automated analysis in the field of proteomic research.

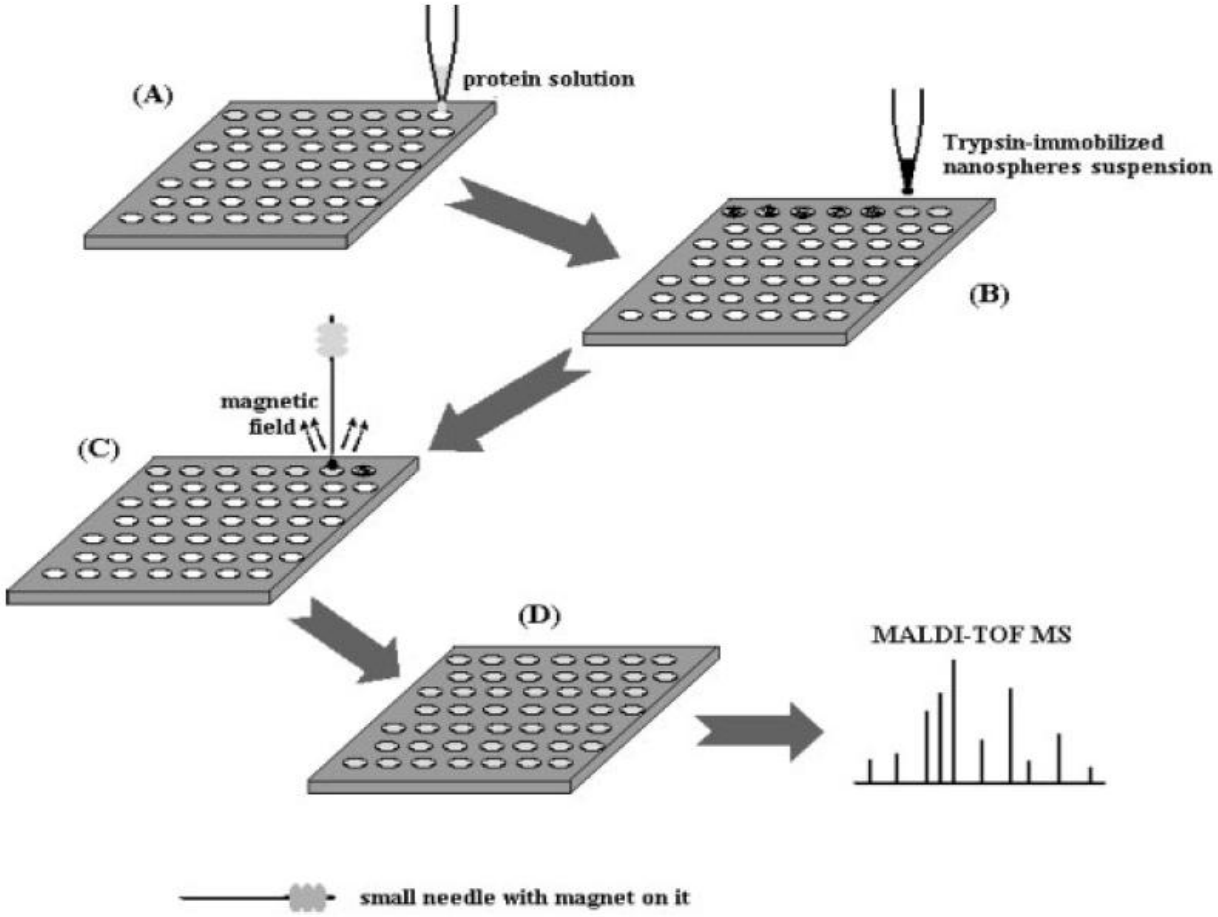

Figure 6.1 Diagram showing the procedure for the on plate digestion of proteins with the aid of magnetic nanoparticles. (A) protein solution is first loaded onto the plate, (B) trypsin-linked magnetic nanoparticles are added to the protein solution, (C) after digestion, the nanoparticles can be easily removed from the plate with the use of a magnetized needle, and (D) a matrix solution is added and the sample is ready for MALDI-TOF/MS analysis.[140]

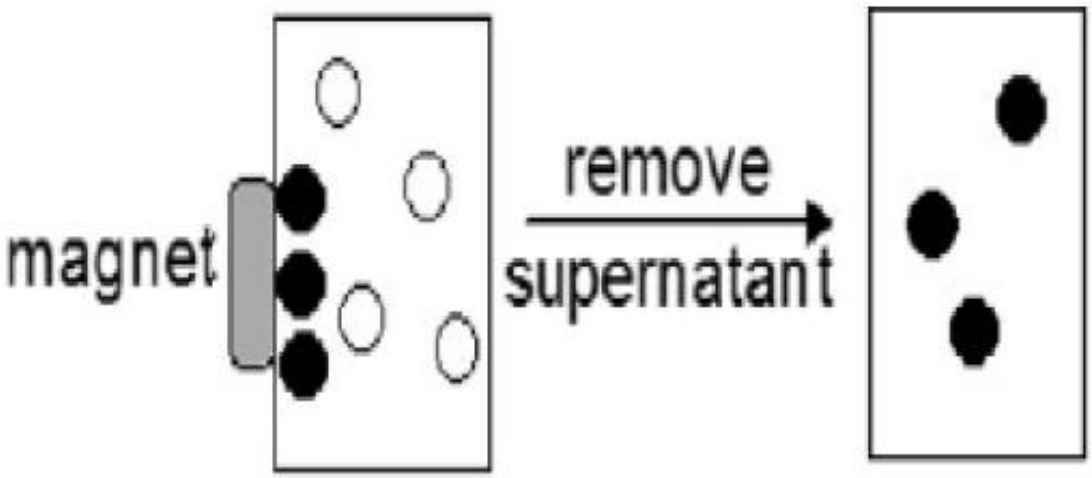

Figure 6.2 Magnetic separations using a permanent magnet attached to the wall of a test tube.[141]

Further studies should also address the different challenges associated with magnetically separating the nanoparticle and their targets from their surroundings. Magnetic separator design can be as simple as the application and removal of a permanent magnet to the wall of a test tube to promote the aggregation, followed by the removal of the supernatant as shown in Figure 6.2. This method can be limited by slow accumulation rates. It is preferable to have regions of high magnetic field to capture the magnetic nanoparticles as they flow by in their carrier medium. The typical way to achieve this is to loosely pack a column with a magnetic matrix of wires or beads, and then pump the magnetically tagged fluid through the column while a field is applied as shown in Figure 6.3.[141] This method is faster than the previous technique; however, problems can arise due to the adsorption of magnetically tagged material onto the matrix.

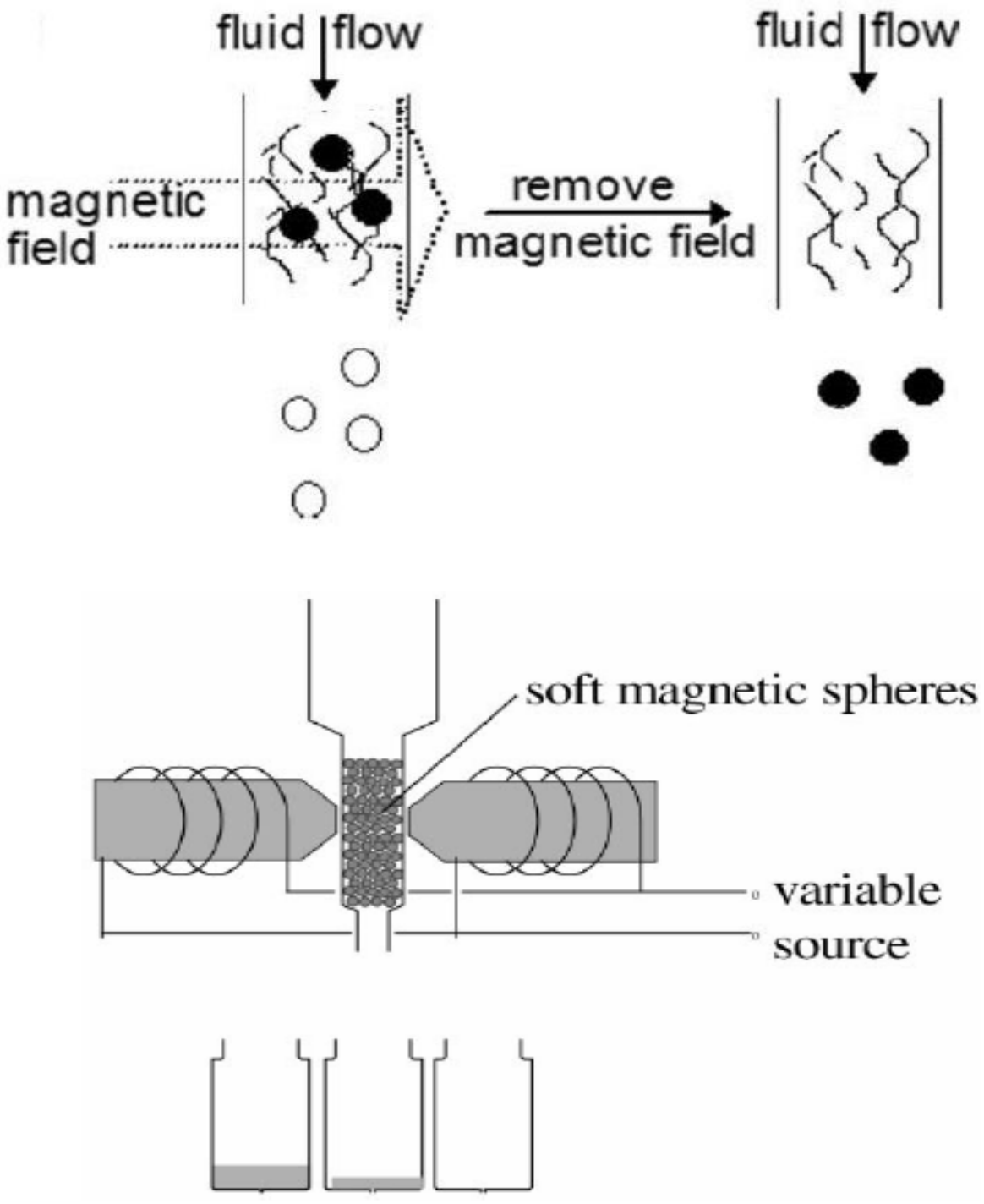

Figure 6.3 Magnetic separator design utilizing a loosely packed column of magnetic wires or beads.[141]

An alternative method which does not involve any obstruction placed in the column is the use of a quadrapole magnetic field- flow fractionation system which creates a magnetic gradient radially outward from the center of the flow column as shown in Figure 6.4.[141] Under the action of the magnetic field gradient, the tagged particles move to the column walls where they are held

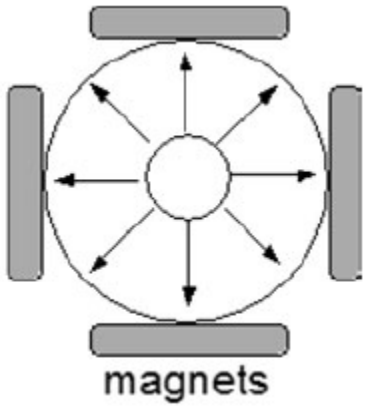

Figure 6.4 Magnetic separator design based on a quadrapole magnetic arrangement.[141]

until the field is removed. As well as separating out the magnetically tagged material, the spatially varying magnitude of the field gradient is used to create a field- flow fractionation approach. Field-Flow Fractionation (FFF) is a separation and characterization technique for macromolecules, colloids, and particles. FFF combines the elements of chromatography and field-driven techniques such as electrophoresis. FFF is a an elution technique, the field in FFF acts not to directly drive the separation, instead, the field is applied at right angles to the flow and serves to drive components into different stream flow velocities. The unequal flow velocities cause the separation, which takes place along the flow axis.[142] The FFF mechanism is illustrated in Figure 6.5.

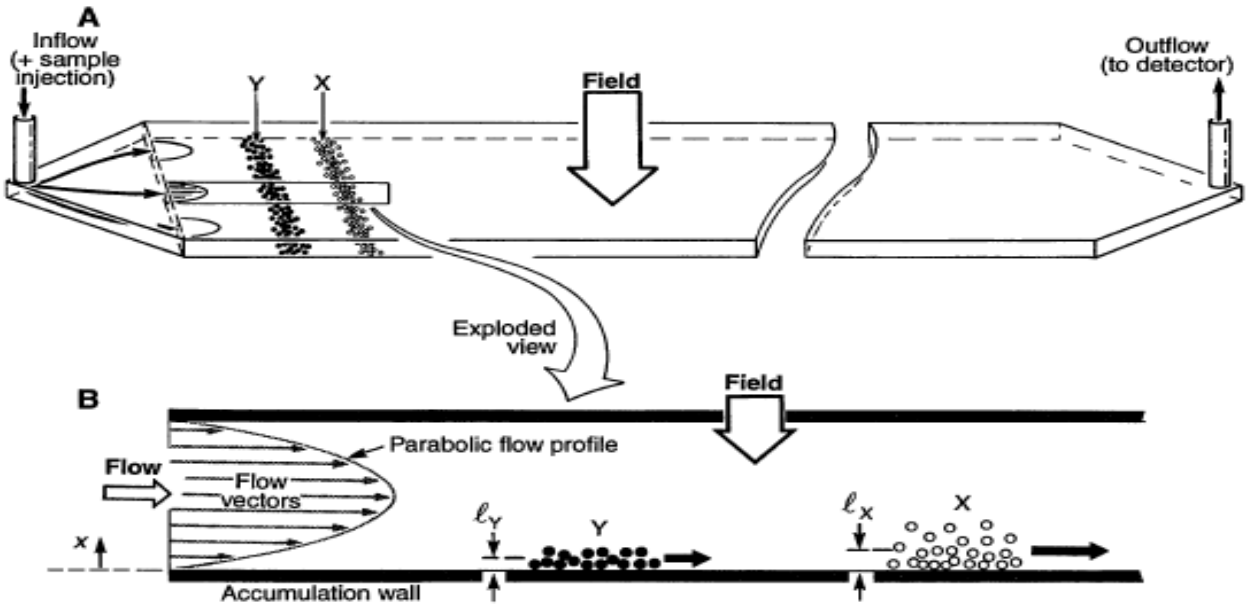

Figure 6.5 Diagram of Field-Flow Fractionation of magnetic nanoparticles.[142]

Magnetic separation has been applied to many aspects of biomedical and biological research. It has proven to be a very sensitive technique for the detection of tumor cells and malarial parasites in blood, and it has been used as a pre-processing technology for polymerase chain reactions, through which the DNA of a sample is amplified and identified. In another application, magnetic nanoparticles that have been surface coated with a styrene-divinylbenzene copolymer can be utilized as a packing matrix for ultra high pressure liquid chromatography. The use of 3 μm diameter non-porous particles for reversed phase liquid chromatography has been shown to increase resolution and reduce analysis time.[155] The shorter diffusion path of

nanoparticles that have been surface coated with a styrene-divinylbenzene copolymer reduces axial dispersion of solutes and minimizes peak broadening as shown in Figure 6.6. This technology can be applied to the challenging task of the analysis of intact proteins and proteolytic digested proteins. To test the ability of nanoparticles to serve as a stationary material for reversed phase ultrahigh pressure liquid chromatography, I compared a commercial column to a column packed with styrene coated iron oxide nanoparticles. Currently, there are no UPLC columns described in the literature that contain styrene coated iron oxide nanoparticles, as this clearly represents a novel process. The commercial column was an Acuity UPLC® BEH300 C18 1.7µm 2.1 X 150 mm column obtained from Waters Corporation. Figure 6.7 shows an overlay of both chromatograms. Both columns show very similar results for the ten proteins used in the evaluation. The added benefit of the particles being magnetic offers the possibility to manipulate retention times by placing the HPLC column into an external magnetic field as shown in Figure 6.8.

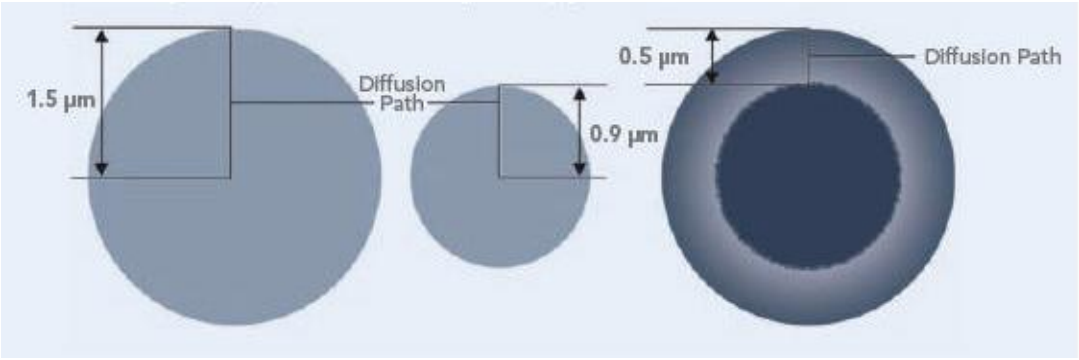

Figure 6.6 Porous packing material (left) and iron oxide nanoparticles that have been surface coated with a styrene-divinylbenzene copolymer (right).

Protein	Mass (kDa)
1. RNase A	13.7
2. Cytochrome C	12.2
3. Insulin	5.7
4. Lysozyme	14.3
5. BSA	66.4
6. α-Lactalbumin	14.2
7. Myoglobin	17.0
8. Trypsin Inhibitor	20.0
9. Chymotrypsinogen A	25.7
10. Ovalbumin	44.3

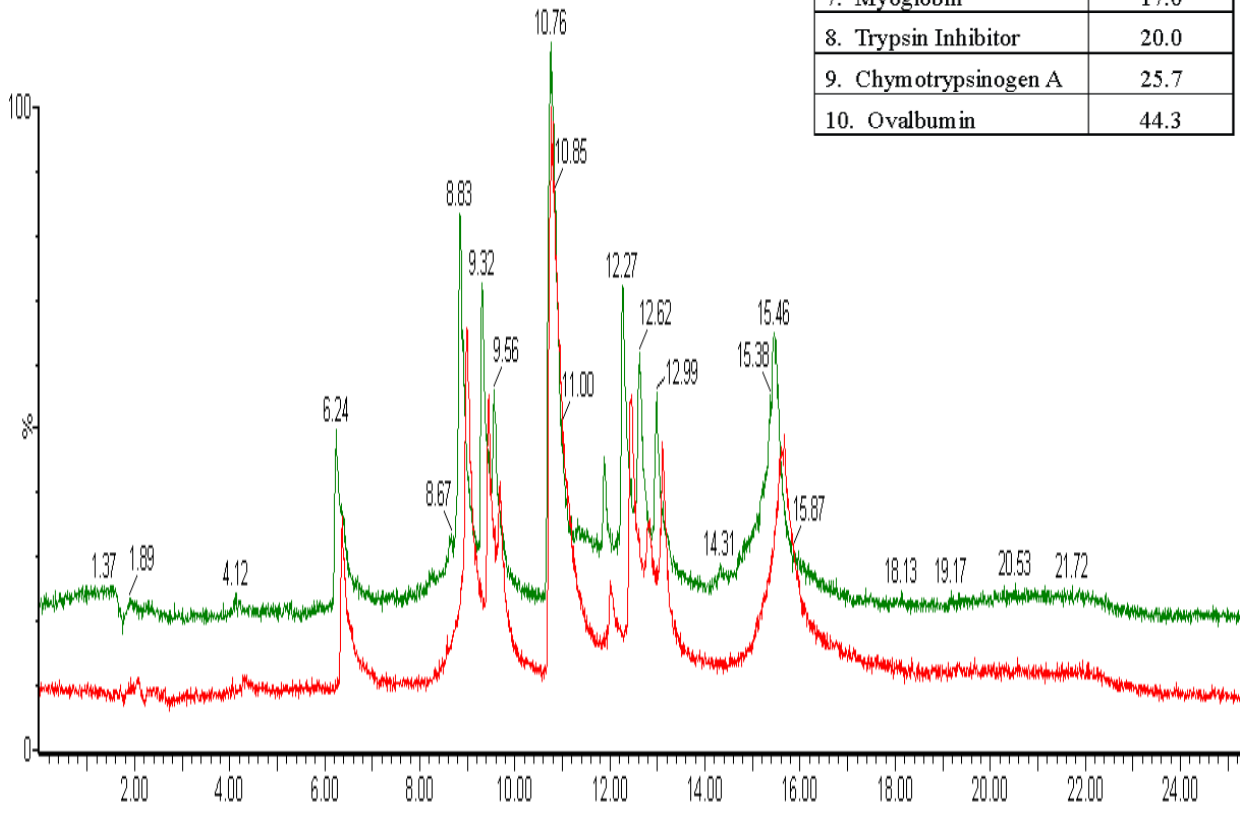

Figure 6.7 Results obtained using typically employed HPLC conditions (column temperature = 35 °C and acetonitrile was the organic modifier used) The 10 proteins used in the column comparison and their masses are provided in the inset table (top), and the chromatogram obtained from the Acuity UPLC® BEH300 C18 1.7µm 2.1 X 150 mm column from Waters Corporation (green), and the chromatogram obtained from the column with iron oxide nanoparticles surface coated with a styrene-divinylbenzene copolymer (red).

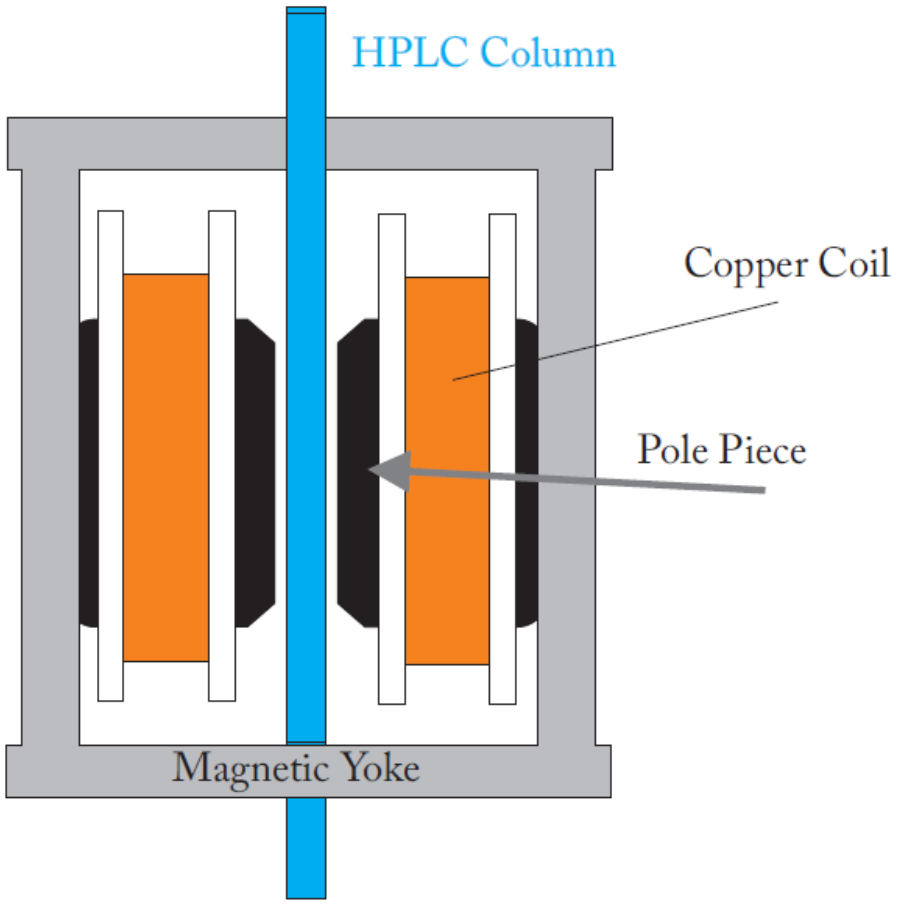

Figure 6.8 Magnetic separator design of a HPLC column with a magnetic stationary phase placed inside a variable external magnetic field.

In this dissertation, I have reviewed the magnetic properties of iron oxide nanoparticles and have detailed some of the synthesis strategies that produce and surface coat the particles for further applications. This paper has focused on the applications of nanoparticles in the areas of biological separations and magnetic resonance imaging contrast enhancement. These are only two of the many biomedical applications of magnetic nanoparticles that are currently being explored. For example, research is being conducted on drug delivery, hyperthermia, and tissue engineering applications. In summary, one of the biggest challenges in biomedical applications with nanoparticles is dealing with the issue of technology transfer. There are a multitude of opportunities for more interdisciplinary approaches that ensure that proof of concept studies should actually be carried out *in vivo*. Lastly, safety and biocompatibility studies, as well as long term toxicity studies should be performed that address whether laboratory experiments can imitate the conditions that would be found *in vivo*.

References

(1) Sun, S.; Murray, C. B.; Weller, D.; Folks, L.; Moser, A. *Science* **2000**, *287*, 1989.

(2) Miller, M. M.; Prinz, G. A.; Cheng, S. F.; Bounnak, S. *Appl. Phys. Lett.* **2002**, *81*, 2211.

(3) Jain, T. K.; Morales, M. A.; Sahoo, S. K.; Leslie-Pelecky, D. L.; Labhasetwar, V. *Mol. Pharm.* **2005**, *2* (3), 194.

(4) Chourpa, I.; Douziech-Eyrolles, L.; Ngaboni-Okassa, L.; Fouquenet, J. F.; Cohen-Jonathan, S.; Souce, M.; Marchais, H.; Dubois, P. *Analyst* **2005**, *130* (10), 1395.

(5) Huber, D. L. *Small* **2005**, *1*, 482.

(6) Burda, C.; Chen, X.; Narayanan, R.; El-Sayed, M. A. *Chemical Review* **2005**, *105*, 1025
.
(7) Srivastava, C.; Nikles, D. E.; Thompson, G. B. *J. Appl Phys* **2008**, *104*, 104314.

(8) Alivisatos, A. P. *Science* **1996**, *271*, 933.

(9) Hu, C. H.; Jiang, J. F.; Cai, Q. Y. *Supercond. Sci. Technol.* **2002**, *15*, 330.

(10) Hua, Q.; et al. *Nanotech* **2010**, *21*, 215706.

(11) Kastner, M. A. *Rev Mod Phys* **1992**, *64*, 849.

(12) McMurry, J.D.;Fay, R.C. *Chemistry;* 5th ed.; Pearson Prentice Hall, New Jersey, 2008

(13) Wang, Y.; Herron, N. *Physical Review B* **1990**, *42*, 7253.

(14) Johansson, K. P.; McLendon, G.; Marchetti, A. P. *Chem. Phys. Lett.* **1991**, *179*, 321.

(15) Rossetti, R.; Hull, R.; Gibson, J. M.; Brus, L. E. *J. Chem Phys* **1985**, *83*, 1406.

(16) Dannhauser, T.; O'Neil, M.; Johansson, K.; Whitten, D.; McLendon, G. *J. Phys Chem* **1986**, *90*, 6074.

(17) Lin, S. T.; Franklin, M. T.; Klabunde, K. J. *Langmuir* **1986**, *2*, 259.

(18) Glaspell, G. P.; Zuo, C.; Jagodzinski, P. W. *J. Cluster Science* **2005**, *16*, 39.

(19) Jun, B.-H.; Noh, M. S.; Kim, J.; Kim, G.; Kang, H.; Kim, M.-S.; Seo, Y.-T.; Baek, J.; Kim, J.-H.; Park, J.; Kim, S.; Kim, Y.-K.; Hyeon, T.; Cho, M.-H.; Jeong, D. H.; Lee, Y.-S. *Small* **2009**,*9999*, NA.

(20) Kim, K.; Jang, H. J.; Shin, K. S. *Analyst* **2009**, *134*, 308.

(21) Kneipp, K.; Kneipp, H.; Manoharan, R.; Hanlon, E. B.; Itzkan, I.; Dasari, R. R.; Feld, M. S.*Appl. Spectrosc.* **1998**, *52*, 1493.

(22) Kneipp, K.; Kneipp, H.; Manoharan, R.; Itzkan, I.; Dasari, R. R.; Feld, M. S. *J. Raman Spectrosc.* **1998**, *29*, 743.

(23) Li, X.; Zhang, J.; Xu, W.; Jia, H.; Wang, X.; Yang, B.; Zhao, B.; Li, B.; Ozaki, Y. *Langmuir***2003**, *19*, 4285.

(24) Michaels, A. M.; Jiang, J.; Brus, L. *J. Phys. Chem. B* **2000**, *104*, 11965.

(25) *Hao, E.; Schatz, G. C. J. Chem. Phys. 2004, 120, 357–366*

(26) Noh, M. S.; Jun, B.-H.; Kim, S.; Kang, H.; Woo, M.-A.; Minai-Tehrani, A.; Kim, J.-E.; Kim, J.;Park, J.; Lim, H.-T.; Park, S.-C.; Hyeon, T.; Kim, Y.-K.; Jeong, D. H.; Lee, Y.-S.; Cho, M.-H.*Biomaterials* **2009**, *30*, 3915.

(27) Sato-Berru, R.; Redon, R.; Vaquez-Olmos, A.; Saniger, J. M. *J. Raman Spectrosc.* **2009**, *40*,376.

(28) Sevilla, P.; Garcia-Blanco, F.; Garcia-Ramos, J. V.; Sanchez-Cortes, S. *Phys. Chem. Chem Phys.* **2009**, *11*, 8342.

(29) Shkilnyy, A.; Souce, M.; Dubois, P.; Warmont, F.; Saboungi, M. L.; Chourpa, I. *Analyst* **2009**, *134*, 1868.

(30) Torreggiani, A.; Jurasekova, Z.; D'Angelantonio, M.; Tamba, M.; Garcia-Ramos, J. V.; Sanchez-Cortes, S. *Colloids and Surfaces a-Physicochemical and Engineering Aspects* **2009**, *339*, 60.

(31) Xu, H. X.; Aizpurua, J.; Kall, M.; Apell, P. *Physical Review E* **2000**, *62*, 4318.

(32) Freestone, I.; Meeks, N.; Sax, M.; Higgitt, C. *Gold Bulletin* **2007**, *40*, 270.

(33) Martin, T. P.; Naher, U.; Schaber, H.; Zimmermann, U. *The Journal of Chemical Physics* **1994**, *100*, 2322.

(34) Leslie-Pelecky, Diandra .; Rieke, Reuben. *Chem. Mater.* **1996,** *8*, 1770-1783

(35) Cullity, B. D.; Graham, C. D. *Introduction to Magnetic Materials*; 2 ed.; John Wiley & Sons: Hoboken, New Jersey, 2009.

(36) Cornell, RM.; Schwertmann, U. *The Iron Oxides: Structure,Properties, Reactions, Occurrences and Uses*. Weinheim: Wiley-VCH; 2003.

(37) N´eel, L. *Ann Phys (Paris)* **1948**, 3:137–198.

(38) Chin, A. B.; Yaacob, I. I. *J. Mater. Process. Technol.* **2007**, *191*, 235–237.

(39) Albornoz, C.; Jacobo, S. E. *J. Magn. Magn. Mater*. **2006**, *305*, 12. *Mater.* **2005**, *289*, 328.

(40) Kim, E. H.; Lee, H. S.; Kwak, B. K.; Kim, B. K. *J. Magn. Magn.*

(41) Wan, J.; Chen, X.; Wang, Z.; Yang, X.; Qian, Y. *J. Cryst. Growth* **2005**, *276*, 571.

(42) Kimata, M.; Nakagawa, D.; Hasegawa, M. *Powder Technol.* **2003**, *132*, 112.

(43) Alvarez, G. S.; Muhammed, M.; Zagorodni, A. A. *Chem. Eng. Sci.* **2006**, *61*, 4625

(44) Martinez-Mera, I.; Espinosa, M. E.; Perez-Hernandez, R.; Arenas-Alatorre, J. *Mater. Lett.* **2007**, *61*, 4447–4451.

(45) Morisson, S. A.; Cahill, C. L.; Carpenter, E.; Calvin, S.; Harris, V. G. *J. Nanosci. Nanotechnol.* **2005**, *5*, 1323.

(46) Sun, Y.-K.; Ma, M.; Zhang, Y.; Gu, N. *Colloids Surf., A* **2004**, *245*, 15.

(47) Qiu, J.; Yang, R.; Li, M.; Jiang, N. *Mater. Res. Bull.* **2005**, *40*, 1968.

(48) Lee, S.-J.; Jeong, J.-R.; Shin, S.-C.; Kim, J.-C.; Kim, J.-D. *J. Magn Magn. Mater.* **2004**, *282*, 147.

(49) LaMer, V. K.; Dinegar, R. H. *J. Am. Chem. Soc.* **1950**, *72*, 4847.

(50) Sugimoto T *Fine Particles: Synthesis, Characterisation and Mechanism of Growth* (New York: Marcel Dekker) **2000**

(51) Burda, C.; Chen, X.; Narayanan, R.; El-Sayed, M. A. *Chemical Review* **2005**, *105*, 1025.

(52) LeFort, J., C. R. *Acad. Sci. Paris*, vol. 34, p. 480, **1852**

(53) Tominaga, M.; Matsumoto, M.; Soejima, K.; Taniguchi, I. *J. Colloid Interface Sci.* **2006**, *299*, 761.

(54) Weissleder, R. U.S. Patent 5,492,814, 1996; *Chem. Abstr.* 1997, *124*, 283285.

(55) Sjorgren, C. E.; Briley-Saebo, K.; Hanson, M.; Johansson, C. *Magn. Reson. Med.* **1994**, *31*, 268.

(56) Itoh, H.; Sugimoto, T. *J. Colloid Interface Sci.* **2003**, *265*, 283.

(57) Thapa, D.; Palkar, V. R.; Kurup, M. B.; Malik, S. K. *Mater. Lett.* **2004**, *58*, 2692.

(58) Pardoe, H.; Chua-anusorn, W.; St. Pierre, T. G.; Dobson, J. *J. Magn. Magn. Mater* **2001**, *225*, 41.

(59) Khalafalla, S. E.; Reimers, G. W. *IEEE Trans. Magn.* **1980**, *16*, 178.

(60) Massart, R. *IEEE Trans. Magn.* **1981**, *17*, 1247.

(61) Massart, R.; Cabuil, V. *J. Chim. Phys.* **1987**, *84*, 7.

(62) Lisiecki, I,; Pileni, M. P. *J. Am. Chem.* **1993**, *Soc.* 7, 115.

(63) Zhang, K.; Chew, C. H.; Xu, G. Q.; Wang, J.; Gan, L. M. *Langmuir*. **1999,** 15, 3056.

(64) Zarur, A. J.; Ying, J. Y. *Nature.* **2000,** 403, 65.

(65) Tartaj, P.; De Jonghe, L. C. *J. Mater. Chem.* **2000**, 10, 2786.

(66) Tartaj, P.; Tartaj, J. *Chem. Mater.* **2002** 14, 536.

(67) Pileni, M. P. *Nature Mater.* **2003,** 2, 145.

(68) Feltin, N.; Pileni, M. P. *Langmuir,* **1997** 13, 3927.

(69) L´opez-Quintela, M. A.; Rivas, J. *J. Colloid Interface Sci.* **1993** 158, 446.

(70) Carpenter, E. E. *J. Magn. Magn. Mater*, **2001,** 225, 17.

(71) Boutonnet, M.; Kizling, J.; Stenius, P. *Colloids Surf.* **1982** A, **5,** 209.

(72) Fievet, F.; Lagier, J. P.; Blin, B.; Beaudoin, B.; Figlarz, M. *Solid State Ionics* **1989**, *198*, 32.

(73) Tzitzios, V. K.; Petridis, D.; Zafiropoulou, I.; Hadjipanayis, G.; Niarchos, D. *J. Magn. Magn. Mater.* **2005**, *294* (2), e95.

(74) Chow, G. M.; Kurihara, L. K.; Kemner, K. M.; Schoen, P. E.; Elam, W. T.; Ervin, A.; Keller, S.; Zhang, Y.D. ; Budnick, J.; Ambrose, T. *J. Mater. Res.* **1995**, *10*, 1546.

(75) Chow, G. M.; Kurihara, L. K.; Schoen, P. E. U.S. Patent 6,436,167, 2002; *Chem. Abstr.* 2003, *137*, 173223.

(76) Viau, G.; Ravel, F.; Acher, O.; Fie´vet-Vincent, F.; Fie´vet, F. *J. Appl. Phys.* **1994**, *76*, 6570.

(77) Viau, G.; Ravel, F.; Acher, O.; Fie´vet-Vincent, F.; Fie´vet, F. *J. Magn. Magn. Mater.* **1995**, *140-144*, 377.

(78) Viau, G.; Fie´vet-Vincent, F.; Fie´vet, F. *J. Mater. Chem.* **1996**, *6*, 1047.

(79) Viau, G.; Fie´vet-Vincent, F.; Fie´vet, F. *Solid State Ionics* **1996**, *84*, 259.

(80) Viau, G.; Fie´vet-Vincent, F.; Fie´vet, F.; Toneguzzo, P.; Ravel, F.; Acher, O. *J. Appl. Phys.* **1997**, *81*, 2749.

(81) Toneguzzo, P.; Acher, O.; Viau, G.; Fie´vet-Vincent, F.; Fie´vet, F. *J. Appl. Phys.* **1997**, *81*, 5546.

(82) Toneguzzo, P.; Viau, G.; Acher, O.; Fie´vet-Vincent, F.; Fie´vet, F. *Ad*v. *Mater.* **1998**, *10*, 1032.

(83) Toneguzzo, P.; Acher, O.; Viau, G.; Pierrard, A.; Fie´vet-Vincent, F.; Fie´vet, F.; Rosenman, I. *IEEE Trans. Magn.* **1999**, *35*, 3469.

(84) Mercier, D.; Le´vy, J.-C.S.; Viau, G.; Fie´vet-Vincent, F.; Fie´vet, F.; Toneguzzo, P.; Acher, O. *Phys. Re*V. *B: Condens. Matter Mater. Phys.* **2000**, *62*, 532.

(85) Viau, G.; Toneguzzo, P.; Pierrard, A.; Acher, O.; Fie´vet-Vincent, F.; Fie´vet, F. *Scr. Mater.* **2001**, *44*, 2263.

(86) Yu, S.; Chow, G. M. *J. Nanosci. Nanotechnol.* **2006**, *6* (7), 2135.

(87) Giri, A. K.; Chowdary, K. M.; Majetich, S. A. *Mater. Phys. Mech.* **2000**, *1*, 1.

(88) Hegde, M. S.; Larcher, D.; Dupont, L.; Beaudoin, B.; Tekaia-Elhsissen, K.; Tarascon, J. M. *Solid State Ionics* **1997**, *93*, 33.

(89) Derjaguin, B. V.; Landau, L. *Acta Physicochim. URSS* **1941**, *14*, 633.

(90) Verwey, E. J. W.; Overbeek, J. T. G. *Theory of the Stability of Lyophobic Colloids*; Elsevier: Amsterdam, The Netherlands, **1948.**

(91) Cornell, R. M.; Schwertmann, U. *Iron Oxides in the Laboratory: Preparation and Characterization*; VCH Publishers: Weinheim, Germany, **1991.**

(92) Hafeli, U.; Schu¨tt, W.; Teller, J.; Zbrorowski, M. *Scientific and Clinical Applications of Magnetic Carriers*; Plenum Press: New York, **1997**.

(93) Arshady, R. *Radiolabeled and Magnetic Particles in Medicine and Biology*; Critrus Books: London, U.K., **2001**; Vol. 3.

(94) Okassa, L. N.; Marchais, H.; Douziech-Eyrolles, L.; Cohen-Jonathan, S.; Souce, M.; Dubois, P.; Chourpa, I. *Int. J. Pharm.* **2005**, *302* (1-2), 187.

(95) Zhang, Y.; Kohler, N.; Zhang, M. *Biomaterials* **2002**, *23*, 1553.

(96) Lacava, L. M.; Lacava, Z. G. M.; Da Silva, M. F.; Silva, O.; Chaves, S. B.; Azevedo, R. B.; Pelegrini, F.; Gansau, C.; Buske, N.; Sabolovic, D.; Morais, P. C. *Biophys. J.* **2001**, *80*, 2483.

(97) Zhang, C.; Wangler, B.; Morgenstern, B.; Zentgraf, H.; Eisenhut, M.; Untenecker, H.; Kruger, R.; Huss, R.; Seliger, C.; Semmler, W.; Kiessling, F. *Langmuir* **2007**, *23* (3), 1427.

(98) Mulvaney, P.; Liz-Marzan, L. M.; Giersig, M.; Ung, T. *J. Mater. Chem.* **2000**, *10*, 1259.

(99) Tartaj, P.; Gonzalez-Carreno, T.; Serna, C. J. *Langmuir* **2002**, *18*, 4556.

(100) Tartaj, P.; Gonzalez-Carreno, T.; Serna, C. J. *Adv. Mater.* **2001**, *13*, 1620.

(101) Santra, S.; Tapec, R.; Theodoropoulou, N.; Dobson, J.; Hebard, A.; Tan, W. *Langmuir* **2001**, *17*, 2900.

(102) Chen, M.; Yamamuro, S.; Farrell, D.; Majetich, S. A. *J. Appl. Phys* **2003**, *93*, 7551.

(103) Lin, J.; Zhou, W.; Kumbhar, A.; Fang, J.; Carpenter, E. E.; O'Connor, C. J. *J. Solid State Chem.* **2001**, *159*, 26.

(104) Zhou, W. L.; Carpenter, E. E.; Lin, J.; Kumbhar, A.; Sims, J.; O'Connor, C. J. *Eur. Phys. J. D* **2001**, *16*, 289.

(105) Morawski, A. M.; Winter, P. M.; Crowder, K. C.; Caruthers, S. D.; Fuhrlop, R. W.; Scott, M. J.; Robertson, J. D.; Abendschein, D. R.; Lanza, G. M.; Wickline, S. A. *Magn. Reson. Med.* **2004**, *51*, 480.

(106) Shepherd, P. G.; Popplewell, J.; Charles, S. W. *J. Phys. D: Appl. Phys.* **1970**, *3*, 1985.

(107) Xu, H. K.; Sorensen, C. M.; Klabunde, K. J.; Hadjipanayis, G. C. *J. Mater. Res.* **1992**, *7*, 712.

(108) Alcala, M. D.; Real, C. *Solid State Ionics* **2006**, *177*, 955.

(109) Gushikem, Y.; Rosatto, S. S. *J. Braz. Chem. Soc.* **2001**, *12*, 695.

(110) Woo, K.; Hong, J.; Ahn, J.-P. *J. Magn. Magn. Mater.* **2005**, *293*, 17

(111) van Ewijk, G. A.; Vroege, G. J.; Philipse, A. P. *J. Magn. Magn. Mater.* **1999**, *201*, 31.

(112) Bruce, I. J.; Taylor, J.; Todd, M.; Davies, M. J.; Borioni, E.; Sangregorio, C.; Sen, T. *J. Magn. Magn. Mater.* **2004**, *284*, 145.

(113) Ma, D.; Guan, J.; Normandin, F.; Denommee, S.; Enright, G.; Veres, T.; Simard, B. *Chem. Mater.* **2006**, *18*, 1920.

(114) Yu, J. H.; Lee, C.-W.; Im, S.-S.; Lee, J.-S. *Re*V. *Ad*V. *Mater. Sci.* **2003**, *4*, 55.

(115) Sto¨ber, W.; Fink, A.; Bohn, E. *J. Colloid Interface Sci.* **1968**, *26*, 62.

(116) Philipse, A. P.; van Bruggen, M. P. B.; Pathmamanoharan, C. *Langmuir* **1994**, *10*, 92.

(117) Lu, Y.; Yin, Y.; Mayers, B. T.; Xia, Y. *Nano. Lett.* **2002**, *2*, 183.

(118) Deng, Y.-H.; Wang, C.-C.; Hu, J.-H.; Yang, W.-L.; Fu, S.-K. *Colloids Surf., A* **2005**, *262*, 87.

(119) Barnakov, Y. A.; Yu, M. H.; Rosenzweig, Z. *Langmuir* **2005**, *21*, 7524.

(120) Im, S. H.; Herricks, T.; Lee, Y. T.; Xia, Y. *Chem. Phys. Lett.* **2005**, *40* (1-3), 19.

(121) Butterworth, M. D.; Bell, S. A.; Armes, S. P.; Simpson, A. W. *J. Colloid Interface Sci.* **1996**, *183*, 91.

(122) Liu, X.; Xing, J.; Guan, Y.; Shan, G.; Liu, H. *Colloids Surf., A* **2004**, *238*, 127.

(123) Tartaj, P.; Serna, C. J. *J. Am. Chem. Soc.* **2003**, *125*, 15754.

(124) Tartaj, P.; Serna, C. J. *Chem. Mater.* **2002**, *14*, 4396.

(125) Gao, X.; Yu, K. M. K.; Tamb, K. Y.; Tsang, S. C. *Chem. Comm.* **2003**, 2298.

(126) Lyon, J. L.; Fleming, D. A.; Stone, B.; Schiffer, P.; Willians, M. E. *Nano. Lett.* **2004**, *4*, 719.

(127) Kim, J.; Park, S.; Lee, J. E.; Jin, S. M.; Lee, J. H.; Lee, I. S.; Yang, I.; Kim, J. S.; Kim, S. K.; Cho, M. H.; Hyeon, T. *Angew. Chem., Int. Ed.* **2006**, *45* (46), 7754.

(128) Lee, J.-H.; Huh, Y.-M.; Jun, Y.-w.; Seo, J.-w.; Jang, J.-t.; Song, H.-T.; Kim, S.; Cho, E.-J.; Yoon, H.-G.; Suh, J.-S.; Cheon, J. *Nat. Med.* **2007**, *13*, 95.

(129) Jun, Y.-W.; Seo, J.-W.; Cheon, J. *Acc. Chem. Res.* **2008**, *41*, 179.

(130) Tartaj, P.; Gonzalez-Carreno, T.; Serna, C. J. *J. Phys. D: Appl. Phys*. **2003,** 36 R182–R197, *18*, 4556.

(131) Cunningham, C. H.; Arai, T.; Yang, P. C.; McConnell, M. V.; Pauly, J. M.; Conolly, S. M. *Magn. Reson. Med.* **2005**, *53*, 999.

(132) Shapiro, E. M.; Skrtic, S.; Koretsky, A. P. *Magn. Reson. Med.* **2005**,*53*, 329.

(133) Shapiro, E. M.; Sharer, K.; Skrtic, S.; Koretsky, A. P. *Magn. Reson. Med.* **2006**, *55*, 242.

(134) Blin, B.; Fievet, F.; Beaupere, D.; Figlarz, M. *New J. Chem* **1989**, *13*, 67.

(135) Blin, B.; Fievet, F.; Lagier, J. P.; Beaudoin, B.; Figlarz, M. *Journal De Chimie Physique Et De Physico-Chimie Biologique* **1987**, *84*, R15.

(136) Barr, J.R. *J. Anal. Toxicol.* **2004**, *28*, 305.

(137) Zilinskas, R.A. *J. Am. Med. Assoc.* **1997**, *278*, 418–424.

(138) Fagerquist, C.; Garbus, B. *Anal. Chem* **2010** 82, 2717-2725

(139) McRobbie, D.; Moore, E.;Graves, M. *MRI – From Picture to Proton* Cambridge University Press: New York, **2003**.

(140) Li, Y.; Yan, B.; Deng, C. *Proteomics* **2007**, 7, 3661-3671

(141) Pankhurst, Q.; Connolly, J.; Jones, S.; Dobson, J. *J. Phys. D: Appl. Phys*. **2003**, 36 R167-R181

(142) Giddings, J. *Science* **1993**, 260, 1456-1465

(143) International Center for Diffraction Data http://www.icdd.com/index.htm (Accessed 08/25/08)

(144) P. Scherrer, *Göttinger Nachrichten Gesell.*, Vol. 2, 1918, p 98.

(145) Cullity, B.D.; Stock, S.R. *Elements of X-Ray Diffraction*; 3rd Ed.; Prentice-Hall Inc., 2001

(146) Jenkins ,R.; Snyder, R.L. *Introduction to X-ray Powder Diffractometry*; John Wiley & Sons Inc., 1996

(147) Klug, H.P.; Alexander, L.E. *X-Ray Diffraction Procedures*; 2nd Ed.; John Wiley & Sons Inc., 1974

(148) Warren, B.E. *X-Ray Diffraction*; Addison-Wesley Publishing Co., 1969

(149) Boss, C.B.; Fredeen, K.J. *Concepts, Instrumentation, and Techniques in Inductively Coupled Plasma Optical Emission Spectrometry;* 2nd Edition Perkin-Elmer, 1997

(150) Grabarek, Z.; Gergely, J. *Anal. Biochem* **1990**, 185,131-135..

(151) O'Connell, T.X.; Horita, T.J.; Kasravi, B. *American Family Physician* **2005**, 71, 105

(152) Alberts, B., *Molecular Biology of the Cell*. Garland Publishing, Inc., New York, NY. **1983**

(153) Harlow, E.; Lane, D. *Antibodies: A Laboratory Manual.* Cold Spring Harbor Laboratory, Cold Spring Harbor, NY. **1988**

(154) Sites, D.P., *Basic & Clinical Immunology*. Lange Medical Publication, Los Altos, CA. **1976**

(155) Mellore, J.S.; Jorgenson, J.W. *Anal. Chem.* **2004**, 76, 5441-5450

(156) Bradford, M. *Ana Bioch* **1976,** 72, 248-254

(157) Laurent, S.; Forge, D.; Port, M.; Roch, A.; Robic, C.; Muller, R. *Chem. Rev.* **2008**, 108, 2064-2110

(158) Shaw, D. *Introduction to Colloid and Surface Chemistry*. Butterwoth: UK 1992

(159) Larcher, D.; Patrice, R. *J. Solid State Chem.* **2000**, *154*, 405.

(160) Blin, B.; Fievet, F.; Beaupere, D.; Figlarz, M. *New Jour of Chemistry* **1989**, *13*, 67.

(161) Carroll, K.J.; Reveles, J.U.; Shultz, M.D.; Khanna, S.J.; Carpenter, E.E. *J. Phys. Chem. C* **2011**, 115, 2656-2664

Vita

Christopher Ryan Warren was born on February 3, 1968, in Richmond, Virginia, and is an American Citizen. He graduated from Lee-Davis High School, Mechanicsville, Virginia in 1986. He received his Bachelor of Science in Chemistry from Virginia Commonwealth University, Richmond, Virginia in 1990. He received a Doctor of Philosophy in Chemistry from Virginia Commonwealth University in 2013.